UNIVERSITY OF ROCHESTER
LABORATORY FOR LASER ENERGETICS

Volume 78
January–March 1999
DOE/SF/19460-295

LLE Review

Quarterly Report

About the Cover:

The cover photograph shows Scientist Jonathon Zuegel (bottom) and Research Associate Douglas Jacobs-Perkins (top) aligning a double-pass, two-dimensional smoothing by spectral dispersion (2-D SSD) system that has been developed in the SSD testbed. The high-frequency bulk-phase modulator, highlighted in the lower left portion of the photograph, applies phase-modulated bandwidth to the laser pulse in the second direction of smoothing in the 2-D SSD system. Microwave power is delivered to the modulator from an LLE-built, 20-W solid-state microwave power amplifier that is fed by a microwave oscillator (shown at the right side of the photograph) operating at 10.4077 GHz. The solid-state microwave power amplifier will be replaced with a 1-kW traveling wave tube amplifier in order to generate the 1-THz UV bandwidth operation on OMEGA.

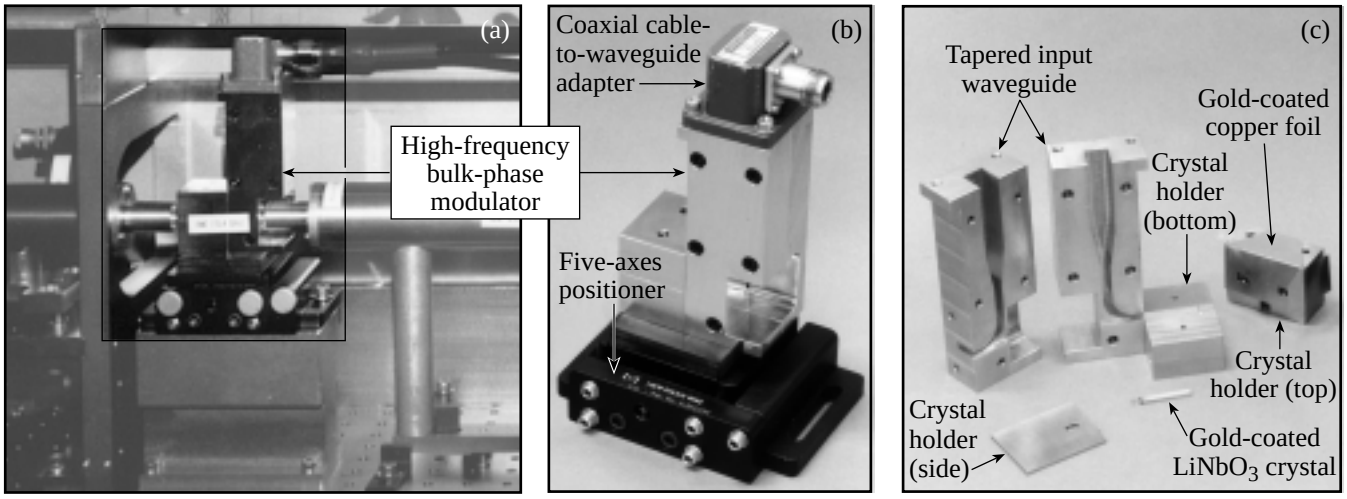

The three photographs shown above illustrate key aspects of the high-frequency bulk-phase modulator. (a) The integration of the modulator in the 2-D SSD system is highlighted. (b) The modulator is aligned in the 2-D SSD system with a five-axes positioner, and the microwave power is delivered to the modulator via a coaxial cable-to-waveguide adapter. (c) The internal structure of the individual components of the modulator is revealed. The crystal holder and tapered input waveguide sections are machined from copper to maximize electrical and thermal conductivity and are gold plated to prevent oxidation of the copper. All four sides of the $LiNbO_3$ crystal are gold coated to form a standing-wave waveguide resonator that is approximately $2 \bullet \lambda_{microwave}$ long, while the ends are antireflection coated for the SSD beam. The overall dimension of the crystal is 3.05 mm × 2.0 mm × 26.3 mm.

The work described in this volume includes current research at the Laboratory for Laser Energetics, which is supported by New York State Energy Research and Development Authority, the University of Rochester, the U.S. Department of Energy Office of Inertial Confinement Fusion under Cooperative Agreement No. DE-FC03-92SF19460, and other agencies.

Printed in the United States of America
Available from
National Technical Information Services
U.S. Department of Commerce
5285 Port Royal Road
Springfield, VA 22161
Price codes: Printed Copy A04
Microfiche A01

For questions or comments, contact Sean P. Regan, *Editor*, Laboratory for Laser Energetics, 250 East River Road, Rochester, NY 14623-1299, (716) 275-7077; e-mail: sreg@lle.rochester.edu.

Worldwide-Web Home Page: http://www.lle.rochester.edu/

UNIVERSITY OF ROCHESTER
LABORATORY FOR LASER ENERGETICS

Volume 78
January–March 1999
DOE/SF/19460-295

LLE Review

Quarterly Report

UR LLE

Contents

In Brief

This volume of the LLE Review, covering the period January–March 1999, features two articles concerning issues relevant to 2-D SSD laser-beam smoothing on OMEGA. In the first article J. D. Zuegel and J. A. Marozas present the design of an efficient, bulk phase modulator operating at approximately 10.5 GHz, which can produce substantial phase-modulated bandwidth with modest microwave drive power. This modulator is the cornerstone of the 1-THz UV bandwidth operation planned for OMEGA this year. In the second article J. A. Marozas and J. H. Kelly describe a recently developed code—Waasese—that simulates the collective behavior of the optical components in the SSD driver line. The measurable signatures predicted by the code greatly enhance the diagnostic capability of the SSD driver line.

Additional highlights of the research presented in this issue are

- F. J. Marshall, J. A. Delettrez, V. Yu. Glebov, R. P. J. Town, B. Yaakobi, R. L. Kremens, and M. D. Cable report results of a 60-beam implosion experiment of hollow shell targets. A survey of target performance based on laser-irradiation uniformity and laser pulse shape was conducted, and compression of the shell material to areal densities of ~60 to 130 mg/cm^2 was observed.

- R. D. Petrasso, P. B. Radha, D. G. Hicks, C. K. Li, F. H. Seguin, V. Yu. Glebov, C. Stoeckl, and J. M. Soures demonstrate on OMEGA the diagnostic capability of the two charged-particle magnetic spectrometers, which LLE has developed in collaboration with MIT and LLNL. As an initial application, simultaneous measurements of the fuel areal density, shell areal density, and fuel temperature have been carried out on OMEGA using D^{3}He-filled imploding capsules.

- M. D. Skeldon describes the modeling of an aperture-coupled-stripline (ACSL), electrical-waveform generator that produces an optical seed pulse for OMEGA. Details of the on-target pulse shape are related critically to the details of the seed-pulse shape. The ACSL pulse-shaping system will be implemented on OMEGA in the next few months. The model is based on a numerical solution of the telegraph equations using the method of characteristics.

- K. Green and R. Sobolewski present a measurement technique that enables the complete characterization of electronic devices having any dynamic temporal and spectral frequency response, such as the photoconductive microwave switches on OMEGA's pulse-shaping system. The technique is a superset of a form of input–output relationships called the scattering or *S* parameter; this technique can also be applied to any microwave or millimeter-wave device whose properties vary rapidly, such as photoconductive attenuators, phase shifters, and directional couplers.

- A. L. Rigatti, D. L. Smith. A. W. Schmid, S. Papernov, and J. H. Kelly examine the damage to OMEGA's stage-C-input, C-output, D-input, E-input, and F-input fused-silica, spatial-filter lenses. LLE has implemented a plan to maintain the quality of OMEGA optics that includes frequent inspections and *in-situ* cleaning of optics. With the establishment of safe operational damage criteria, laser operation has not been impeded. The implications, morphologies, possible causes, and ongoing long-term experiments of spatial-filter lens damage are discussed.

Sean P. Regan
Editor

High-Frequency Bulk Phase Modulator for Broadband Smoothing by Spectral Dispersion on OMEGA

High laser-irradiation uniformity is an important requirement for successful direct-drive inertial confinement fusion (ICF). Direct-drive laser-irradiation uniformity is achieved on OMEGA for different ranges of spatial frequencies using smoothing by spectral dispersion (SSD), polarization smoothing with distributed polarization rotators (DPR's), and multiple-beam overlap.[1] SSD significantly improves irradiation uniformity by rapidly shifting the laser speckle pattern generated by distributed phase plates (DPP's). A high-frequency electro-optic phase modulator produces a wavelength modulation that is subsequently converted by a diffraction grating into the angular deflection required to shift the speckle pattern. The low spatial frequency cutoff of the smoothing produced by SSD is determined by the maximum deflection of the beam. Extremely smooth, time-averaged intensity profiles are achieved on a time scale corresponding to the inverse bandwidth impressed by the phase modulator; thus, larger SSD bandwidths are desirable. Two-dimensional SSD (2-D SSD) extends the smoothing benefits of SSD by using two separate stages of bulk electro-optic phase modulators and gratings to deflect the laser speckle pattern in orthogonal directions.

For OMEGA, implementing a high-frequency modulator in the second direction of the 2-D SSD system is advantageous since the bandwidth from the second modulator is not dispersed until after the most-limiting spatial-filter pinhole, which is located in the large-aperture ring amplifier (LARA)[2] in the driver line. This constraint requires that high-frequency phase modulation be generated in a bulk electro-optic modulator to accommodate the dispersed bandwidth from the first modulator.

Design methods used to develop the current generation of 3.0- and 3.3-GHz bulk phase modulators[3] are directly relevant to higher-frequency designs, but several factors merit special attention in higher-frequency modulators designed to generate large SSD bandwidths. First, resonant designs are attractive since higher electric fields can be developed in the electro-optic material without expensive, high-power microwave sources. Velocity-matching the optical and microwave fields is also important to achieve efficient optical phase modulation. Lastly, controlling FM-to-AM conversion at higher-modulation frequencies is a more difficult system problem.

A number of bulk electro-optic phase modulator designs are found in the literature.[4–10] An approximately 9-GHz modulator[4] implemented on the original 24-beam OMEGA laser system incorporated a lithium niobate ($LiNbO_3$) crystal inside an evacuated, high-Q microwave resonator, but it suffered difficulties coupling microwave power from the resonator mode into the crystal. Velocity-matched waveguide resonator designs[5–7] operate at microwave frequencies near the waveguide cutoff to match the optical and microwave phase velocities. This matching allows arbitrarily long interaction lengths to be used to achieve increased modulation efficiency. A quasi-velocity-matched concept[8] uses periodically poled lithium tantalate ($LiTaO_3$) to approximately realize this same advantage with the added advantage of a TEM modulation field, but it suffers from the inherently lower Q factor of a micro strip resonator. An ~20-GHz dielectric resonator design[9] achieves a high Q factor, but the electric field distribution of the TM_{101} resonant mode is poorly suited for 2-D SSD applications. Convenient coupling of microwave power into a resonator structure is also a critical design issue. Electric-probe[6,9] and magnetic-loop[7] coupling require that the resonator structure be partially air filled, but this reduces the maximum clear aperture. Cutoff-waveguide coupling eliminates this disadvantage and, in addition, offers the possibility of tuning the resonance frequency.[10]

Incorporating a higher-frequency phase modulator in the 2-D SSD system offers two approaches to improving irradiation uniformity on OMEGA. First, larger SSD bandwidths can be generated for a given number of FM sidebands and propagated through the laser system since less grating dispersion is required to achieve a single color cycle. Increased SSD bandwidths smooth laser irradiation faster. An asymmetric 2-D SSD configuration on OMEGA using phase modulators operating at 3.0 and ~10 GHz could achieve infrared bandwidths of 1.5 $\times$ 12 Å, respectively, to generate 1×1 color cycles nominally.

This infrared bandwidth corresponds to a UV bandwidth of approximately 1 THz. To efficiently convert this infrared bandwidth to the ultraviolet, dual-tripler frequency-conversion crystals[11] (FCC's) must be implemented on all 60 OMEGA beams. This upgrade will be completed before the end of 1999.

Alternately, multiple SSD color cycles can be produced with a higher modulation frequency for a given grating design, and the same SSD bandwidth can be propagated without exceeding the beam divergence limit imposed by the laser system pinholes. Increasing the number of color cycles redistributes the beam nonuniformity to higher spatial frequencies and accelerates the smoothing at the mid-range spatial frequencies (ℓ = 50–200) that pose the greatest threat of seeding hydrodynamic instabilities in direct-drive implosions.[1] The current OMEGA FCC configuration can efficiently convert infrared bandwidths of 1.5×3.0 Å from modulators operating at 3.0 and ~10 GHz to generate 1×3 color cycles, respectively. Experiments utilizing both 1-THz UV bandwidth and multiple color cycle improvements are planned for OMEGA this year.

High-Frequency Modulator Design

A velocity-matched, waveguide-coupled, $LiNbO_3$ dielectric resonator modulator design was selected for the 2-D SSD, high-frequency modulator application. A simple sketch of a generic cutoff-waveguide-coupled resonator[10] is presented in Fig. 78.1(a). A TE_{10} mode of the input waveguide delivers microwave radiation to a high-Q, TE_{10n} standing-wave resonator formed by locating an electro-optic material in an air waveguide that would otherwise be below cutoff at the resonance frequency.

Velocity mismatches between the microwave and optical phase velocities in an electro-optic material reduce phase-modulation efficiency,[12] particularly at high modulation frequencies. In the resonant microwave cavities used for SSD bulk phase modulators, standing waves are impressed across the electro-optic crystal, which can be decomposed into fields co-propagating and counter-propagating with the laser beam. For this case, the velocity-mismatch reduction factor β is given by[12]

$$\beta = \frac{1}{2}\left|\frac{\sin(u_+)}{u_+} + \frac{\sin(u_-)}{u_-}\right|, \tag{1a}$$

$$u_\pm = \left(\frac{\pi f_m L}{c}\right)\left(\sqrt{\varepsilon_3} \mp n_3\right), \tag{1b}$$

where ε_3 is the relative dielectric constant of the electro-optic crystal for polarizing the applied microwave field at the modulation frequency f_m, n_3 is the index of refraction of the crystal, and c is the speed of light in vacuum. The first term of Eq. (1a) accounts for the contribution of the optical beam interacting with the co-propagating microwave, while the second term is associated with the counter-propagating microwave field. The maximum effective interaction length βL for a 10.5-GHz $LiNbO_3$ modulator with no velocity matching is limited to approximately 2 mm, as shown in Fig. 78.2.

Velocity matching is achieved in the configuration shown in Fig. 78.1(a) by setting the width of the crystal, a, to adjust the microwave phase velocity in the waveguide geometry,

$$v_{\text{phase}} = \frac{c}{\sqrt{\varepsilon_3}\sqrt{1-\left(f_c/f_0\right)^2}}, \qquad f_c = \frac{c}{2a\sqrt{\varepsilon_3}}, \tag{2}$$

to match the optical phase velocity in the electro-optic material, c/n_3, where f_c is the cutoff frequency of the waveguide section loaded with the crystal and f_0 is the resonance frequency of the modulator. Figure 78.2 plots the effective interaction length as a function of crystal length for waveguide resonators with different degrees of velocity matching. For a perfectly velocity-matched design, the effective interaction length grows linearly with some modulation caused by the interaction with the counter-propagating microwave field. An almost negligible penalty is observed for a 10% velocity mismatch with a 26.3-mm crystal length shown in Fig. 78.1(c).

The height b of the crystal is arbitrary for a TE_{10n} mode; however, minimizing b increases the electric field magnitude for a given microwave drive power and can eliminate spurious TE_{01m} modes in the crystal that would divert microwave energy if mode-coupling mechanisms exist. The length of the electro-optic material determines the modulator resonance frequency based on the microwave phase velocity in the waveguide. A resonance exists for crystals that are an integer number of half-wavelengths, plus any phase shifts associated with the reflections at the cutoff-waveguide sections. For materials with a high dielectric constant, these phase shifts are generally small and only change the effective length of the resonator by about 1%.[10]

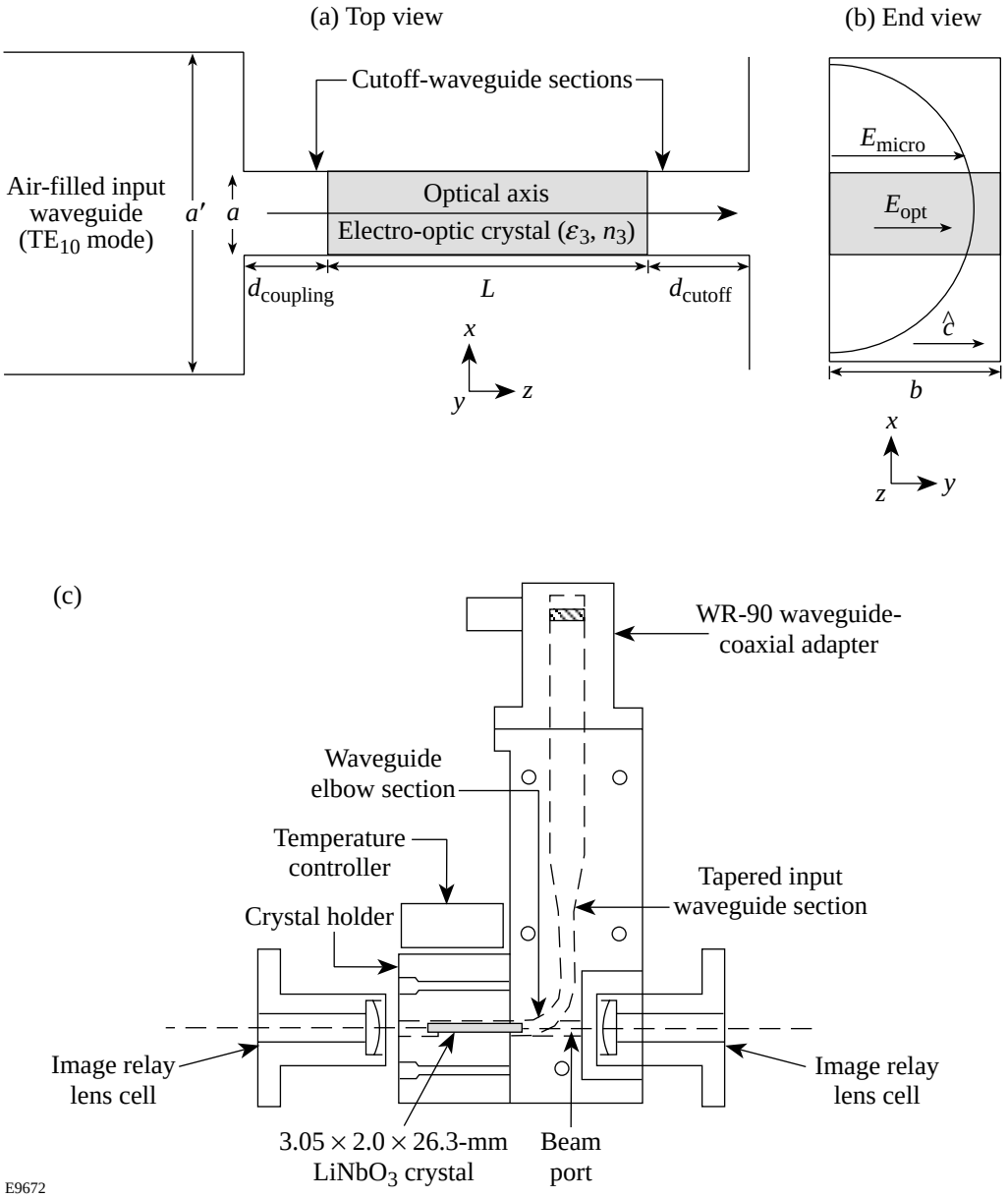

Figure 78.1

(a) Generic cutoff-waveguide-coupled resonator. The electro-optic crystal of length L is positioned in an air-filled, rectangular waveguide of width a and height b. The waveguide width sets the cutoff frequency above the modulator operating frequency in the air-filled sections, but below cutoff in the crystal. The cutoff-waveguide sections act as high reflectors for the standing waves inside the electro-optic crystal resonator. The input waveguide width a' supports traveling waves at the operating frequency that evanescently couple through the coupling distance $d_{coupling}$. (b) The microwave and optical electric fields, E_{micro} and E_{opt}, are oriented along the crystalline c axis to take advantage of the large electro-optic tensor element r_{33} in $LiNbO_3$. The beam size is small enough so that the variation of the microwave field in the x direction is only 15%. (c) A tapered input waveguide provides a transition from standard waveguide dimensions to dimensions required for critical coupling into the modulator crystal. A small beam port in the input waveguide bend provides optical access to the crystal but does not disturb the microwave input since it is significantly smaller than the microwave wavelength.

All SSD modulators designed and built at LLE have used $LiNbO_3$, which is a well-developed electro-optic crystalline material. Other electro-optic materials are commercially available and were considered for the new high-frequency modulator design, including $LiTaO_3$, potassium titanyl phosphate (KTP) and its crystal isomorphs, rubidium titanyl arsenate (RTA), and cesium titanyl arsenate (CTA). Relevant optical and microwave properties of these materials are reported in Table 78.I. A large electro-optic coefficient is obviously desirable, but the index of refraction and relative dielectric constant also play a significant role in maximizing the phase-modulation performance, as indicated by the electro-optic figure of merit. The loss tangent is inversely related to the fundamental limit on the Q factor that can be achieved in a resonant design[13] since it represents the dielectric losses in each material. Lastly, the laser-damage threshold is an important performance parameter. Both bulk and surface laser-damage thresholds were measured for undoped $LiNbO_3$ and are presented in Table 78.I. The surface finish of the samples limited the surface-damage threshold, while a lower bound on the bulk damage threshold was established that was limited by catastrophic surface damage. Doped samples of Zn:$LiNbO_3$ and MgO:$LiNbO_3$ showed poorer damage thresholds. RTA is a potentially attractive alternative possessing a high electro-optic figure of merit, a loss tangent almost four times lower than $LiNbO_3$, plus a lower dielectric constant that would facilitate approximately 20% larger crystal clear apertures. The optical quality of RTA, however, is not currently adequate for SSD applications since strong birefringence gradients are reported and the laser-damage threshold is significantly lower than commercially available $LiNbO_3$.

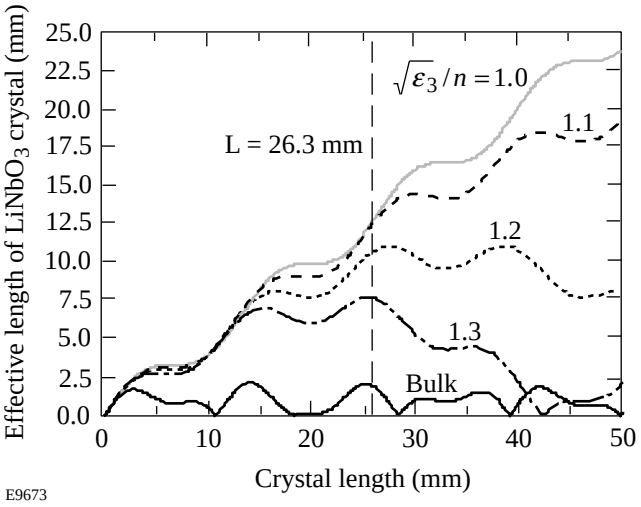

Figure 78.2
Effective interaction length with velocity matching in $LiNbO_3$ modulators. Bulk modulator with no velocity matching (heavy solid line); perfect velocity matching essentially linear with respect to interaction length, with modulation due to interaction with counter-propagating microwave fields (light solid line); variations of velocity mismatch in 10% graduations (dashed lines).

Setting the beam size in a TE_{10n}-mode waveguide modulator requires a compromise between maximizing the uniformity of the phase-modulation depth across the beam and minimizing FM-to-AM conversion. The electric field of the standing wave varies across the transverse dimension, as shown in Fig. 78.1(b). This field distribution produces an index-of-refraction variation equivalent to a time-varying cylindrical gradient-index lens. Minimizing the SSD beam size to the central portion of the aperture minimizes this effect but increases the difficulty of SSD system imaging. The phase-modulated bandwidth dispersed by the SSD gratings must be carefully imaged to prevent FM-to-AM conversion resulting from propagation out of a grating image plane; otherwise,

Table 78.I: Electro-optic material properties.

	$LiNbO_3$ (Refs. 14,15)	$LiTaO_3$ (Refs. 16,17)	KTP (Ref. 18)	RTA (Ref. 16)	CTA (Ref. 16)
Crystalline type	uniaxial	uniaxial	biaxial	biaxial	biaxial
Electro-optic coefficient (pm/V)	r_{33} = 28.8–30.8	33	35.0	40.5	38.0
Index of refraction	n_3 = 2.1561 (extraordinary)	2.143	n_z = 1.840	n_z = 1.890	n_z = 1.930
Relative dielectric constant	ε_{33} = 23.7–27.9	41.4–43	15.4	19	29
Loss tangent (at 10 GHz)	0.0015	0.001	0.70	0.0004	0.002
Electro-optic figure of merit $n_3^6 r_{33}^2/\varepsilon_r \left(\mathrm{pm}^2/V^2\right)$	3304	2548	2705	3935	2573
Laser-damage threshold (GW/cm^2)	>22 (bulk) >2.0 (surface)		>1	0.4	0.4

intensity modulation develops even from a perfectly FM-modulated beam according to

$$\frac{\Delta I}{I} \propto \delta_{\mathrm{mod}} \cdot \left(\omega_{\mathrm{mod}}\, d\theta/d\lambda\right)^2 z \propto \delta_{\mathrm{mod}} \cdot \left(\frac{N_{\mathrm{cc}}}{D_{\mathrm{beam}}}\right)^2 z, \quad (3)$$

where δ_{mod} is the phase-modulation depth, ω_{mod} is the phase-modulation angular frequency, $d\theta/d\lambda$ is the effective grating dispersion, z is the distance from the nearest image plane, N_{cc} is the number of color cycles impressed on the SSD beam, and D_{beam} is the beam diameter. Demagnifying the SSD beam to fit through the modulator increases the sensitivity to imaging errors and color separation of the dispersed FM beam on system optics that can lead to amplitude modulation. This is especially true for systems employing multiple color cycles.

The 10.5-GHz, waveguide-coupled $LiNbO_3$ modulator design [shown in Fig. 78.1(c)] includes four parts: a $LiNbO_3$ crystal, a crystal holder, a tapered input waveguide section, and a temperature controller. For a $LiNbO_3$ modulator operating at 10.5 GHz, the ideal crystal width to achieve velocity matching according to Eq. (2) sets $a = 3.064$ mm. All four sides of the crystal are gold coated to form a standing-wave waveguide resonator that is approximately $2 \bullet \lambda_{\mathrm{microwave}}$ long, while the ends are antireflection coated for the SSD beam. The height is the smallest possible consistent with a 1.1-mm beam size chosen to limit the time-varying cylindrical phase error to a reasonable level.

The crystal holder and tapered input waveguide sections are machined from copper to maximize electrical and thermal conductivity and are gold plated to prevent oxidation of the copper. The high electrical conductivity of copper minimizes conduction losses in both the input waveguide and the waveguide resonator since the gold coatings on the crystal are only a fraction of a skin depth at 10.5 GHz. Good thermal conduction is also beneficial in maintaining a uniform temperature across the crystal.

The crystal holder is machined from three pieces of copper that confine the $LiNbO_3$ crystal on three sides while a copper foil holds it in place. This configuration ensures high-conductivity walls next to the crystal with no air gaps in the direction of the microwave electric field and minimal stress on the crystal. Active temperature control of the modulator crystal is planned to stabilize the resonance frequency and provide a limited range of tuning. The simulated results discussed below are based on the modulator operating at 50°C to provide a ±20°C range of temperature to accommodate uncertainties in the dielectric constant and crystal fabrication tolerances. A significant advantage of the modulator design is that the crystal holder can accept various crystal sizes designed to operate at different resonance frequencies.

The tapered input waveguide section transfers microwave power from a standard coaxial-to-WR-90 waveguide adapter to a 4-mm-high waveguide section suitable for coupling the microwave energy into the modulator crystal. The taper length is $\lambda_{\mathrm{microwave}}/2$ to minimize reflections associated with the waveguide discontinuities. A $\lambda_{\mathrm{microwave}}/2$-long waveguide elbow is also included with a small beam port for optical beam access to the microwave input side of the crystal.

Maximizing microwave power transfer into a cutoff-waveguide-coupled resonator at resonance is accomplished by adjusting d_{coupling} to vary the coupling coefficient,[10]

$$\beta_{\mathrm{coupling}} = \frac{16}{\pi^3}\frac{Q_0}{L_{\mathrm{eff}}}\frac{\frac{a'}{a}\cos^2\left(\frac{\pi}{2}\frac{a'}{a}\right)}{\left[1-\left(\frac{a'}{a}\right)^2\right]^2}\frac{\varepsilon_r - \left(\frac{\lambda_0}{2a'}\right)^2}{\varepsilon_r\left(\varepsilon_r - 1\right)}$$

$$\times\ \lambda_0\sqrt{1-\left(\frac{\lambda_0}{2a}\right)^2}\ \exp\left[-\frac{2\pi d_{\mathrm{coupling}}}{a'}\sqrt{1-\left(\frac{2a}{\lambda_0}\right)}\right], \quad (4)$$

to achieve critical coupling ($\beta_{\mathrm{coupling}} = 1$), where Q_0 is the resonator Q factor, L_{eff} is the effective length of the $LiNbO_3$ crystal, and λ_0 is the free-space microwave wavelength; the remaining dimensions are defined in Fig. 78.1(a). Critical coupling maximizes the power transferred into the resonator.[19] Equation (4) was derived assuming no reaction of the cavity field on the waveguide field and is valid only for positive coupling distances. Using this analytic expression, the coupling coefficient calculated for the modulator presented in Fig. 78.1(c) is plotted in Fig. 78.3, where it is seen that critical coupling is not achieved, even for $d_{\mathrm{coupling}} = 0$. This results from the poor overlap between the input waveguide and crystal resonator modes, which is limited by the large mismatch between the input waveguide width and the small crystal width imposed by the velocity-matching constraint. Although Eq. (4) cannot be extrapolated to negative coupling distances, it strongly suggests that allowing the modulator crystal to extend into the input waveguide would achieve critical coupling.

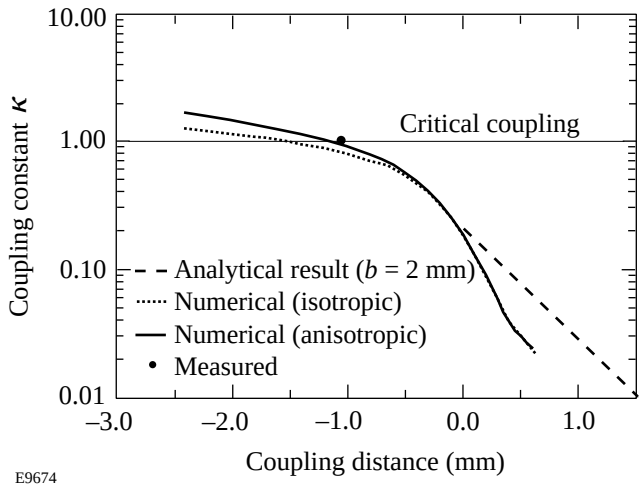

Figure 78.3
Coupling coefficient plotted versus coupling distance for waveguide-coupled $LiNbO_3$ modulator. The analytic values calculated from Eq. (4) are plotted in the dashed line only for positive coupling distances assuming the input waveguide and crystal heights are equal. Values from Micro-Stripes simulations modeling $LiNbO_3$ as an isotropic dielectric, as well as using the tensor values for the dielectric constant are plotted as dotted and solid lines, respectively. Critical coupling was experimentally observed for $d_{coupling}$ = 1.07 mm and plotted.

Accurately analyzing configurations where the crystal protrudes into the input waveguide was accomplished numerically using Micro-Stripes, a commercial three-dimensional electromagnetic analysis package.[20] Micro-Stripes yields both time- and frequency-domain electromagnetic solutions for arbitrary geometries, including tensor material properties such as the dielectric constant for materials like $LiNbO_3$, which are difficult to treat analytically. A particular strength of this simulation package is that wideband frequency-domain results with fine resolution are obtained from a single time-domain simulation.

A typical Micro-Stripes model and the results from a simulation are shown in Fig. 78.4. All the geometric details and material properties of the modulator shown in Fig. 78.4(a) are represented in the model. In a simulation, an electromagnetic impulse is launched in the input waveguide, and the fields throughout the model are calculated as a function of time. Field values are saved at probe points for post-simulation analysis, including digital filtering, resolving incident and reflected waves, and transforming into the frequency domain. The complex reflection coefficient can be calculated as a function of frequency from the simulated forward and reflected microwave field components. The complex reflection coefficient can then be analyzed using a personal computer program QZERO[19] to yield the three important resonator parameters: the resonance frequency, the resonator Q factor, and the coupling coefficient.

(a)

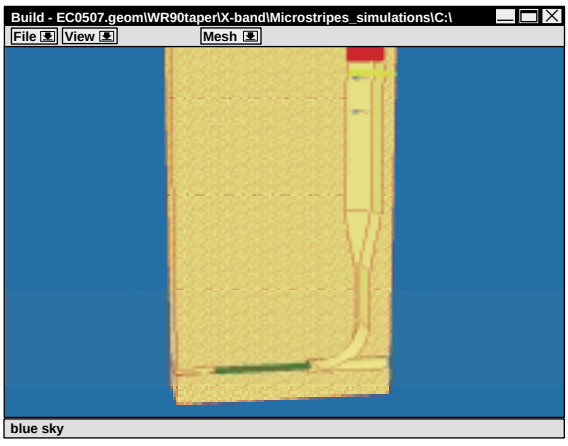

(b)

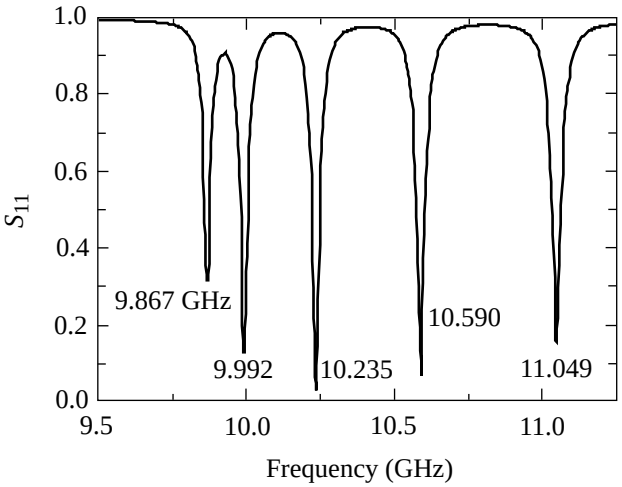

Figure 78.4
Micro-Stripes numerical simulations. (a) The complete three-dimensional, anisotropic geometry of the $LiNbO_3$ modulator shown in Fig. 78.1(c) is modeled with spatial resolution required to yield accurate results; (b) the magnitude of the complex reflectivity plotted versus excitation frequency reflects the harmonic spectrum of the waveguide resonator formed by the $LiNbO_3$ crystal.

Micro-Stripes simulations were performed using an isotropic dielectric constant equal to the value along the designed microwave electric field direction (ε_{33}), as well as the tensor values available from the literature.[15] Simulations for a range of crystal positions were calculated and the coupling coefficient plotted in Fig. 78.3. For both cases, the coupling increases as the $LiNbO_3$ crystal protrudes farther into the input waveguide. Critical coupling is achieved for $d \approx 1.2$ mm for the anisotropic calculation. The magnitude of the complex reflection coefficient plotted versus frequency for this crystal position is shown in Fig. 78.4(b). Nearly critical coupling into a high-Q resonance is evident from the narrow, low-reflection feature representing the $4 \cdot \lambda_{microwave}/2$ mode of the crystal resonator. Another feature evident from Fig. 78.4(b) is that the modulator can be optimally coupled for any of the other resonances to access even higher modulation frequencies; however, given the fixed resonator geometry defined by the crystal, a velocity-mismatch penalty would be incurred.

Figure 78.5 shows the predicted variation of the resonance frequency f_0 and the resonator Q factor over the same range of crystal positions for the $4 \cdot \lambda/2$ resonance as covered in Fig. 78.3. The resonance frequency shows a relatively small variation, and the Q factor is essentially unchanged over the range of crystal positions producing significant microwave coupling into the crystal. Interestingly, the resonance frequency plotted in Fig. 78.5(a) initially decreases as the length of the crystal protruding into the input waveguide increases, after which it increases monotonically. The initial drop in resonance frequency, as well as the initially widening differences between the isotropic and anisotropic simulations of the resonance frequency, indicate that the effective length of the resonator increases as the resonator fields extend into the input waveguide and the fields distort near the crystal input. This field distortion introduces electric field components that interact with the higher dielectric constant (ε_{11}) in the x and z directions. After reaching minima, values for the resonance frequency for both cases increase at the same rate since the crystal length inside the crystal holder decreases. For positive values of the coupling distance $d_{coupling}$, the predicted resonance frequency approaches the value characteristic of the crystal loaded in an infinitely long, cutoff waveguide. The predicted Q factor in Fig. 78.5(b) also increases since the coupling losses into the input waveguide rapidly decrease, as seen in Fig. 78.3.

Modulator Performance

Microwave measurements of the X-band modulator and adjustments to optimize coupling were performed using a microwave vector network analyzer (HP Model 8720B). As designed, the length of the crystal protruding into the input waveguide was set to maximize microwave coupling into the $4 \cdot \lambda/2$ resonance. Excellent coupling was achieved for a coupling distance of −1.07 mm. Within experimental uncertainties the measured return loss of −35 dB represents critical coupling and is plotted in Fig. 78.3. Excellent agreement with predicted values of the coupling coefficient is observed.

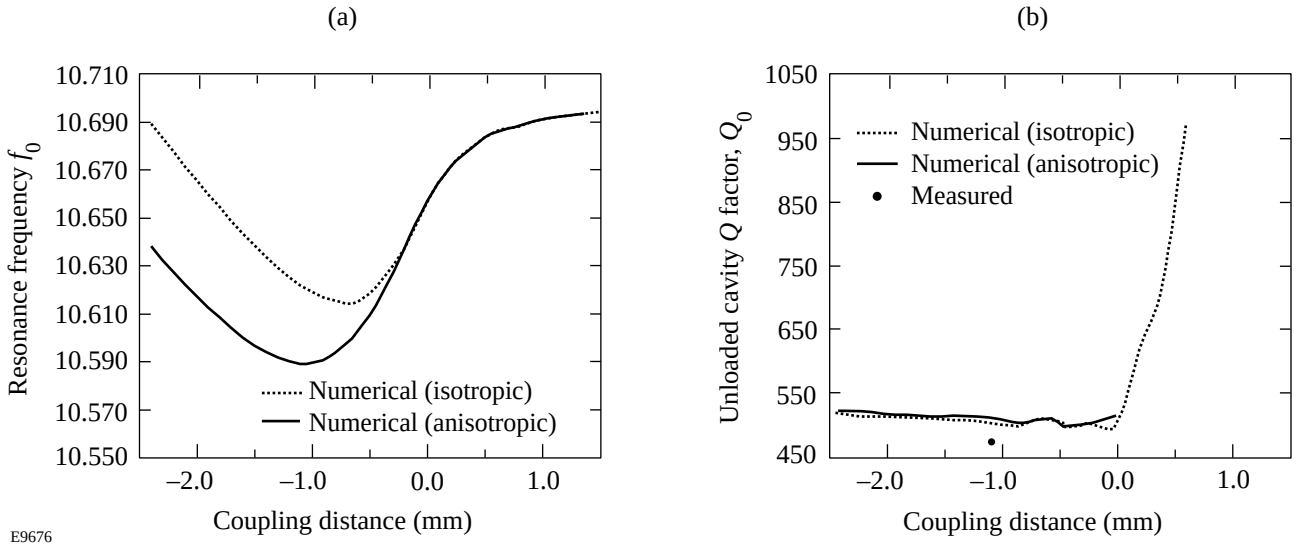

Figure 78.5
(a) Resonance frequency and (b) Q factor for cutoff-coupled, $LiNbO_3$ waveguide modulator.

The measured complex reflectivity of the modulator was also analyzed to evaluate the resonance frequency and Q factor. The measured resonance frequency at critical coupling is 10.412 GHz, which is 1.7% lower than predicted from the Micro-Stripes simulations. This discrepancy is attributed to three factors: First, the cutoff-waveguide cross section at the end of the crystal opposite the input waveguide was enlarged slightly to simplify alignment of the modulator in the SSD system, which would increase the effective length of the resonator and reduce the resonance frequency. Second, crystal fabricating tolerances resulted in slightly larger width and length dimensions that also increase the effective resonator length. Lastly, the actual dielectric tensor values for the $LiNbO_3$ crystal may differ from the literature values[15] used in the simulations. The measured Q factor plotted in Fig. 78.5(b) agrees well with the predicted values.

Experimentally, double-pass operation yields 1.95-Å SSD bandwidths with approximately 14.4 W of microwave power delivered to the modulator. This measurement of phase-modulation performance shows reasonable agreement with a simple estimate based on microwave measurements. The microwave energy stored in the resonator, E_{stored}, can be calculated from the definition of the unloaded Q factor,

$$Q_0 \equiv \omega_0 \, E_{\text{stored}} / P_{\text{in}} ,$$

where P_{in} is the power delivered to the modulator and ω_0 is the angular microwave frequency $\omega_0 = 2\pi f_0$. The stored energy E_{stored} can be related easily to the electric field strength inside the crystal, E_0, by approximating the field distribution with the mode of a TE_{10n} resonator and spatially integrating to derive

$$E_{\text{stored}} = \varepsilon_{33} / 8 (abL) E_0^2 ,$$

where ε_{33} is the dielectric constant, and a, b, and L are the crystal width, height, and length, respectively. These expressions can be combined with the expression for phase-modulation depth,[3]

$$\delta_{\text{mod}} = \frac{\pi \cdot \beta L \cdot n_3^3 \, r_{33}}{\lambda_{\text{opt}}} E_0 ,$$

where βL is the effective crystal length including velocity mismatch, n_3 is the index of refraction, r_{33} is the electro-optic coefficient, and λ_{opt} is the optical wavelength. Using the measured values for Q_0, a, b, and L, literature values for ε_{33}, n_3, and r_{33}, a calculated value of $\beta L = 0.95$ to account for some velocity mismatch tolerance, a phase-modulation depth of 1.59 is calculated. For a single pass, this corresponds to an SSD bandwidth $\Delta\lambda_{\text{single}} = 1.22$ Å, or a double-pass bandwidth $\Delta\lambda_{\text{double}} = 2.44$ Å.

Additional SSD bandwidth can be achieved by increasing the number of passes through the modulator or increasing input power. Based on the measured performance, a double-pass configuration would require approximately 520 W of microwave drive power to generate 12 Å of phase-modulated bandwidth, while an active multipass scheme with four passes would require less than 130 W at the expense of greater system complexity.

Conclusion

The design of an efficient, bulk phase modulator operating at approximately 10.5 GHz, which can produce substantial phase-modulated bandwidth with modest microwave drive power, has been presented. The waveguide resonator design employs an adapted form of cutoff-waveguide coupling and velocity matching to yield a simple, high-Q microwave design with practical clear-aperture dimensions suitable for application in a 2-D SSD system. The design is easily scalable to other frequencies by simply changing the electro-optic crystal dimensions. The measured microwave performance of the modulator agrees well with performance predicted from fully anisotropic, three-dimensional numerical simulations.

ACKNOWLEDGMENT

The authors acknowledge the support of the staff at the Laboratory for Laser Energetics of the University of Rochester without whose many years of diligent work the OMEGA laser system would not exist. This work was supported by the U.S. Department of Energy Office of Inertial Confinement Fusion under Cooperative Agreement No. DE-FC03-92SF19460, the University of Rochester, and New York State Energy Research and Development Authority. The support of DOE does not constitute an endorsement by DOE of the views expressed in this article.

REFERENCES:

1. S. Skupsky and R. S. Craxton, Phys. Plasmas **6**, 2157 (1999).
2. Laboratory for Laser Energetics LLE Review **58**, 90, NTIS document No. DOE/SF/19460-17 (1994). Copies may be obtained from the National Technical Information Service, Springfield, VA 22161.
3. Laboratory for Laser Energetics LLE Review **68**, 192, NTIS document No. DOE/SF/19460-139 (1996). Copies may be obtained from the National Technical Information Service, Springfield, VA 22161.
4. Laboratory for Laser Energetics LLE Review **48**, 169, NTIS document No. DOE/DP40200-175 (1991). Copies may be obtained from the National Technical Information Service, Springfield, VA 22161.
5. G. Carter, Appl. Phys. Lett. **32**, 810 (1978).

6. T. F. Gallagher, N. H. Tran, and J. P. Watjen, Appl. Opt. **25**, 510 (1986); N. H. Tran *et al*., Appl. Opt. **24**, 4282 (1985); T. F. Gallagher and J. P. Watjen, U.S. Patent No. 4,733,397 (22 March 1988).

7. A. A. Godil, U.S. Patent No. 5,414,552 (9 May 1995).

8. F.-Z. Guo *et al*., IEEE J. Quantum Electron. **33**, 879 (1997).

9. A. A. Godil *et al*., Opt. Lett. **16**, 1765 (1991).

10. E. Bonek *et al*., AEU **32**, 209 (1978).

11. A. Babushkin, R. S. Craxton, S. Oskoui, M. J. Guardalben, R. L. Keck, and W. Seka, Opt. Lett. **23**, 927 (1998).

12. I. P. Kaminow and J. Liu, Proc. IEEE **51**, 132 (1963).

13. D. M. Pozar, *Microwave Engineering*, 2nd ed. (Wiley, New York, 1998).

14. Y. Ohmachi, K. Sawamoto, and H. Toyoda, Jpn. J. Appl. Phys. **6**, 1467 (1967).

15. R. S. Weis and T. K. Gaylord, Appl. Phys. A **37**, 191 (1985).

16. Crystal Technology data sheet, Palo Alto, CA 94303 (May 1993).

17. J. R. Teague, R. R. Rice, and R. Gerson, J. Appl. Phys. **46**, 2864 (1975).

18. Crystal Associates data sheet, Waldwick, NJ 07463 (May 1996).

19. D. Kajfez, *Q Factor* (Vector Fields, Oxford, MS, 1994).

20. Micro-Stripes^{TM}, available from Sonnet Software, Inc., Liverpool, NY 13090.

Angular Spectrum Representation of Pulsed Laser Beams with Two-Dimensional Smoothing by Spectral Dispersion

Pulsed laser beams with two-dimensional smoothing by spectral dispersion (2-D SSD), used in inertial confinement fusion (ICF), improve the on-target uniformity on the OMEGA laser system;[1–4] however, 2-D SSD is highly susceptible to significant amplitude modulation (AM) during its generation and propagation.[5–8] In addition to on-target uniformity, the smoothness of the pulsed beam as it propagates through the long laser amplifier chain is important because of the perennial concern regarding laser damage. Small-scale, nonlinear self-focusing can occur as the pulsed beam propagates through various optical components because of the large fluences inherent in ICF applications. Any AM, in space or time, present on the pulsed beam may induce self-focusing and lead to damage. OMEGA utilizes many spatial filters to help alleviate the buildup of high spatial frequencies that tend to self-focus. In an effort to reduce the overall AM, it is imperative that the AM produced by the SSD driver line is at an absolute minimum.

A complete analysis of the SSD driver line requires a model that accounts for diffraction and spatiotemporal spectral effects of the many optical components that comprise the driver during both the generation and propagation of 2-D SSD beams. AM sources and other nonideal behavior can occur at any point in the SSD driver line, and the impact of a particular optical component depends on its relative location and the parameters that describe the SSD operation. Laser beam propagation codes that include SSD as part of an entire ICF laser system modeling exist at other laboratories, for example, Prop92 at LLNL and Miró at CEA; however, they do not emphasize the underlying optical components in the SSD driver line. A comprehensive understanding of the AM issue and other nonideal behavior entails a rigorous examination of the specific optics involved in the SSD driver line, including the effects of multiple-layered dielectric media, crystal birefringence, multiple co-propagating beams, nonlinear grating behavior, and far-field distortion. A model must be able to simulate the nonideal effects, predict the relative impact, and characterize the behavior so that experimental measurements can be used to diagnose and excise the problem.

The code (Waasese) developed to address the AM issue in the SSD driver line simulates many optical components, predicts the degree of AM, and characterizes the AM mechanisms in terms of measurable signatures. Different AM sources are measured on near-field streak camera images and exhibit distinct spatiotemporal patterns, trends in the temporal spectrum, and/or AM that varies as a function of an SSD parameter. Waasese simulations associate these distinct characteristics or signatures to particular optic components. These signature/component relationships are then exploited to diagnose, locate, and eliminate the AM sources when used in conjunction with experimental measurements. Waasese has been successfully used to locate some AM sources and identify solutions in the new double-pass 2-D SSD driver line scheduled for installation on OMEGA. Waasese is based on the angular spectrum representation, which accurately models diffraction and spatiotemporal spectral effects. Waasese is not limited to AM issues and has been used to model observed far-field distortion. Waasese's inherent flexibility facilitates future enhancements as other laser propagation issues arise.

Waasese models the individual optical components of the SSD driver line using a transfer-function approach as opposed to applying the ideal spatiotemporal dependent phase term. An angular spectrum representation and/or a thin optic phase transformation describes the transfer functions of the optical components. This approach models SSD generation in a stepwise fashion so that nonideal components, such as wave plates, may be included at any point in the process such as in between the preshear and dispersion gratings. This is an important issue because the degree to which optical components contribute to AM depends on their relative location in the SSD driver line. For example, surface roughness of a far-field retro mirror of the second SSD dimension will produce AM on the first but not the second dimension because the second dimension has not been dispersed at this point. Also, the AM induced by the crystal birefringence of the second SSD dimension can be compensated, provided that re-imaging takes place prior to the final grating. Additional examples of the modeling capabilities of

Waasese include nonlinear behavior of gratings, multiple surface reflections from a crystal in combination with an end mirror that produce co-propagating beams with offset spatiotemporal spectra, angular-dependent phase modulation depth that produces distorted far-field spectra, multiple-layered dielectric coatings that model high-reflection (HR) or antireflection (AR) coatings, etalon effects that modulate the temporal spectrum, spatial phase modulation of irregular surfaces, and image rotation between grating pairs. Waasese is capable of modeling arbitrary initial spatial and temporal profiles such as Gaussian, hyperbolic tangent, square, round, and elliptical. A postprocessor for Waasese incorporates various instructional data-visualization techniques of the spatiotemporal intensity and phase history of 2-D SSD pulsed beams: a spatiotemporal cross section, a spatial cross section, a false-color instantaneous wavelength overlay, a time-averaged far-field view, and a time evolution of the far-field pattern. These data-visualization techniques provide valuable insight into various problems that arise and their subsequent solutions.

The angular spectrum representation provides a straightforward analytical and numerical method to accurately analyze the generation and propagation of 2-D SSD pulsed laser beams. The angular spectrum representation decomposes a pulsed beam into a continuous linear sum of harmonic plane waves that individually propagate with a unique direction and temporal frequency through the laser system. Each harmonic plane wave is completely described by three parameters: k_x, k_y, and ω. When the resultant harmonic plane waves are summed, a representation of a 2-D SSD pulsed laser beam is obtained that accurately models diffraction and spatiotemporal spectral effects. Certain optical components require a thin optic phase transformation operation, in real space, whenever the optical surfaces are not planar, e.g., lenses, irregular surfaces on mirror coatings, and surface roughness of optical finishing.

In this article we first describe the angular spectrum representation of the two main elements of the SSD operation used in Waasese: gratings and electro-optic (EO) phase modulators. We then apply these transfer functions to the ideal generation of 2-D SSD, which provides a foundation of comparison for the nonideal cases. Ideal 2-D SSD utilizes a linearized grating equation and a pure phase-modulation operation. Analytical expressions and Waasese demonstrate that the application of the ideal transfer functions reduces the problem to the well-known spatiotemporal-dependent phase term that describes 2-D SSD.[1,2] We also introduce the frequency domain and real-space data visualization capabilities of the Waasese postprocessor. Finally in a section covering nonideal 2-D SSD generation we discuss various errors and/or nonideal effects that include nonideal gratings, nonideal phase modulators, crystal birefringence, Littrow mount error, image rotation, temporal spectrum modulation, spatial spectrum modulation, and image-plane errors.

Angular Spectrum Representation

Consider the electromagnetic field of the pulsed laser beam that propagates along the beam axis $\hat{\mathbf{z}}$ within a nonmagnetic, nonconducting, source-free, linear, causal, spatially and temporally homogeneous, isotropic, and spatially and temporally locally linear dielectric medium described by a constant refractive index $n \equiv \sqrt{\mu\varepsilon/\mu_0\varepsilon_0}$. Let the electric field $\mathbf{E}'(\mathbf{r},t)$ of the pulsed laser beam be defined on an image plane at $z = z_0$:

$$\mathbf{E}_0{}'(\mathbf{r}_T,t) \equiv \mathbf{E}'(\mathbf{r},t)\Big|_{z=z_0}, \tag{1}$$

where the position vector and transverse position vector are defined, respectively, by

$$\mathbf{r} \equiv x\hat{\mathbf{x}} + y\hat{\mathbf{y}} + z\hat{\mathbf{z}} \tag{2}$$

and

$$\mathbf{r}_T \equiv x\hat{\mathbf{x}} + y\hat{\mathbf{y}} \tag{3}$$

in the right-handed rectangular coordinate system (x,*y*,*z*) with the corresponding unit vectors $(\hat{\mathbf{x}},\hat{\mathbf{y}},\hat{\mathbf{z}})$. In addition, let the pulsed laser beam possess the form of a modulated carrier of angular frequency ω_c:

$$\mathbf{E}_0{}'(\mathbf{r}_T,t) \equiv \mathbf{E}_0(\mathbf{r}_T,t)e^{i\omega_c t}, \tag{4}$$

where $\mathbf{E}_0(\mathbf{r}_T,t)$ is the spatiotemporal envelope of the pulsed beam. The angular spectrum of the electric field at the image plane is given by the forward, three-dimensional, spatial spatiotemporal Fourier-Laplace transform (compare Ref. 9, §5.1 and Ref. 10, Chap. 4):

$$\begin{aligned}\tilde{\mathbf{E}}_0(\mathbf{k}_T,\omega) &\equiv \tilde{\mathbf{E}}(\mathbf{k}_T,z_0,\omega)\\ &= \int_{-\infty}^{\infty}\!\!\int\!\!\int \mathbf{E}_0(\mathbf{r}_T,t)e^{i\omega t}e^{-i\mathbf{k}_T\cdot\mathbf{r}_T}\,dt\,dx\,dy.\end{aligned} \tag{5}$$

The wave vector and transverse wave vector are defined, respectively, as

$$\mathbf{k} \equiv k_x \hat{\mathbf{x}} + k_y \hat{\mathbf{y}} + k_z \hat{\mathbf{z}} \tag{6}$$

and

$$\mathbf{k}_T \equiv k_x \hat{\mathbf{x}} + k_y \hat{\mathbf{y}} \, , \tag{7}$$

where the transverse wave numbers or spatial frequencies k_x and k_y are real-valued and the longitudinal wave number k_z is given by the principle root of the expression

$$k_z \equiv \sqrt{k_0^2 n^2 - k_T^2} \, , \tag{8}$$

and $k_T^2 \equiv k_x^2 + k_y^2$. The quantity $k_0 \equiv 2\pi/\lambda = \omega'/c$ is the vacuum wave number, ω' is the angular frequency of the electromagnetic disturbance that is centered about the carrier ω_c,

$$\omega' \equiv \omega_c + \omega, \tag{9}$$

and $c \equiv 1/\sqrt{\mu_0 \varepsilon_0}$ is the vacuum speed of light.

Free-space propagation of the electric field of the pulsed laser beam along the beam axis in any source-free and homogenous region of dielectric is given exactly by the angular spectrum representation (compare Ref. 9, §5.1)

$$\mathbf{E}(\mathbf{r}_T, z, t) = \frac{1}{(2\pi)^3} \int\int\int_{-\infty}^{\infty} \tilde{\mathbf{E}}_0(\mathbf{k}_T, \omega) e^{i\Delta z k_z} e^{-i\omega t} e^{i\mathbf{k}_T \cdot \mathbf{r}_T} \, \mathrm{d}\omega \, \mathrm{d}k_x \mathrm{d}k_y \, , \tag{10}$$

where $\Delta z \equiv z - z_0$. The expression given in Eq. (10) is an exact solution to Maxwell's equations in an isotropic, source-free dielectric medium. Any inaccuracies associated with this method amount to assumptions made about the field behavior $\mathbf{E}_0(\mathbf{r}_T, t)$ on the initial plane $z = z_0$ (such as assuming scalar fields or Fresnel-Kirchoff boundary conditions) or when approximating the integrals as summations when performing numerical simulations. When $k_T^2 \le k_0^2 n^2$, the longitudinal wave number k_z is real-valued and the integrand of Eq. (10) represents homogenous plane waves with spectral amplitudes or angular spectra $\tilde{\mathbf{E}}_0(\mathbf{k}_T, \omega)$ whose phase fronts propagate in the direction given by the wave vector $\mathbf{k} \equiv k_x \hat{\mathbf{x}} + k_y \hat{\mathbf{y}} + k_z \hat{\mathbf{z}}$. Thus, the angular spectrum representation decomposes an arbitrary pulsed laser beam into a continuous sum of homogeneous plane waves that propagate in a unique direction and with an angular frequency ω'. The expression in Eq. (10) represents the general case of vectors and is certainly valid for each individual vector component; therefore it is applicable to the scalar diffraction problems presented in this article.

A useful measure that marks the boundary between the near field and far field for diffraction problems is the Rayleigh range given by (Ref. 11, p. 714)

$$z_R \equiv \frac{A}{\lambda_c} \, , \tag{11}$$

where A is the area of the beam (see Table 78.II for typical numbers on OMEGA). Another useful parameter is the Fresnel number given by

$$N \equiv \frac{a^2}{\lambda_c \Delta z} \, , \tag{12}$$

which measures the number of Fresnel zones contained within an aperture of width or diameter $2a$. For full-aperture illumination, the Fresnel number will determine the number of strong ripples apparent in the near-field diffraction pattern. However, a beam with a supergaussian profile or other rounded square shapes such as a hyperbolic-tangent will not exhibit these strong ripples (Ref. 11, p. 739). For this reason, the simulations presented here utilize these shapes to reduce the edge diffraction ripples in order to emphasize other diffraction effects. Waasese is based on the angular spectrum representation and is therefore inherently capable of modeling any beam shape or temporal profile.

Elements of the SSD Operation

The two basic elements of the SSD operation in terms of the angular spectrum representation—gratings and EO phase modulators—are presented as transfer functions in both real and frequency space to describe the complex 2-D SSD system as a set of interchangeable operations. This method also develops a sense of the resultant frequency-domain effects of each operation and its relation to the real space.

1. The Grating Equation

The grating equation relates an incident harmonic plane wave to a transmitted (or reflected) harmonic plane wave that is given by[12]

$$\sin(\theta_i) + \sin(\theta_t) = -m \frac{\lambda}{d} \, , \tag{13}$$

Table 78.II: The Rayleigh range Δz_R, the color-separation distance Δz_{crit}, and their ratio $\Delta z_{crit}/\Delta z_R$ for various beam diameters and two values of applied bandwidth for a dispersion of $d\theta_t/d\lambda$ = 197 μrad/Å and grating beam diameter $D_{grating}$ = 44 mm.

	Diameter (cm)								
	0.11	0.22	0.55	1.938	4.4	8.488	14.63	19.52	27.33
Δz_R (m)	0.902	3.608	22.55	280	1443	5371	15956	28405	55683
Δz_{crit} (m), 1.5 Å	0.186	0.745	4.653	57.77	297.8	1108.2	3292.4	5861.1	11489
$\Delta z_{crit}/\Delta z_R$	0.206	0.206	0.206	0.206	0.206	0.206	0.206	0.206	0.206
Δz_{crit} (m), 3.0 Å	0.093	0.372	2.327	28.89	148.9	554.12	1646.2	2930.6	5744.7
$\Delta z_{crit}/\Delta z_R$	0.103	0.103	0.103	0.103	0.103	0.103	0.103	0.103	0.103

where θ_i and θ_t are the incident and transmitted angles relative to the grating normal, m is the order of the grating, d is the groove spacing, $\lambda \equiv 2\pi c/\omega'$ is the wavelength, and $\omega' \equiv \omega_c + \omega$ is the angular frequency that is centered about the carrier ω_c. The gratings in the SSD driver lines at LLE are used in transmission mode with an order $m = -1$ (see Fig. 78.6). Solving Eq. (13) for θ_t with an order $m = -1$ yields

$$\theta_t = \sin^{-1}\left[\frac{\lambda}{d} - \sin(\theta_i)\right]. \tag{14}$$

Taking the derivative of Eq. (14) with respect to λ yields the grating dispersion

$$\frac{d\theta_t}{d\lambda} = \frac{1}{d\sqrt{1-\left[\frac{\lambda}{d} - \sin(\theta_i)\right]^2}} \ . \tag{15}$$

For the SSD laser systems at LLE, the gratings are typically in a Littrow mount, which is defined to be when the angles of the incident and transmitted plane waves are equal for a particular design wavelength, i.e., $\theta_{Litt} \equiv \theta_i = \theta_t$. Under this condition, an incident pulsed beam will retain its incident beam diameter and is described by

$$\sin(\theta_{Litt}) = \frac{\lambda_c}{2d} \ , \tag{16}$$

where $\lambda_c = 2\pi c/\omega_c$ is the central or design wavelength. Typically, the design parameters for a grating are the central wavelength λ_c and a desired amount of dispersion $d\theta_t/d\lambda$ while assuming a Littrow mount, which then determines the grating groove spacing d by substituting Eq. (16) into Eq. (15). Once a grating design is realized, an operating point has been determined on the $d\theta_t/d\lambda$ curve, which can be seen in the example illustrated in Fig. 78.7. When the bandwidth $\Delta\lambda$ that is induced by the SSD system is small enough, then the slope

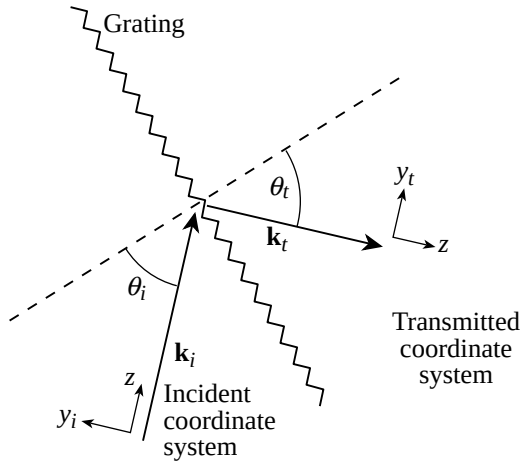

Figure 78.6
The coordinate systems for the incident and transmitted pulsed beams that traverse a grating in transmission mode of order $m = -1$. Notice that the beam axis (z) remains unaltered as a result of the grating operation; indicating the rotation from the incident to the transmitted coordinate system as the beam axis follows the course of the real beam.

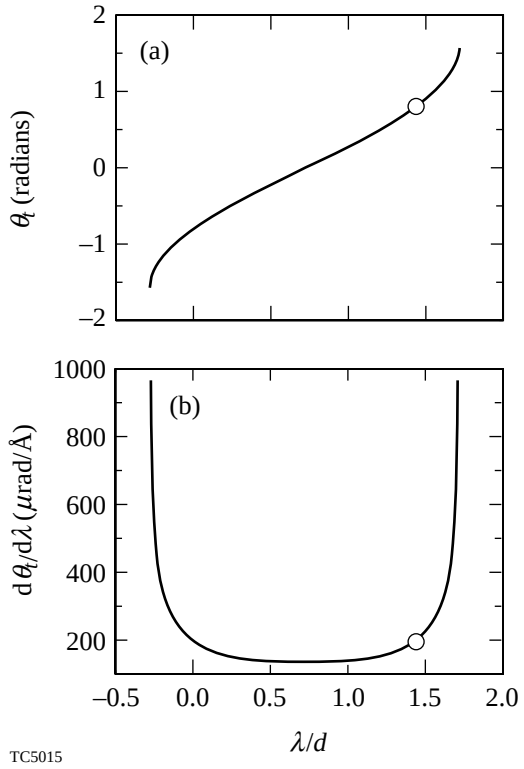

Figure 78.7
The design points on (a) the grating equation θ_t and (b) the grating dispersion equation $d\theta_t/d\lambda$ for λ_c = 1053 nm, $\theta_{L\,itt}$ = 46°, and d = 0.732 μm/groove.

$d\theta_t/d\lambda$ is nearly constant over that bandwidth; however, since Eq. (15) is inherently nonlinear, beam distortion becomes more significant as the bandwidth increases.

Consider an incident modulated pulsed laser beam with an angular carrier frequency of ω_c, pulse duration τ, and diameter D impinging upon a grating that disperses along the $\hat{\mathbf{y}}$ direction. Define the incident beam axis (z) to make an angle Θ_i with regard to the grating normal in the y-z plane. Then define a transmitted-beam axis that makes an angle Θ_t with regard to the grating normal. (This situation is illustrated in Fig. 78.6.) By decomposing the incident pulsed laser beam into its angular spectrum, the grating equation (14) may be used to accurately describe the action of the grating in the spatiotemporal frequency space. The grating acts as an angular transformation operation that redirects or maps each incident plane wave (completely described by the parameters k_x, k_y, and ω) onto the transmitted-beam axis. Notice that the image plane will be rotated onto the transmitted-beam axis as indicated in Fig. 78.6. Only the wave number in the $\hat{\mathbf{y}}$ direction is altered during this transformation, and, in general, the new transverse wave number is a function of both the transverse wave number and the angular frequency, i.e., $k_{y_g}\left(k_y,\omega\right)$. The transformation operation $k_{y_g}\left(k_y,\omega\right)$ is referred to as the grating angular dispersion, which acts along the $\hat{\mathbf{y}}$ direction as denoted by the subscript y. The grating angular dispersion may be expressed as [compare Eq. (14)]

$$k_{y_g}\left(k_y,\omega\right) = k_0 n \sin\left\{\Theta_t - \sin^{-1}\left[\frac{\lambda}{d} - \sin\left(\Theta_i + \sin^{-1}\left\{\frac{k_y}{k_0 n}\right\}\right)\right]\right\}, \qquad (17)$$

where $k_0 \equiv \omega'/c$, $\lambda \equiv 2\pi c/\omega'$, and $\omega' \equiv \omega_c + \omega$. The electric field of the transmitted pulsed laser beam is expressed, in general, by

$$E_g\left(\mathbf{r}_T,t\right) = \frac{1}{(2\pi)^3}\int\int\int_{-\infty}^{\infty} \tilde{E}_g\left(\mathbf{k}_T,\omega\right) e^{-i\omega t} e^{i\mathbf{k}_T\cdot\mathbf{r}_T}\, d\omega\, dk_x\, dk_y \qquad (18)$$

with the associated distorted angular spectrum given by

$$\tilde{E}_g\left(k_T,\omega\right) = \tilde{E}_0\left(k_x, k_{y_g}, \omega\right). \qquad (19)$$

The action of the grating may be interpreted as a nonlinear mapping of the angular spectrum onto a new spectral grid, which is nonuniform in general. Consequently, in general, Eq. (18) is not suitable for fast Fourier transform (FFT) algorithms, and a proper treatment requires a slow Fourier transform operation to regrid the data. Under certain approximations, however, Eq. (18) is suitable for FFT algorithms, which are then used to regrid the angular spectrum back onto the original grid: first, assuming that the angular dispersion is a linear function of the transverse wave number k_y and, second, assuming an additional linear dependence of the temporal frequency ω. Waasese can be configured to run in any of these three modes to calculate the grating effects where a tradeoff of speed versus accuracy must be made.

The first assumption may be expressed as a first-order Taylor series expansion about the transverse wave number k_y:

$$k_{y_g}\left(k_y,\omega\right) = k_{y_g}\left(k_y,\omega\right)\Big|_{k_y=0} + k_y \frac{\partial}{\partial k_y} k_{y_g}\left(k_y,\omega\right)\Big|_{k_y=0}. \qquad (20)$$

The partial derivative in Eq. (20) is given by

$$\frac{\partial}{\partial k_y} k_{y_g}\left(k_y,\omega\right) = \frac{\cos\left\{\Theta_t - \sin^{-1}\left[\frac{\lambda}{d} - \sin\left(\Theta_i + \sin^{-1}\left\{\frac{k_y}{k_0 n}\right\}\right)\right]\right\}}{\sqrt{1-\left[\frac{\lambda}{d} - \sin\left(\Theta_i + \sin^{-1}\left\{\frac{k_y}{k_0 n}\right\}\right)\right]^2}} \times \frac{\cos\left(\Theta_i + \sin^{-1}\left\{\frac{k_y}{k_0 n}\right\}\right)}{\sqrt{1-\left[\frac{k_y}{k_0 n}\right]^2}} . \quad (21)$$

If the grating is in the Littrow mount and is tuned to the center frequency ω_c, then evaluating the partial derivative at $k_y = 0$ yields

$$k_{y_g}\left(k_y,\omega\right)\Big|_{k_y=0} = k_0 n \sin\left\{\Theta_t - \sin^{-1}\left[\frac{\lambda}{d} - \sin\left(\Theta_i\right)\right]\right\} , \quad (22)$$

and while assuming that $\omega' \cong \omega_c$,

$$\frac{\partial}{\partial k_y} k_{y_g}\left(k_y,\omega\right)\Big|_{k_y=0} \cong 1. \quad (23)$$

Substituting Eqs. (22) and (23) into Eq. (20) gives

$$k_{y_g}\left(k_y,\omega\right) = \hat{k}_{y_g} + k_y , \quad (24)$$

where $\hat{k}_{y_g}(\omega) \equiv k_{y_g}(0,\omega)$. A change of variables defined by Eq. (24) yields [compare Eq. (18)]

$$E_g\left(\mathbf{r}_T,t\right) = \frac{1}{(2\pi)^3}\int\int\int_{-\infty}^{\infty}\left\{\tilde{E}_0\left(k_x,k_{y_g},\omega\right) \times e^{-i\omega t} e^{i\left[k_x x + k_{y_g} y - \hat{k}_{y_g}(\omega) y\right]}\right\} \mathrm{d}\omega\,\mathrm{d}k_x\,\mathrm{d}k_{y_g}. \quad (25)$$

Since $\hat{k}_{y_g}$ is only a function of the temporal angular frequency ω, the inverse 2-D spatial Fourier transform operation yields

$$E_g\left(\mathbf{r}_T,t\right) = \frac{1}{2\pi}\int_{-\infty}^{\infty}\tilde{E}_0\left(\mathbf{r}_T,\omega\right)e^{-i\omega t} e^{-i\hat{k}_{y_g}(\omega) y}\mathrm{d}\omega , \quad (26)$$

where

$$\tilde{E}_0\left(\mathbf{r}_T,\omega\right) = \frac{1}{(2\pi)^2}\iint_{-\infty}^{\infty}\tilde{E}_0\left(\mathbf{k}_t,\omega\right)e^{i\mathbf{k}_T\cdot\mathbf{r}_T}\mathrm{d}k_x\mathrm{d}k_y . \quad (27)$$

The distorted angular spectrum is then given by

$$\tilde{E}_g\left(\mathbf{k}_T,\omega\right) = \iint_{-\infty}^{\infty}\tilde{E}_0\left(\mathbf{r}_T,\omega\right)e^{i\hat{k}_{y_g}(\omega) y} e^{-i\mathbf{k}_T\cdot\mathbf{r}_T}\mathrm{d}x\mathrm{d}y = \int_{-\infty}^{\infty}\tilde{E}_0\left(k_x,y,\omega\right)e^{-i\hat{k}_{y_g}(\omega) y - ik_y y}\mathrm{d}y. \quad (28)$$

The utility of Eq. (28) lies in the ability to regrid the angular spectrum using conventional FFT algorithms. Waasese applies three operations to the initial angular spectrum $\tilde{E}_0\left(\mathbf{k}_T,\omega\right)$ to regrid the distorted angular spectrum $\tilde{E}_g\left(\mathbf{k}_T,\omega\right)$ onto the original numerical grid: inverse spatially transform the k_y dimension, apply the distortion term

$$e^{-i\hat{k}_{y_g}(\omega) y},$$

and, finally, forward spatially transform the y dimension.

The second assumption may be expressed as a bivariate, first-order Taylor series expansion:

$$k_{y_g}\left(k_y,\omega\right) = k_{y_g}\left(k_y,\omega\right)\Big|_{k_y=0,\omega=0} + k_y\frac{\partial}{\partial k_y}k_{y_g}\left(k_y,\omega\right)\Big|_{k_y=0,\omega=0} + \omega\frac{\partial}{\partial\omega}k_{y_g}\left(k_y,\omega\right)\Big|_{k_y=0,\omega=0}, \quad (29)$$

where $\omega' \equiv \omega_c + \omega$. The partial derivative with regard to ω in Eq. (29) is given by

$$\frac{\partial}{\partial\omega} k_{y_g}\left(k_y,\omega\right)$$

$$= \frac{1}{c}\sin\left\{\Theta_t - \sin^{-1}\left[\frac{\lambda}{d} - \sin\left(\Theta_i + \sin^{-1}\left\{\frac{k_y}{k_0 n}\right\}\right)\right]\right\}$$

$$+ k_0 n \frac{\cos\left\{\Theta_t - \sin^{-1}\left[\frac{\lambda}{d} - \sin\left(\Theta_i + \sin^{-1}\left\{\frac{k_y}{k_0 n}\right\}\right)\right]\right\}}{\sqrt{1-\left[\frac{\lambda}{d} - \sin\left(\Theta_i + \sin^{-1}\left\{\frac{k_y}{k_0 n}\right\}\right)\right]^2}}$$

$$\times \left[\frac{\lambda}{\omega' d} - \frac{\cos\left(\Theta_i + \sin^{-1}\left\{\frac{k_y}{k_0 n}\right\}\right)}{\sqrt{1-\left[\frac{k_y}{k_0 n}\right]^2}} - \frac{k_y}{k_0 \omega'}\right]. \quad (30)$$

If the grating is in a Littrow mount tuned to the center frequency ω_c, then

$$k_{y_g}\left(k_y,\omega\right)\Big|_{k_y=0,\omega=0} = 0, \quad (31)$$

$$\frac{\partial}{\partial k_y} k_{y_g}\left(k_y,\omega\right)\Big|_{k_y=0,\omega=0} = 1, \quad (32)$$

and

$$\frac{\partial}{\partial\omega} k_{y_g}\left(k_y,\omega\right)\Big|_{k_y=0,\omega=0} = \frac{1}{d\sqrt{1-\left[\frac{\lambda_c}{d} - \sin\left(\Theta_i\right)\right]^2}} \frac{\lambda_c}{c}. \quad (33)$$

Equation (29) can then be written as

$$k_{y_g}\left(k_y,\omega\right) = k_y + \xi_g \omega \quad (34)$$

and is known as the linearized grating angular dispersion, where Eq. (15) has been used in the definition

$$\xi_g \equiv \frac{\lambda_c}{c}\frac{\mathrm{d}\theta_t}{\mathrm{d}\lambda}\bigg|_{\omega=0,\theta_i=\Theta_i}.$$

The transmitted pulsed laser beam then becomes a temporally skewed or sheared version of the incident pulsed beam:

$$E_g\left(\mathbf{r}_T,t\right) = \frac{1}{2\pi}\int_{-\infty}^{\infty}\tilde{E}_0\left(\mathbf{r}_T,\omega\right)e^{-i\omega\left(t-\xi_g y\right)}\mathrm{d}\omega$$

$$= E_0\left(\mathbf{r}_T, t-\xi_g y\right), \quad (35)$$

where a temporal delay is imposed across the beam by an amount defined by

$$\tau_D = \xi_g D. \quad (36)$$

The angular spectrum is also sheared and is given by

$$\tilde{E}_g\left(\mathbf{k}_T,\omega\right) = \tilde{E}_0\left(k_x, k_y + \xi_g\omega, \omega\right). \quad (37)$$

During numerical simulations, Waasese regrids the initial angular spectrum $\tilde{E}_0\left(\mathbf{k}_T,\omega\right)$ using the technique described in association with Eq. (28).

2. The EO Phase Modulator

A strong microwave or radio frequency (RF) field inside a cavity resonator can modulate the optical refractive index of a nonlinear crystal such as lithium niobate ($LiNbO_3$).[13] The ideal EO phase modulator operates only in the time domain by applying the sinusoidal time-varying phase function $e^{i\delta_M \sin\left(\omega_M t\right)}$ to the optical electric field as

$$E_M\left(\mathbf{r}_T,t\right) = E_0\left(\mathbf{r}_T,t\right)e^{i\delta_M\sin\left(\omega_M t\right)}, \quad (38)$$

where δ_M is the modulation depth and $\upsilon_M \equiv \omega_M/2\pi$ is the RF modulation frequency. This modulation scheme is referred to as pure-tone phase modulation that is a specific type of a general class known as exponential or angle modulation and is inherently a nonlinear process. In general, the bandwidth applied by phase modulation has infinite extent, and discarding any portion will result in distortion and a degradation of signal fidelity, e.g., AM. Practically, the significant bandwidth applied by phase modulation is concentrated in a finite spectral region, which is a function of the modulation depth δ_M. The question then becomes How much bandwidth is required to retain adequate signal integrity? (See Carlson Ref. 14, pp. 239–245 for an in-depth discussion.)

The applied bandwidth is estimated by Carson's rule:

$$\Delta\upsilon = \frac{\Delta\omega}{2\pi} \approx 2\left(\delta_{\mathrm{M}} + 1\right)\upsilon_{\mathrm{M}} \ , \tag{39}$$

which appropriately goes to the limiting cases.

$$\Delta\upsilon = \begin{cases} 2\delta_{\mathrm{M}}\upsilon_{\mathrm{M}} & \delta_{\mathrm{M}} >> 1 \\ 2\upsilon_{\mathrm{M}} & \delta_{\mathrm{M}} << 1 \end{cases} ; \tag{40}$$

however, Carson's rule underestimates the bandwidth for the range $2 < \delta_{\mathrm{M}} < 10$. The bandwidth is more accurately estimated by

$$\Delta\upsilon \approx 2\left(\delta_{\mathrm{M}} + 2\right)\upsilon_{\mathrm{M}} \tag{41}$$

for modulation depths $\delta_{\mathrm{M}} > 2$. The applied bandwidth may also be expressed in terms of the wavelength as

$$\Delta\lambda = 2\left(\lambda_c - \frac{c}{\dfrac{c}{\lambda_c} - \dfrac{\Delta\upsilon}{2}}\right) \cong \frac{\Delta\upsilon\lambda_c^2}{c} \ , \tag{42}$$

where any estimate for $\Delta\upsilon$ can be applied. Typically, the estimate for the bandwidth given by $2\delta_{\mathrm{M}}\upsilon_{\mathrm{M}}$ is quoted in the literature on SSD applications (even for modulation depths $\delta_{\mathrm{M}} < 10$). This convention will be followed in this article for consistency not accuracy.

Equation (38) can be written as an equivalent series expansion given by (compare Ref. 14, p. 228)

$$E_{\mathrm{M}}\left(\mathbf{r}_T, t\right) = E_0\left(\mathbf{r}_T, t\right) \sum_{l=-\infty}^{\infty} J_l\left(\delta_{\mathrm{M}}\right) e^{il\omega_{\mathrm{M}}t} . \tag{43}$$

The spatiotemporal Fourier-Laplace transform of Eq. (43) yields the replicated angular spectrum

$$\tilde{E}_{\mathrm{M}}\left(k_T, \omega\right) = \tilde{E}_0\left(k_T, \omega\right) * \sum_{l=-\infty}^{\infty} J_l\left(\delta_{\mathrm{M}}\right) \delta\left(\omega - l\omega_{\mathrm{M}}\right) \ . \tag{44}$$

The original angular spectrum $\tilde{E}\left(k_T, \omega\right)$ is replicated with a spacing of ω_{M} and amplitudes determined by the Bessel functions of the first kind $J_l\left(\delta_{\mathrm{M}}\right)$ by virtue of the convolution process denoted in Eq. (44) by the symbol $*$. If the original bandwidth is not small compared to the modulation frequency, some overlap will exist from one band to the next. As long as the overlap is small, which is generally the case for well-defined systems, the spectral peaks will be well defined. Even if overlap does occur, it does not affect the validity of the linear superposition implied by Eq. (44). Figure 78.8(a) illustrates a spectrum obtained for a 1-ns pulse using the parameters $\delta_{\mathrm{M}} = 6.15$ and $\nu_{\mathrm{M}} = 3.3$ GHz.

Like any form of exponential modulation, pure-tone phase modulation possesses the unique property of constant amplitude. Maintaining a constant amplitude with a sinusoidal phase variation is best understood using a phasor interpretation where phasors for the carrier plus every sideband are vector-summed in phasor space as illustrated in Fig. 78.9. The resultant phasor sinusoidally sweeps back and forth (by an amount determined by the modulation depth δ_{M}) in phasor space while maintaining constant amplitude. All of the odd-order sideband pairs are in phase quadrature (due to the fact that the components of an odd-order pair have equal magnitude with opposite sign, i.e., $J_{-1}\left(\delta_{\mathrm{M}}\right) = (-1)^l J_l\left(\delta_{\mathrm{M}}\right)$ [see Ref. 15, p. 258, Eq. (9.1.5)], and all of the even-order sideband pairs

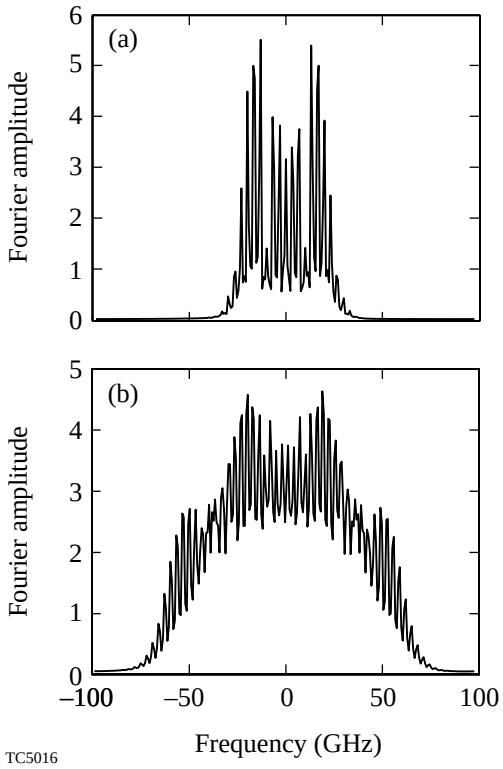

Figure 78.8
The temporal spectrum for (a) a pure-tone and (b) a two-tone phase-modulated optical pulse. The pulse duration is $\tau = 1$ ns and the parameters are $\delta_{\mathrm{M1}} = 6.15$, $\nu_{\mathrm{M1}} = 3.3$ GHz, $\Delta\lambda_{\mathrm{M1}} = 1.5$ Å, $\delta_{\mathrm{M2}} = 13.5$, $\nu_{\mathrm{M2}} = 3.0$ GHz, and $\Delta\lambda_{\mathrm{M2}} = 3.0$ Å.

are collinear with regard to the carrier. The odd-order pairs contribute to the desired sinusoidal phase modulation plus unwanted amplitude modulation. The even-order pairs compensate for the unwanted amplitude modulation imposed by the odd-order pairs (see pp. 230–233 of Ref. 14 for a complete discussion). The constant amplitude inherent in phase modulation relies on the delicate balance of the amplitudes and phases of its spectral components. Any deviation in this balance results in distortion that can exhibit itself as AM.

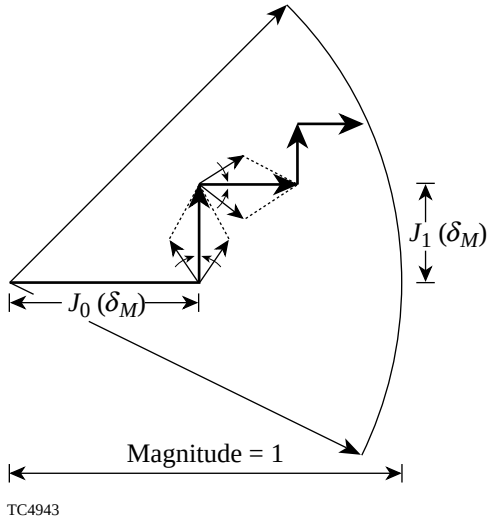

Figure 78.9
Phasor diagram of pure-tone phase modulation that depicts the phasor pairs for a small modulation depth. The diagram depicts how the even-order pairs compensate for the unwanted amplitude modulation imparted by the odd-order pairs. (Adapted from Ref. 14, p. 232, Fig. 6.7.)

Ideal 2-D SSD Generation

Here we describe the step-by-step process that Waasese uses to generate 2-D SSD. Ideal 2-D SSD is produced when the transfer functions given by Eqs. (37) and (44) are used. Analytical expressions are also developed and are shown to be equivalent to a generalization of Ref. 3, which includes beam shape. Ideal 2-D SSD is generated by a series of two ideal 1-D SSD operations performed on the two orthogonal transverse spatial directions of a seed-pulsed laser beam. Each 1-D SSD operation consists of an EO phase modulator sandwiched between a grating pair, such that an image plane exists at each grating plane. The angular spectrum representation of the grating and EO modulator, developed in the previous section, is drawn upon to illustrate the frequency-domain effects and how they relate to real space.

1. 1-D SSD Operation

Since each of the gratings is assumed to be at an image plane, this implies that some kind of image-relaying system must be in place. For practical SSD systems, these are afocal image relay telescopes with slow lenses that do not contribute significant aberrations. Figure 78.10 depicts the 1-D SSD

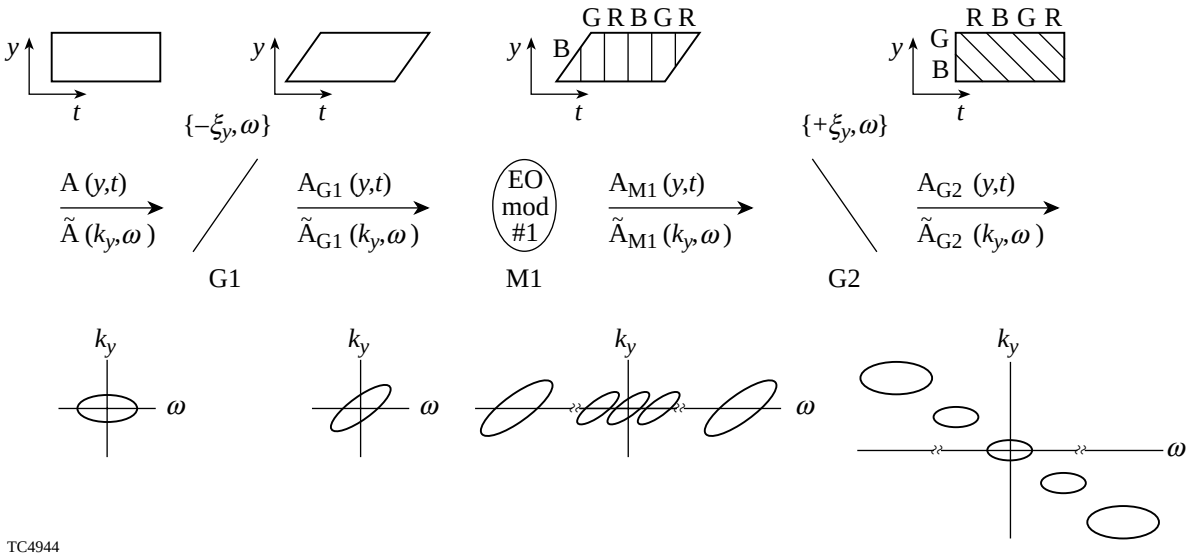

Figure 78.10
A schematic representation of the 1-D SSD operation showing the two important functions: gratings and EO phase modulator. In addition, the image planes are indicated along with the function names and a rough sketch of the field shape, in both real and frequency space, after each operation.

operation with the three major components, including the field names at certain locations. If the bandwidth $\Delta\lambda$ (typically 1 Å $< \Delta\lambda <$ 12 Å) introduced by the SSD system is small relative to the operating wavelength λ_c (for OMEGA the IR wavelength is 1053 nm), then the linearized grating angular dispersion Eq. (34) is an adequate representation of the grating and serves this section by demonstrating the ideal or desired response of an SSD system.

Consider a seed-modulated pulsed laser beam with an angular carrier frequency of ω_c, pulse duration τ, and diameters D_y and D_x. The electric field is defined on an image plane as $E_0(\mathbf{r}_T, t)$ with the associated angular spectrum $\tilde{E}_0(\mathbf{k}_T, \omega)$ and is image relayed onto the input of grating G1. Let the first grating G1 preshear the pulsed beam with a linearized angular dispersion of $-\xi_y$ along the $\hat{\mathbf{y}}$ direction. Consequently, the sheared field after the grating G1 is given by [compare Eq. (35)]

$$E_{\mathrm{G1}}(\mathbf{r}_T, t) = E_0(\mathbf{r}_T, t + \xi_y y), \tag{45}$$

where a temporal delay is imposed across the field by an amount given by $\tau_{D_y} = \xi_y D_y$. The angular spectrum is also sheared and is given by [compare Eq. (37)]

$$\tilde{E}_{\mathrm{G1}}(\mathbf{k}_T, \omega) = \tilde{E}_0(k_x, k_y - \xi_y\omega, \omega), \tag{46}$$

where the angular spectrum has been distorted only in the direction parallel to the k_y axis by the quantity $\xi_y\omega$. A representation of the sheared field and angular spectrum is illustrated in Fig. 78.10. Let the EO phase modulator have a modulation depth of δ_{M1} and a RF modulation frequency of $\upsilon_{\mathrm{M1}} = \omega_{\mathrm{M1}}/2\pi$. By combining the results from Eqs. (43) and (45), the electric field becomes

$$\begin{aligned} E_{\mathrm{M1}}(\mathbf{r}_T, t) &= E_{\mathrm{G1}}(\mathbf{r}_T, t) e^{i\delta_{\mathrm{M1}}\sin(\omega_{\mathrm{M1}}t)} \\ &= E_{\mathrm{G1}}(\mathbf{r}_T, t) \sum_{l=-\infty}^{\infty} J_l(\delta_{\mathrm{M1}}) e^{il\omega_{\mathrm{M1}}t} \end{aligned} \tag{47}$$

and the replicated-sheared angular spectrum is given by

$$\tilde{E}_{\mathrm{M1}}(\mathbf{k}_T, \omega) = \tilde{E}_{\mathrm{G1}}(\mathbf{k}_T, \omega) * \sum_{l=-\infty}^{\infty} J_l(\delta_{\mathrm{M1}}) \delta(\omega - l\omega_{\mathrm{M1}}). \tag{48}$$

A representation of the phase-modulated sheared field and angular spectrum is illustrated in Fig. 78.10. The second grating G2 now acts to disperse the increased bandwidth and remove the preshear from the first grating G1. Let the linearized angular dispersion be of equal magnitude and in the same direction as the first grating but with opposite sign, i.e., $+\xi_y$ (this is realized through the image flip of an odd number of image relays), so that the electric field becomes

$$E_{\mathrm{G2}}(\mathbf{r}_T, t) = E_{\mathrm{M1}}(\mathbf{r}_T, t - \xi_y y), \tag{49}$$

and the unsheared angular spectrum is given by

$$\tilde{E}_{\mathrm{G2}}(\mathbf{k}_T, \omega) = \tilde{E}_{\mathrm{M1}}(k_x, k_y + \xi_y\omega, \omega). \tag{50}$$

After substituting the results of Eqs. (45)–(47)

$$\begin{aligned} E_{\mathrm{G2}}(\mathbf{r}_T, t) &= E_{\mathrm{G1}}(\mathbf{r}_T, t - \xi_y y) e^{i\delta_{\mathrm{M1}}\sin\left[\omega_{\mathrm{M1}}(t+\xi_y y)\right]} \\ &= E_0(\mathbf{r}_T, t) e^{i\delta_{\mathrm{M1}}\sin\left[\omega_{\mathrm{M1}}(t+\xi_y y)\right]} \\ &= E_0(\mathbf{r}_T, t) \sum_{l=-\infty}^{\infty} J_l(\delta_{\mathrm{M1}}) e^{il\omega_{\mathrm{M1}}(t+\xi_y y)}. \end{aligned} \tag{51}$$

The angular spectrum of the 1-D SSD operation is then given by the spatiotemporal Fourier-Laplace transform of Eq. (51):

$$\begin{aligned} \tilde{E}_{\mathrm{G2}}(\mathbf{k}_T, \omega) &= \tilde{E}_0(\mathbf{k}_T, \omega) \\ &\quad * \sum_{l=-\infty}^{\infty} J_l(\delta_{\mathrm{M1}}) \delta(k_x, k_y - l\xi_y\omega_{\mathrm{M1}}, \omega + l\omega_{\mathrm{M1}}), \end{aligned} \tag{52}$$

where it is important to notice that exact replicas of the original spectrum, modified only by the amplitude of the Bessel functions of the first kind $J_l(\delta_{\mathrm{M1}})$, are centered on a regularly spaced line or comb of delta functions described by the summation operation. The comb of delta functions lies along the line $k_y = \xi_y\omega$ on the $k_y - \omega$ plane of the 3-D spatiotemporal spectrum and are spaced by $\xi_y\omega_{\mathrm{M1}}$ on the k_y axis and ω_{M1} on the ω axis. A representation of the final field and angular spectrum is illustrated in Fig. 78.10. Each replica of the original angular spectrum in Eq. (52) can be interpreted as an individual colored-pulsed beam with an associated wavelength or color $\lambda \equiv 2\pi c/\omega'$, where $\omega' = \omega_c + l\omega_{\mathrm{M1}}$, whose phase front advances in the direction $\mathbf{k} \equiv k_x\hat{\mathbf{x}} + (k_y - l\xi_y\omega_{\mathrm{M1}})\hat{\mathbf{y}} + k_z\hat{\mathbf{z}}$.

It is important to notice that, for propagation distances $\Delta z << z_R$ (such that minimal edge diffraction takes place for rounded square beams), the individual colored-pulsed beams retain their shape and continue to propagate along the beam axis and only the phase fronts break across the beam in a different direction. The individual colored beams will eventually separate since the energy flows along the direction **k**. The distance that colored-pulsed beam shifts in the transverse direction is given approximately by

$$\Delta y_l = \Delta z \tan\left(\Delta\theta_l\right), \tag{53}$$

where

$$\Delta\theta_l = \xi_g \frac{c}{\lambda_c} \Delta\lambda_l \frac{D_{\text{grating}}}{D}, \tag{54}$$

$\Delta\lambda_l \cong \left(\lambda_c^2/c\right) l \nu_{\text{M1}}$ is the spectral offset of a particular color, and D_{grating} is the beam diameter at the grating. The critical propagation distance for color separation is defined as when the outermost colored-pulsed beam has shifted by one beam diameter, i.e., $\Delta y = D_y$, and is approximated by

$$\Delta z_{\text{crit}} = \frac{D_y}{\tan(\Delta\theta)} \cong \frac{D_y}{\Delta\theta} = \frac{2}{\xi_g} \frac{\lambda_c}{c\Delta\lambda} \frac{{D_y}^2}{D_{\text{grating}}}, \tag{55}$$

where $\Delta\lambda$ is the applied bandwidth given by Eq. (42). The data in Table 78.II represents Δz_{R}, Δz_{crit}, and $\Delta z_{\text{crit}}/\Delta z_{\text{R}}$ for various OMEGA beam diameters for the system parameters: $\mathrm{d}\theta_t/\mathrm{d}\lambda\big|_{\omega=0} = 197\ \mu$rad/Å, $\Delta\lambda_{\text{M1}} = 1.5$ Å, 3.0 Å, and $D_{\text{grating}} = 44$ mm.

The electric field of a pulsed beam is a complex three-dimensional object whose intensity distribution, in space, is suitably described as a *brick of light* that moves along the propagation axis at the group velocity of the pulse. At one position of the propagation axis, the intensity of the brick of light is distributed about the transverse spatial dimensions as described by the beam profile and in time as described by the pulse shape. Taking different kinds of cross sections or slices of the brick of light is a way to visualize the multidimensioned data. A spatiotemporal cross section illustrates the intensity history of the pulsed beam. As an example, a spatiotemporal slice of a 1-D SSD pulsed laser beam is shown in Fig. 78.11 for two orthogonal directions with the system parameters $\delta_{\text{M1}} = 6.15$, $\nu_{\text{M1}} = 3.3$ GHz, $\Delta\lambda_{\text{M1}} = 1.5$ Å, $\tau = 1$ ns, $D_y = D_x = 44$ mm, and where stepped hyperbolic-tangent profiles were used in the spatial and temporal dimensions. In addition a false-color representation of the instantaneous wavelength is defined by

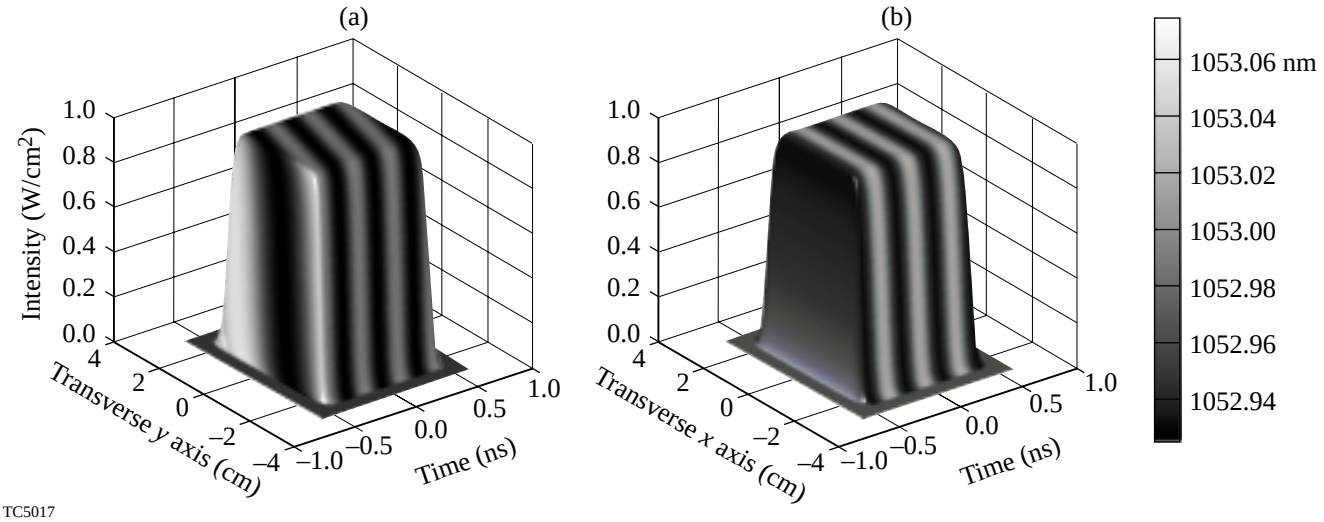

Figure 78.11
Spatiotemporal slices along (a) the *y*-*t* plane and (b) the *x*-*t* plane of a 1-D SSD pulsed beam with an overlay of the instantaneous wavelength $\hat{\lambda}\left(\mathbf{r}_T, t\right)$ superimposed onto the intensity profile for the system parameters $\delta_{\text{M1}} = 6.15$, $\nu_{\text{M1}} = 3.3$ GHz, $\Delta\lambda_{\text{M1}} = 1.5$ Å, $\tau = 1$ ns, $N_{c_y} \cong 1$, $\tau = 1$ ns, $D_y = D_x = 44$ mm, and where hyperbolic-tangent profiles were used in the spatial and temporal dimensions.

$$\hat{\lambda}(\mathbf{r}_T,t) \equiv \frac{c}{\frac{c}{\lambda_c} - \hat{\nu}} \ , \tag{56}$$

where the instantaneous frequency is given by

$$\hat{\nu} \equiv \frac{1}{2\pi}\frac{\partial \varphi}{\partial t} \tag{57}$$

and φ is the instantaneous phase of the field of the form $e^{i\varphi(y,t)}e^{i\omega_c t}$. The instantaneous wavelength is shown mapped onto the 3-D intensity surface, in effect, displaying the phase information of the electric field as a fourth dimension of data. The resultant dispersed spectrum of the 1-D SSD operation is displayed across the beam as one cycle of instantaneous wavelength or color, i.e., every color is displayed twice as the RF phase modulation cycles through 2π radians. In general, the fraction of RF phase-modulation cycles completed during the temporal shear $\tau_{D_y} = \xi_y D_y$, imposed by the first grating G1, and displayed across the beam as a result of the second grating G2, is determined by the number of color cycles (compare to Ref. 1):

$$N_{c_y} \equiv \tau_{D_y} \nu_{\mathrm{M1}} \, . \tag{58}$$

The instantaneous wavelength (or color) is not to be confused with the discrete colored-pulsed beams mentioned in the previous paragraph; the instantaneous wavelength is a continuous function defined in the temporal domain, whereas the other forms a discrete set defined in the temporal frequency domain. The bandwidth of the instantaneous frequency is given by

$$\Delta\hat{\nu} \equiv 2\delta_{\mathrm{M1}}\nu_{\mathrm{M1}} \, . \tag{59}$$

Notice that no approximation is made here as compared to the frequency-domain bandwidth described by Eqs. (39) and (41), and that it equals the bandwidth in the limit of large modulation depths given by Eq. (40). This fact illustrates the important difference between the instantaneous frequency and that of the frequency domain. When used with care, however, the instantaneous frequency is useful in describing some optical effects (such as etalons) since the modulation rate is slow compared to the underlying optical carrier. Another very important difference is that $\hat{\lambda}(\mathbf{r}_T,t)$ is a smooth, continuous function, and the frequency-space spectrum is comprised of a discrete set of frequencies (broadened only by the finite duration of the pulse width) as described by Eq. (44).

2. Series of Two 1-D SSD Operations

Consider, in a manner analogous to the previous subsection, a seed-modulated pulsed laser beam with an angular carrier frequency ω_c, pulse duration τ, and diameters D_y and D_x. The electric field is defined on an image plane as $E_0(\mathbf{r}_T,t)$ with the associated angular spectrum $\tilde{E}_0(\mathbf{k}_T,\omega)$ and is image relayed onto the input of grating G1. A diagram of the 2-D SSD system is shown in Fig. 78.12. Let the first SSD operation be given by Eqs. (51) and (52). Let the first grating of the second-dimension G3 operation preshear the pulsed beam with a linearized angular dispersion of $-\xi_x$ along the direction $\hat{\mathbf{x}}$. Consequently, the sheared field after the grating G3, in terms of the results from the first dimension Eq. (35), is given by

$$E_{\mathrm{G3}}(\mathbf{r}_T,t) = E_{\mathrm{G2}}(\mathbf{r}_T, t+\xi_x x) \ , \tag{60}$$

where a temporal delay imposed across the field is an amount given by $\tau_{D_y} = \xi_x D_x$. The sheared angular spectrum is given by [compare Eq. (37)]

$$\tilde{E}_{\mathrm{G3}}(\mathbf{k}_T,\omega) = \tilde{E}_{\mathrm{G2}}(k_x - \xi_x\omega, k_y, \omega), \tag{61}$$

where the angular spectrum has been distorted only in the direction parallel to the k_x axis by the quantity δ_{M2}. Let the second EO phase modulator have a modulation depth of δ_{M2} and a RF modulation frequency of $\upsilon_{\mathrm{M2}} = \omega_{\mathrm{M2}}/2\pi$. The electric field becomes

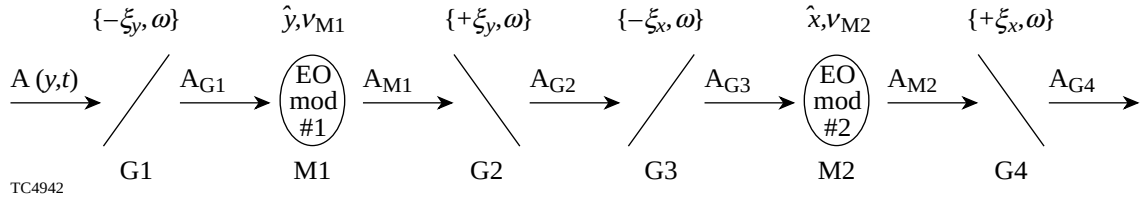

Figure 78.12
A schematic representation of the 2-D SSD operation, which exhibits a series of two 1-D SSD operations that act on two orthogonal directions $\hat{\mathbf{x}}$ and $\hat{\mathbf{y}}$.

$$E_{\mathrm{M2}}(\mathbf{r}_T,t) = E_{\mathrm{G3}}(\mathbf{r}_T,t)e^{i\delta_{\mathrm{M2}}\sin(\omega_{\mathrm{M2}}t)}$$
$$= E_{\mathrm{G3}}(\mathbf{r}_T,t)\sum_{m=-\infty}^{\infty} J_m(\delta_{\mathrm{M2}})e^{im\omega_{\mathrm{M2}}t}, \quad (62)$$

and the replicated-sheared angular spectrum is given by

$$\tilde{E}_{\mathrm{M2}}(\mathbf{k}_T,\omega) = \tilde{E}_{\mathrm{G3}}(\mathbf{k}_T,\omega) * \sum_{m=-\infty}^{\infty} J_m(\delta_{\mathrm{M2}})\delta(\omega - m\omega_{\mathrm{M2}}) . \quad (63)$$

The second grating of the second dimension G4 now acts to disperse the increased bandwidth and removes the preshear from the grating G3. Let the linearized angular dispersion be of equal magnitude to the grating G3 but with opposite sign, i.e., $+\xi_x$, so that the electric field becomes

$$E_{\mathrm{G4}}(\mathbf{r}_T,t) = E_{\mathrm{M2}}(\mathbf{r}_T,t-\xi_x x) \quad (64)$$

and the unsheared angular spectrum is given by

$$\tilde{E}_{\mathrm{G4}}(\mathbf{k}_T,\omega) = \tilde{E}_{\mathrm{M2}}(k_x+\xi_x\omega,k_y,\omega) . \quad (65)$$

After substituting the results of Eqs. (52), (55), (57), and (60),

$$E_{\mathrm{G4}}(\mathbf{r}_T,t) = E_{\mathrm{G3}}(\mathbf{r},t+\xi_x x)e^{i\delta_{\mathrm{M2}}\sin[\omega_{\mathrm{M2}}(t+\xi_x x)]}$$
$$= E_{\mathrm{G2}}(\mathbf{r}_T,t)e^{i\delta_{\mathrm{M2}}\sin[\omega_{\mathrm{M2}}(t+\xi_x x)]}$$
$$= E_0(\mathbf{r}_T,t)e^{i\delta_{\mathrm{M1}}\sin[\omega_{\mathrm{M1}}(t+\xi_y y)]}e^{i\delta_{\mathrm{M2}}\sin[\omega_{\mathrm{M2}}(t+\xi_x x)]}$$
$$= E_0(\mathbf{r}_T,t)\sum_{l=-\infty}^{\infty} J_l(\delta_{\mathrm{M1}})e^{il\omega_{\mathrm{M1}}(t+\xi_y y)}$$
$$\times \sum_{m=-\infty}^{\infty} J_m(\delta_{\mathrm{M2}})e^{im\omega_{\mathrm{M2}}(t+\xi_x x)} . \quad (66)$$

Equation (66) represents a generalization of Ref. 3, which includes beam shape. The angular spectrum of the 2-D SSD operation is then given by the spatiotemporal Fourier-Laplace transform of Eq. (66):

$$\tilde{E}_{\mathrm{G4}}(\mathbf{k}_T,\omega) = \tilde{E}_0(\mathbf{k}_T,\omega)$$
$$* \sum_{l=-\infty}^{\infty} J_l(\delta_{\mathrm{M1}})\delta(k_x, k_y - l\xi_y\omega_{\mathrm{M1}}, \omega + l\omega_{\mathrm{M1}})$$
$$* \sum_{m=-\infty}^{\infty} J_m(\delta_{\mathrm{M2}})\delta(k_x - m\xi_x\omega_{\mathrm{M2}}, k_y, \omega + m\omega_{\mathrm{M2}})$$
$$= \tilde{E}_0(\mathbf{k}_T,\omega) * \sum_{l=-\infty}^{\infty}\sum_{m=-\infty}^{\infty}\left[J_l(\delta_{\mathrm{M1}})J_m(\delta_{\mathrm{M2}})\right.$$
$$\left.\times\delta(k_x - m\xi_x\omega_{\mathrm{M2}}, k_y - l\xi_y\omega_{\mathrm{M1}}, \omega + l\omega_{\mathrm{M1}} + m\omega_{\mathrm{M2}})\right], \quad (67)$$

where it is important to notice that exact replicas of the original spectrum, modified only by the amplitudes of the Bessel functions of the first kind $J_l(\delta_{\mathrm{M1}})$ and $J_m(\delta_{\mathrm{M2}})$, are centered on a regularly spaced grid or field of delta functions formed by the innermost convolution operation. The field of delta functions lies on the plane $k_x/\xi_x + k_y/\xi_y = \omega$ in the 3-D spatiotemporal spectrum and are spaced by $\xi_y\omega_{\mathrm{M1}}$ in the direction of the k_y axis, by $\xi_x\omega_{\mathrm{M2}}$ in the direction of the k_x axis, and by linear combinations of both ω_{M1} and ω_{M2} in the direction of the ω axis. Notice that there exist sum and difference frequencies, which is characteristic of two-tone phase modulation (see Ref. 14, pp. 233–234). An example of a two-tone phase-modulated temporal spectrum is illustrated in Fig. 78.8(b) for the parameters $\delta_{\mathrm{M1}} = 6.15$, $\nu_{\mathrm{M1}} = 3.3$ GHz, $\delta_{\mathrm{M2}} = 13.5$, and $\nu_{\mathrm{M2}} = 3.0$ GHz.

Spatiotemporal cross sections of a 2-D SSD pulsed laser beam with the instantaneous wavelength overlay is shown in Fig. 78.13 for two orthogonal directions for the system parameters $\delta_{\mathrm{M1}} = 6.15$, $\nu_{\mathrm{M1}} = 3.3$ GHz, $\Delta\lambda_{\mathrm{M1}} = 1.5$ Å, $\delta_{\mathrm{M2}} = 13.5$, and $\nu_{\mathrm{M2}} = 3.0$ GHz, $\Delta\lambda_{\mathrm{M2}} = 3.0$ Å, $\tau = 1$ ns, $D_y = D_x = 44$ mm, and where hyperbolic-tangent profiles were used in the spatial and temporal dimensions. At any particular moment in time, the resultant dispersed spectrum from the first dimension of the 2-D SSD operation is seen displayed across the beam as a smaller window of color (relative to the overall bandwidth). As time progresses, the window of color is swept across the total bandwidth. The number of color cycles of the second SSD dimension is given by

$$N_{c_x} \equiv \tau_{D_x}\nu_{M2} , \quad (68)$$

where $\tau_{D_x} = \xi_x D_x$. The brick of light can also be sliced in another direction, i.e., a spatial cross section at a particular instant of time that illustrates how the instantaneous colors move across the beam profile as time changes. Two examples of the 3-D intensity profile of the beam, as viewed from above, are illustrated in Fig. 78.14 with an instantaneous wavelength overlay. The color center is seen to move across the beam. The number of color cycles in each direction is readily observed.

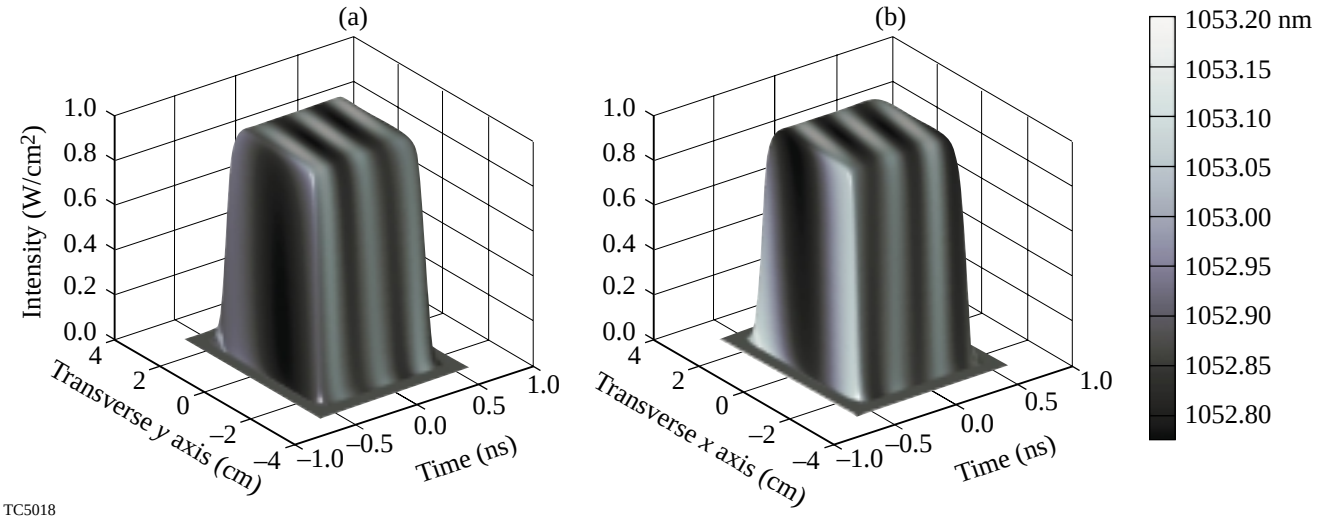

Figure 78.13
Spatiotemporal slices along (a) the *y*-*t* plane and (b) the *x*-*t* plane of a 2-D SSD pulsed beam. with an overlay of the instantaneous wavelength $\hat{\lambda}(\mathbf{r}_T, t)$ superimposed onto the intensity profile for the system parameters: $\delta_{M1} = 6.15$, $\nu_{M1} = 3.3$ GHz, $\Delta\lambda_{M1} = 1.5$ Å, $N_{c_y} \cong 1$, $\delta_{M2} = 13.5$, and $\nu_{M2} = 3.0$ GHz, $\Delta\lambda_{M2} = 3.0$ Å, $N_{c_x} \cong 0.9$, $\tau = 1$ ns, $D_y = D_x = 44$ mm, and where hyperbolic-tangent profiles were used in the spatial and temporal dimensions.

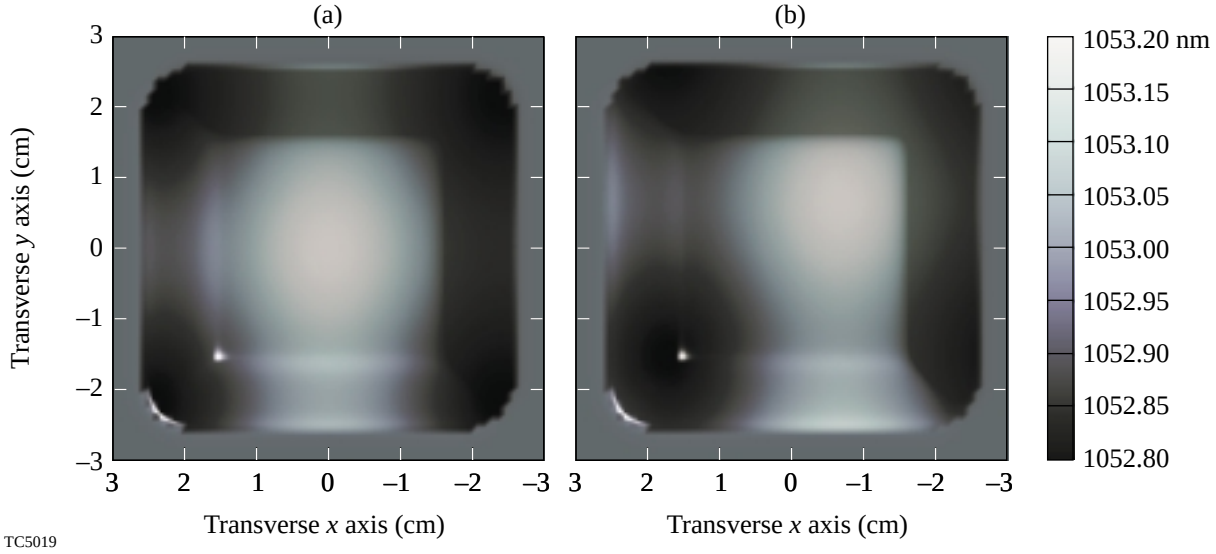

Figure 78.14
Spatial cross sections of a 2-D SSD pulsed beam with an overlay of the instantaneous wavelength $\hat{\lambda}(\mathbf{r}_T, t)$ for the system parameters: $\delta_{M1} = 6.15$, $\nu_{M1} = 3.3$ GHz, $\Delta\lambda_{M1} = 1.5$ Å, $N_{c_y} \cong 1$, $\delta_{M2} = 13.5$, and $\nu_{M2} = 3.0$ GHz, $\Delta\lambda_{M2} = 3.0$ Å, $N_{c_x} \cong 0.9$, $\tau = 1$ ns, $D_y = D_x = 44$ mm, and where hyperbolic-tangent profiles were used in the spatial and temporal dimensions. The images are for two instants of time: (a) $t_1 = 0$ ps and (b) $t_2 = 46$ ps.

A useful diagnostic for 2-D SSD systems is the time-averaged, far-field intensity structure of the pulsed beam. A far-field camera operates by propagating the 2-D SSD pulsed beam through a lens onto its focal plane, where a CCD or film captures the image in a time-integrated sense. This process takes advantage of the Fourier-transforming properties of lenses. The object is assumed to be one focal length in front of the lens (otherwise a phase curvature is imposed across the far field), and the image is in the focal plane of the lens (see Ref. 16, pp. 86–87). Waasese simulates this data by taking the time average of the expression

$$\tilde{I}_{\text{far field}}\left(\mathbf{k}_T, t\right) \equiv \frac{1}{2} n \varepsilon_0 c \left| \int\int_{-\infty}^{\infty} E_0\left(\mathbf{r}_T, t\right) e^{-i\mathbf{k}_T \cdot \mathbf{r}_T} \, \mathrm{d}x\mathrm{d}y \right|^2 . \qquad (69)$$

The expression given by Eq. (64) is equivalent to the far field in real space, at the focal plane of the lens, by making the transformations $k_x \equiv 2\pi x_{\text{ff}}/\lambda_c f$ and $k_y \equiv 2\pi y_{\text{ff}}/\lambda_c f$, where x_{ff} and y_{ff} are the real-space, far-field coordinates and f is the focal length of the lens. A time-averaged plot of Eq. (69) is illustrated in Fig. 78.15 for the same system parameters of this section. If the expression Eq. (64) is plotted directly as a function of time, a movie of the far field can be generated. The underlying far-field pattern remains constant while the spectral peaks change amplitude and can give the appearance of movement when the number of color cycles is less than 1 (provided there are no other smoothing mechanisms).

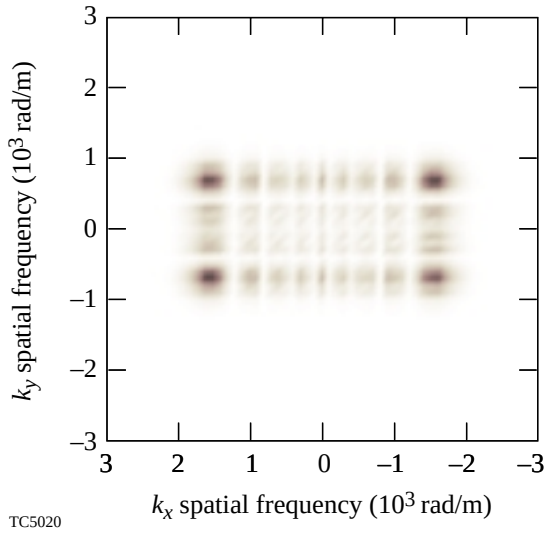

Figure 78.15
Simulation of the time-averaged far field of a 2-D SSD pulsed beam for the system parameters: $\delta_{\text{M1}} = 6.15$, $\nu_{\text{M1}} = 3.3$ GHz, $\Delta\lambda_{\text{M1}} = 1.5$ Å, $N_{c_y} \cong 1$, $\delta_{\text{M2}} = 13.5$, and $\nu_{\text{M2}} = 3.0$ GHz, $\Delta\lambda_{\text{M2}} = 3.0$ Å, $N_{c_x} \cong 0.9$, $\tau = 1$ ns, $D_y = D_x = 44$ mm, and where hyperbolic-tangent profiles were used in the spatial and temporal dimensions.

Nonideal Effects

In realistic SSD driver lines, a variety of mechanisms complicate the ideal situation described in the previous section. Some mechanisms simply distort the pulsed beam and others lead to AM. For example, if the preshear and dispersion grating are misaligned, the dispersion grating will not completely remove the distortion placed on the beam by the preshear grating. The result is a slight increase to the rise time of the pulse as well as a distorted far-field pattern in the rough shape of a rhombus. If the EO phase modulator has an angular-dependent modulation depth, the bandwidth imposed by the modulator will depend on the incident angle of the incident harmonic plane waves. This effect in combination with a grating misalignment explains the observed distorted far-field images (see Fig. 78.16); however, these two effects do not induce AM.

1. PM-to-AM Conversion Mechanisms

A variety of mechanisms destroy the ideal situation described in the previous section by producing AM. In general, they are referred to as PM-to-AM conversion mechanisms since any disruption to the spectral components of perfect phase modulation results in amplitude modulation. These mechanisms fall basically into two main categories that refer to the manner in which the spectral components can be altered: phase and amplitude effects. If the relative phases or the amplitudes of the spectral components are altered (with the exception to a linear phase variation), the phasor components will not add properly, resulting in AM. Waasese is well suited to analyze all of these effects in the spatiotemporal domain since it is based on the angular spectrum representation.

PM-to-AM conversion mechanisms further divide into temporal or spatial domain effects. Temporal domain effects directly control the phase or amplitudes by spectral filtering through devices such as etalons and amplifiers with nonconstant bandwidth. The transmissivity of etalons varies as a function of wavelength, which modulates the spectral amplitudes of a PM pulse. A similar and stronger effect is produced when a first-order ghost image co-propagates at a slight angle to the main beam, which has made one round-trip in a cavity. A streak camera measurement of this effect along with a simulation is shown in Fig. 78.17. Spatial domain effects indirectly control the spectral phase or amplitudes since, as a result of the gratings, the temporal spectrum has been coupled with the

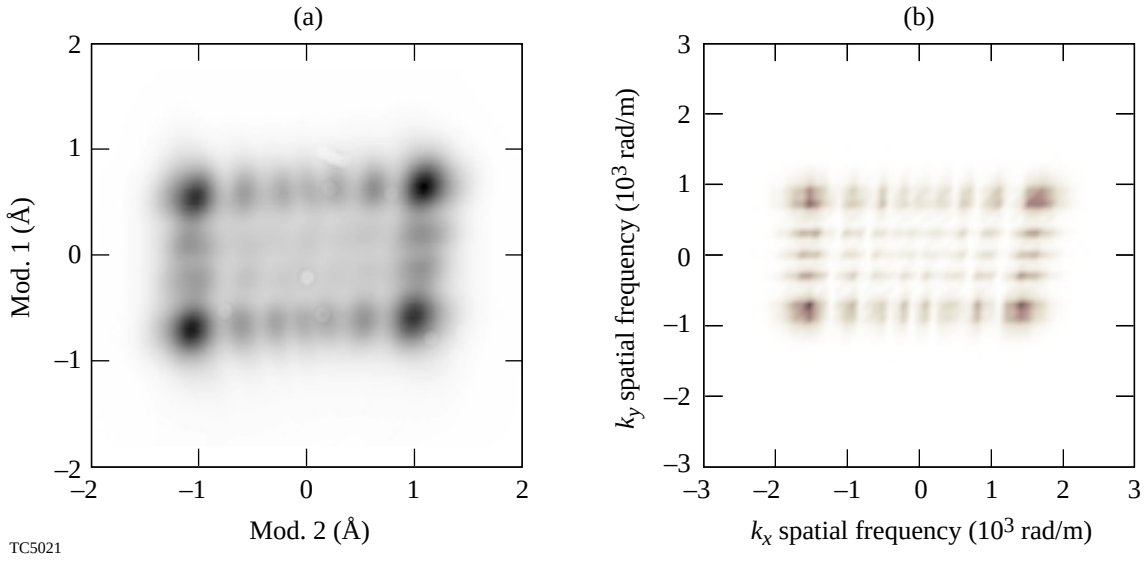

Figure 78.16
(a) A measured distorted far-field image of the double-pass 2-D SSD system and (b) a simulation of the time-averaged far field with an angular-dependent modulation depth and a G3 and G4 misalignment for the system parameters: $\delta_{M1} = 6.15$, $\nu_{M1} = 3.3$ GHz, $\Delta\lambda_{M1} = 1.5$ Å, $N_{c_y} \cong 1$, $\delta_{M2} = 13.5$, and $\nu_{M2} = 3.0$ GHz, $\Delta\lambda_{M2} = 3.0$ Å, $N_{c_x} \cong 0.9$, $\tau = 1$ ns, $D_y = D_x = 44$ mm, and where hyperbolic-tangent profiles were used in the spatial and temporal dimensions.

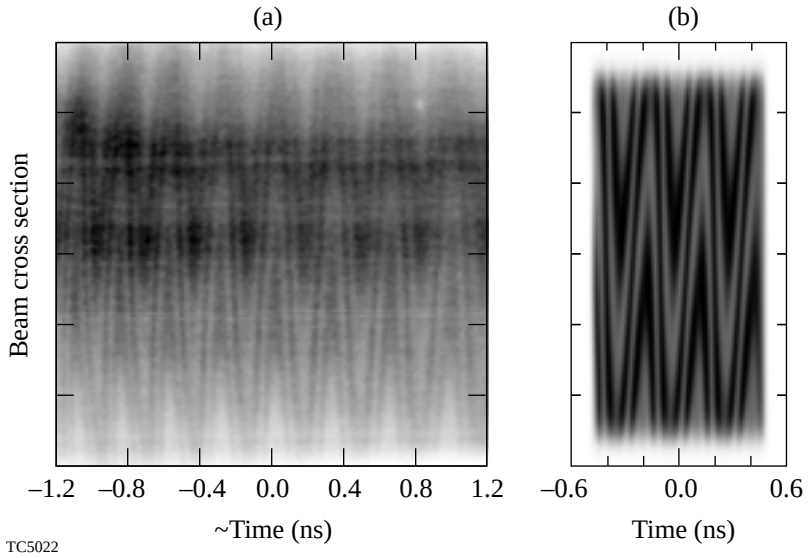

Figure 78.17
(a) A measured streak camera image (showing 2.4 ns of time) resulting from a noncollinear co-propagating reflection and (b) a simulation (showing 1 ns of time) of the interference from a first-order ghost delayed by 50 ps co-propagating at an angle of 40 μrad to the main beam. The simulation is limited to 1 ns due to practical memory constraints; however, 1 ns is sufficient to illustrate the pattern that repeats at a rate of $1/\nu_M$.

spatial spectrum, i.e., the dispersed bandwidth. Therefore, spatial domain effects play a role only after the dispersion gratings G2 of the first dimension and G4 of the second dimension and include propagation and pinhole clipping. Propagation leads to AM since each color's phase front propagates in a different direction, which imparts a different amount of phase to each color. The AM grows unbounded in a nonlinear manner as the propagation distance increases, but image relaying has the ability to restore PM at an image plane. Table 78.III contains some simulation results of propagation out of the image plane for various locations on OMEGA and for different 2-D SSD configurations. Pinhole clipping leads to AM since, in the far field, the dispersed bandwidth is splayed across the focal plane and, if the outermost colors are blocked by the pinhole, AM results.

Spatial phase variations in the near field of an SSD pulsed beam do not directly convert to AM, but the far field may be significantly broadened. If this image is passed through an image relay with a pinhole filter, spectral clipping can occur, which leads to AM. On the other hand, nonlinear spatial phase variations in the far field convert directly to AM in the near field since the spectral components are distributed in the far field as shown in Fig. 78.15. For example, surface roughness of a mirror that is placed in the far field of an image relay cavity alters the phase front of the reflected beam. Waasese simulates the surface roughness by spectrally filtering a random-number generator to match observed surface roughness statistics; an example is shown in Fig. 78.18. The effect on a 1-D SSD pulsed beam is shown in the example in Fig. 78.19. As another example, a curved retro mirror was unknowingly placed in the far-field retro stage of the second dimension and was sheared to produce planar phase fronts. When planar mirrors were substituted for the curved mirror, extremely large AM was observed. The signature of propagation out of an image plane was used to identify the AM source as a curved far-field mirror since propagation also induces a curved phase on the angular spectrum (see Fig. 78.20). Combinations of devices can also lead to AM. For example, a Faraday rotator with a wavelength-sensitive rotation in combination with a cavity ejection wave plate and a polarizer will result in an effective spectral filter.

Nonideal phase-modulator effects can be included in addition to applying the ideal PM described in Eq. (43). If the angular spectrum of the input beam is significantly broad in the direction of the optic axis, i.e., a 1-D SSD beam entering the second-dimension modulator, the crystal birefringence must

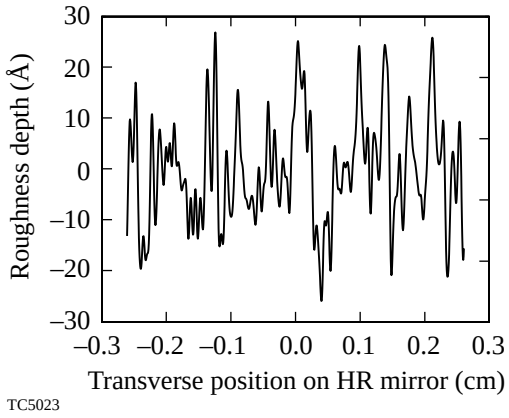

Figure 78.18
Modeled surface roughness on a far-field, high-reflecting dielectric mirror.

Table 78.III: The AM, given as a percentage of peak-to-initial value, that results from propagation out of an image plane for different locations on OMEGA and for different 2-D SSD configurations.

Component Location	Beam Diameter (cm)	1 THz N_c = 2,1 2.1, 10.4 Å 8.8, 10.2 GHz	N_c = 1,3.6 1.5, 3.0 Å 3.3, 12 GHz	N_c = 1, 1 LLNL 5.0 Å 17 GHz	N_c = 2, 1 LLNL 5.0 Å 17 GHz	Current N_c = 1, 1 1.25, 1.75 Å 3.3, 3.0 GHz
Focus lens (3ω)	27.3	13.6	31.3	2.08	8.90	5.83
FCC	27.3	0.731	1.45	0.120	0.482	0.328
F spatial filter	19.5	3.06	6.23	0.496	2.01	1.36
E spatial filter	14.6	3.88	7.98	0.626	2.55	1.72
C relay	8.49	18.9	46.1	2.81	12.3	7.91

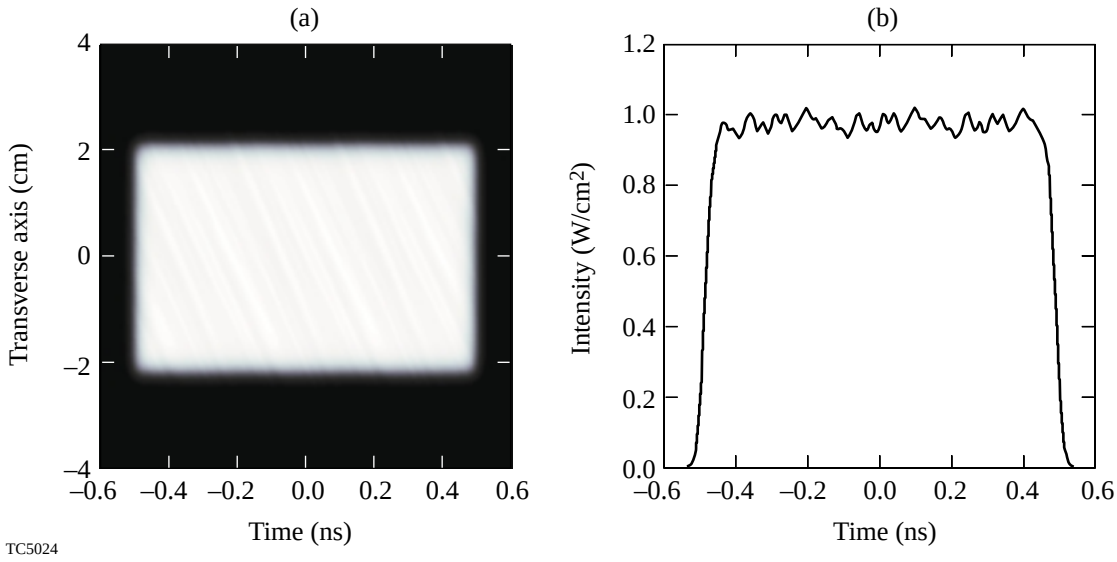

Figure 78.19
(a) Spatiotemporal cross section and (b) lineout of a 1-D SSD pulsed beam incident on a far-field mirror with surface roughness as modeled in Fig. 78.18 that yielded a peak-to-mean AM of 4.8%.

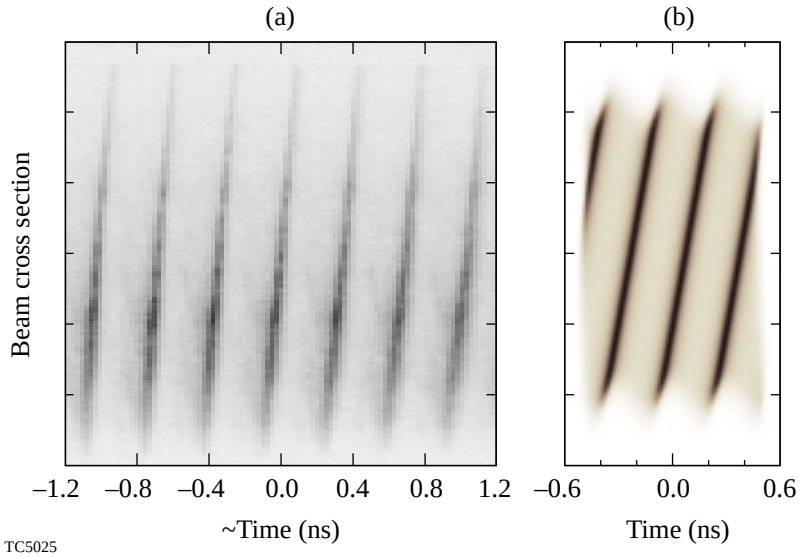

Figure 78.20
(a) A measured streak camera image (showing 3 ns of time) resulting from a phase curvature caused by an improperly placed retro mirror at the second SSD dimension double-pass cavity and (b) a simulation of the same effect, resulting in 110% peak-to-mean AM. The simulation is limited to 1 ns due to practical memory constraints; however, 1 ns is sufficient to illustrate the pattern that repeats at a rate of $1/\nu_M$.

be taken into account. This effect is exhibited by a quadratic phase distortion in the spatial frequency domain (in the direction corresponding to the optic axis) that results from the index ellipsoid of uniaxial crystals (see Ref. 17, pp. 86–90). Each harmonic plane wave produced by the first SSD dimension will experience a different phase delay as it propagates through the second modulator, which results in AM in the first dimension. Before the second dimension has been dispersed by G4, an adjustment of the image plane will correct for this AM source because propagation induces a compensating phase curvature on the angular spectrum (see Fig. 78.21). This is permissible because the spread of the angular spectrum in the second dimension is not significant before it has passed through the dispersion grating.

One other source of PM to AM is the nonlinear mapping of the grating. In the ideal case, Eq. (34) is used to describe this mapping. If the more complete nonlinear mapping is used [Eq. (17)], large enough bandwidths and color cycles will lead to a distorted mapping onto the spatial spectrum and subsequently will introduce AM. Waasese simulates this effect and shows that the distortion is greatest near the edge of the beam as seen in Fig. 78.22.

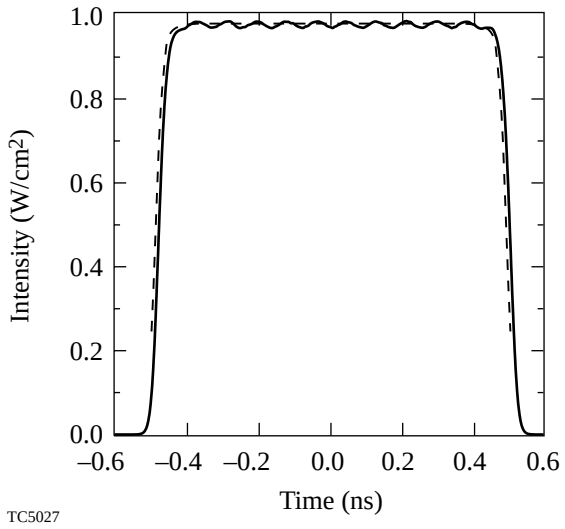

Figure 78.22
Simulation of the nonlinear grating equation effect on a 2-D SSD pulsed beam using a double-grating set. The distortion is greatest near the edge of the beam and results in a peak-to-mean AM of about 1%. The lineout is taken at $x = 1.5$ cm and $y = 0$ cm. The system parameters: $\delta_{M1} = 6.15$, $\nu_{M1} = 3.36$ GHz, $\Delta\lambda_{M1} = 1.5$ Å, $N_{c_y} \cong 1$, $\delta_{M2} = 3.38$, $\nu_{M2} = 12.06$ GHz, $\Delta\lambda_{M2} = 3.0$ Å, and $N_{c_x} \cong 3.65$.

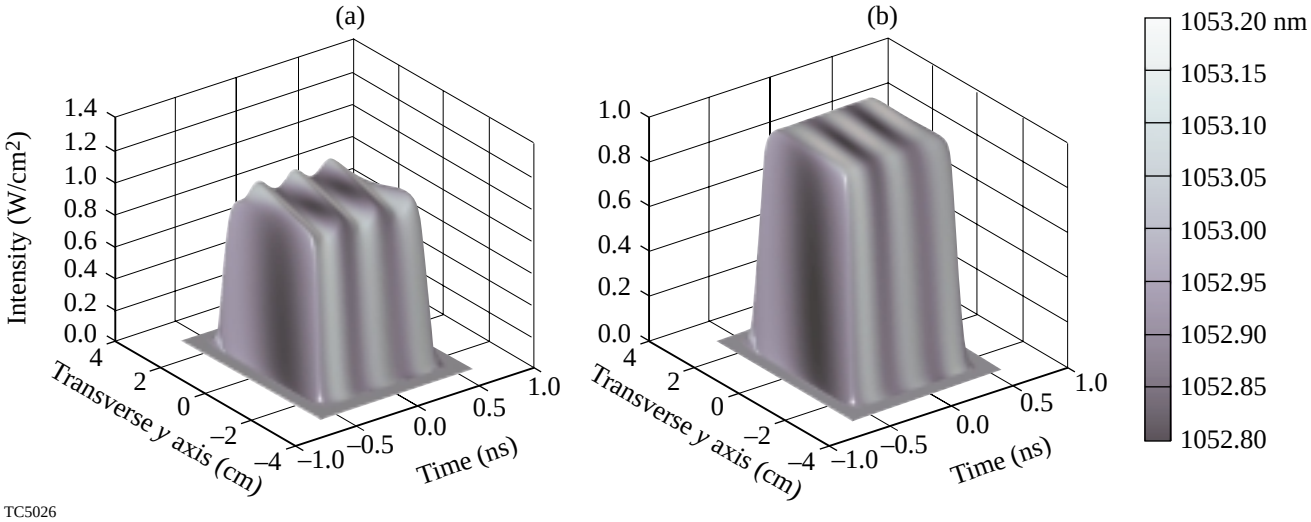

Figure 78.21
(a) Simulation of the propagation of a 1.1-mm beam through the second SSD dimension modulator while including crystal birefringence results in a peak-to-mean AM of 4%; (b) simulation of the compensating effect of a 0.56-mm adjustment to the image plane prior to the final grating at the 1.1-mm beam diameter. The system parameters: $\delta_{M1} = 6.15$, $\nu_{M1} = 3.3$ GHz, $\Delta\lambda_{M1} = 1.5$ Å, $N_{c_y} \cong 1$, $\delta_{M2} = 13.5$, and $\nu_{M2} = 3.0$ GHz, $\Delta\lambda_{M2} = 3.0$ Å, $N_{c_x} \cong 0.9$, $\tau = 1$ ns, $D_y = D_x = 44$ mm, where hyperbolic-tangent profiles were used in the spatial and temporal dimensions, and an effective $LiNbO_3$ crystal length of 36 mm.

Conclusion

Waasese provides a flexible modeling tool for simulating the generation and propagation of 2-D SSD pulsed laser beams. Waasese simulates ideal and nonideal behavior of the many optical components that comprise the SSD driver line including their relative positions. Waasese predicts measurable signatures that function as diagnostic tools since they are associated with particular optical components. The signature/component relationships act together with experimental measurements to help locate and eliminate a troublesome component. Minimizing any AM in the driver line will ensure the safety level and lifetime of OMEGA optics by circumventing the effects of small-scale self-focusing. Waasese proves to be an indispensable modeling tool for the OMEGA laser, and its inherent flexibility will provide a means to enhance its capabilities to model other laser propagation issues such as nonlinear propagation, on-target uniformity, amplifier gain, scattering losses, and pinhole clipping.

ACKNOWLEDGMENT

The authors wish to thank Dr. Jonathan Zuegel and Dr. Douglas Jacobs-Perkins for many useful discussions and laboratory work that followed. This research was supported by NSF Grant PHY94-15583. In addition, this work was partially supported by the U.S. Department of Energy Office of Inertial Confinement Fusion under Cooperative Agreement No. DE-FC03-92SF19460, the University of Rochester, and the New York State Energy Research and Development Authority. The support of DOE does not constitute an endorsement by DOE of the views expressed in this article.

REFERENCES

1. S. Skupsky, R. W. Short, T. Kessler, R. S. Craxton, S. Letzring, and J. M. Soures, J. Appl. Phys. **66**, 3456 (1989).
2. S. Skupsky and R. S. Craxton, "Irradiation Uniformity for High-Compression Laser Fusion Experiments," to be published in Physics of Plasmas.
3. Laboratory for Laser Energetics LLE Review **69**, 1, NTIS document No. DOE/SF/19460-152 (1996). Copies may be obtained from the National Technical Information Service, Springfield, VA 22161.
4. J. E. Rothenberg, J. Opt. Soc. Am. B **14**, 1664 (1997).
5. P. W. McKenty, S. Skupsky, J. H. Kelly, and C. T. Cotton, J. Appl. Phys. **76**, 2027 (1994).
6. Y. H. Chuang, L. Zheng, and D. D. Meyerhofer, "Amplification of Broad-Band Phase-Modulated Laser Pulses for Beam Smoothing by Spectral Dispersion," LLE, memorandum (August 1991).
7. R. Short, LLE, private communication (1989).
8. J. E. Rothenberg, D. F. Browning, and R. B. Wilcox, "The Issue of FM to AM Conversion on the National Ignition Facility," to be published in SPIE's Proceedings on Solid State Lasers for Application (SSLA) to Inertial Confinement Fusion, 3rd Annual International Conference, Monterey, CA, 7–12 June 1998.
9. J. A. Marozas, "Angular Spectrum Representation of Ultrawideband Electromagnetic Pulse Propagation in Lossy, Dispersive Dielectric Slab Waveguides," Ph.D. Thesis, University of Vermont, 1998.
10. K. E. Oughstun and G. C. Sherman, *Electromagnetic Pulse Propagation in Causal Dielectrics*, Springer Series on Wave Phenomena, Vol. 16 (Springer-Verlag, Berlin, 1994).
11. A. E. Siegman, *Lasers* (University Science Books, Mill Valley, CA, 1986).
12. E. G. Loewen and E. Popov, *Diffraction Gratings and Applications*, Optical Engineering, Vol. 58 (Marcel Dekker, New York, 1997).
13. Laboratory for Laser Energetics LLE Review **68**, 192, NTIS document No. DOE/SF/19460-139 (1996). Copies may be obtained from the National Technical Information Service, Springfield, VA 22161.
14. A. B. Carlson, *Communication Systems: An Introduction to Signals and Noise in Electrical Communication*, McGraw-Hill Electrical and Electronic Engineering Series (McGraw-Hill, New York, 1968).
15. M. Abramowitz and I. A. Stegun, eds. *Handbook of Mathematical Functions with Formulas, Graphs, and Mathematical Tables*, Applied Mathematics Series 55 (U.S. Government Printing Office, Washington, DC, 1964).
16. J. W. Goodman, *Introduction to Fourier Optics* (McGraw-Hill, New York, 1968).
17. A. Yariv, in *Quantum Electronics*, 2nd ed. (Wiley, New York, 1975).

Hollow-Shell Implosion Studies on the 60-Beam, UV OMEGA Laser System

Direct-drive inertial confinement laser fusion is accomplished by uniformly illuminating spherical fuel-bearing targets with high-power laser beams, ablatively driving implosions that result in large increases in density and temperature. Current large laser systems such as the University of Rochester's OMEGA laser, which is capable of both direct- and indirect-drive implosion experiments,[1,2] and the Lawrence Livermore National Laboratory's Nova laser,[3,4] which is designed primarily for indirect-drive implosions, are smaller in size and total output energy than what is believed necessary to obtain ignition and gain. Attaining conditions for ignition to occur (densities of ~200 g/cm^3 and temperatures of ~3 to 4 keV) awaits the completion of the National Ignition Facility[5] (NIF) and other megajoule-class drivers currently being planned. In addition to the high temperatures and densities, ignition requires fuel areal densities (density–radius product) $\gtrsim$0.3 g/cm^2 to stop the 3.5-MeV alpha particles in order to obtain thermonuclear burn propagation.[6,7] To reach these conditions in direct-drive implosions requires controlling the growth of the Rayleigh–Taylor (RT) instability, which is seeded by nonuniformities in the laser illumination. The RT instability can lead to shell breakup and mixing of shell material into the gas-fill or central voided region in the case of evacuated targets. We are currently studying the attainment of near-ignition-scale areal densities on OMEGA and the effects of beam smoothing and pulse shaping thereon, by using surrogate cryogenic targets where the shell acts as the fuel layer. These will be followed by actual cryogenic (DD or DT) targets, when the cryogenic target–handling facility is completed.

Previously reported direct-drive OMEGA experiments have demonstrated the ability to achieve high relative temperatures[8] (kT_e ~3 to 4 keV, kT_i ~14 keV) attaining DT neutron yields of >10^{14}. Additionally, the acceleration- and deceleration-phase target stability has been studied in spherical implosions using thin polymer layers containing various high-Z elements, such as Ti, Cl, and Si, with D_2 fills containing a small Ar component.[9]

In the present experiments, we have studied the stagnation phase (maximum density and temperature conditions) of the implosions designed to attain high areal densities ($\gtrsim$0.1 g/cm^3) using both x-ray and neutron spectroscopic techniques. The targets consist of both deuterated and undeuterated polymer shells with either zero-pressure (evacuated) or low-pressure (3-atm) D_2 or D^{3}He fills. The zero-pressure- or low-pressure-fill targets are "surrogates" for cryogenic targets since in actual cryogenic targets the gas pressure will be at or below the triple-point vapor pressure of D_2 or DT gas (0.2 atm at 20 K).[10] An equivalent particle density is obtained for a pressure of 3 atm at room temperature (300 K). The hydrodynamics of the central gas-filled region of a 3-atm-filled target will therefore be the same as an actual cryogenic target at the triple point. Conversely, the shell of the surrogate cryogenic target is not expected to evolve the same but will have a different in-flight aspect ratio (mean radius/thickness) and convergence ratio (initial radius/final radius). Also, the RT growth in a CH shell will be larger than for a DT shell because the reduced ablation velocity leads to a lesser ablative stabilization. Nevertheless, high areal densities ($\gtrsim$0.1 g/cm^2), high convergence ratios (>20), and moderately high central temperatures ($\gtrsim$2 keV) can be studied with a surrogate cryogenic target. The measurements described in this work have revealed significant information about the implosion of surrogate cryogenic targets and the effects of beam smoothing and pulse shaping thereon.

Experiments

The targets used for these experiments were manufactured by General Atomics.[11] Hollow spherical shells were produced by coating layers of deuterated plastic (CD) and then undeuterated plastic (CH) over a depolymerizable spherical mandrel. The coatings were accomplished by the method of glow discharge plasma (GDP) polymerization. The CD-layer thicknesses ranged from 5 to 10 μm, while the CH-layer thicknesses ranged from 10 to 30 μm. Layer thicknesses were measured to an accuracy of 0.5 μm, and the target diameter was measured to an accuracy of 1 μm. In each case the targets were

held in place in the target chamber using low-mass stalks consisting of a short length of spider silk (~100 μm) that had been previously overcoated with parylene to add mechanical stability. The spider silks were glued to boron fibers ~20 μm in diameter, and the parylene-overcoated stalk end was attached to the target with UV-curable epoxy. The UV epoxy glue spots were the largest single mass perturbation introduced by the stalks; these spots ranged from 10 to 30 μm in diameter. Targets were either prepared and kept evacuated (<10^{-3} Torr) or filled with 3 atm of D_2, H_2, or an equal molar mixture of D^3He gases.

Three laser-irradiation conditions were used for these experiments: (1) Coherent beam illumination (no beam smoothing) was used with the beams focused so as to nearly tangentially illuminate the target at the beam edge. (2) Each beam was modified using a distributed phase plate (DPP)[12] at best focus (diffraction minimum spot ~0.95 mm). (3) Beams with DPP's were smoothed using SSD[13] along two axes (2-D SSD)[12] with frequencies of 3.5 and 3.0 GHz and bandwidths of 1.7 and 1.2 Å (0.25-THz bandwidth). The estimated illumination uniformity for 60 overlapping OMEGA beams (σ_{rms} for ℓ-modes 1 to 500) was ~15% for the coherent beam illumination, ~20% for DPP-only illumination, and ~2.5% for the DPP+SSD illumination. All values quoted are calculated from the idealized effect on the beam distribution and averaged over the length of the pulse. While the distributed phase plates produce a smooth envelope to the beam, they also introduce small-scale laser speckle, hence the larger value of σ_{rms} for the DPP-only illumination. Although the value of σ_{rms} for the DPP+SSD illumination is lower than the other cases, two additional effects not accounted for by this time-averaged quantity must be considered: (1) Beam balance at current levels (~7% rms beam-to-beam energy variation) would produce an on-target illumination nonuniformity of ~2.5% rms even with perfectly smooth beams, with most of that contribution in modes 1 through 5. (2) The smoothing time of the present level of SSD may not be fast enough to avoid imprinting laser-beam speckle onto the target.

The three pulse shapes used in these experiments (Fig. 78.23) were the 1-ns square pulse shape, the 1:6 ratio foot-to-main-pulse shape (also known as PS26), and the 1:40 ratio pulse shape known as $\alpha = 3$. Examples of the actual pulse shapes are shown along with the design shape. Good pulse-shape repeatability was obtained. The purpose of varying the pulse shape in these experiments is to investigate target performance versus pulse shape. Ideally a gradually rising intensity, if properly designed, will produce a final target compression greater than a sharply rising pulse. Figures 78.24(a) and 78.24(b) show the calculated primary neutron yield (D-D) and the fuel and shell areal densities as a function of time for the three different pulse shapes. All simulations (accomplished with the hydrodynamics code *LILAC* as described in the next section) are for an assumed total energy on target of 25 kJ, and in each case the target was a 0.95-mm-diam, 20-μm-thick CH shell filled with 3 atm of D^3He. For these conditions it is clear that the highest yield and compression are obtained for the highest-contrast pulse shape. This trend also holds for the evacuated targets.

The two instruments used to obtain x-ray spectra of the implosion cores were a Kirkpatrick-Baez–type (KB) microscope outfitted with a diffraction grating[14] and a crystal spectrometer outfitted with an imaging slit.[15] The KB microscope has Ir-coated mirrors and a sensitive energy band from ~2 to

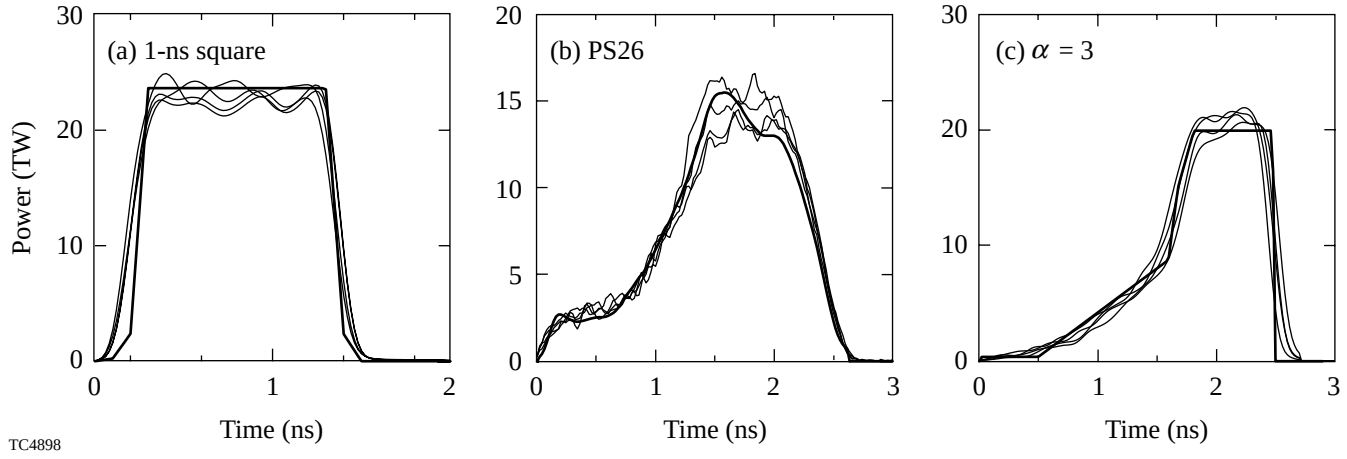

Figure 78.23
The three pulse shapes used in these experiments: (a) the 1-ns square pulse, (b) PS26, a 1:6 ratio foot-to-main pulse shape, and (c) $\alpha = 3$, a 1:40 ratio pulse shape.

8 keV. The absolute response of the microscope was determined both in the laboratory and *in situ*. Figure 78.25(a) shows a typical grating-dispersed image of an imploded hollow-shell target. The bright central peak is the overexposed image of the core (zeroth-order image), while the indicated lines are diffracted images of the core (±first-order images). The spectrum of the core emission, after correction for instrument response, is shown in Fig. 78.25(b) along with a model fit to the spectrum (thermal bremsstrahlung with absorption). (The details of this analysis will be described in the next section.) The crystal spectrometer consisted of an imaging slit in front of a diffraction crystal viewing the target. Diffracted x rays were recorded with DEF film as were the spectrally dispersed images from the KB microscope. The emission from the implosion core was separated from the total flux by the narrow size of the imaging slit (~100 μm). The spectrometer was set to view a region of the spectrum from ~4 to 6 keV containing continuum emission from the targets. This was compared to the KB microscope–derived spectra on certain shots. A limited number of shots were taken with targets containing a Ti-doped layer, and in such cases the observed jump in the spectrum at the Ti *K* edge was used to infer the shell areal density.[15]

Primary neutron yield (D-D neutrons) was measured with an array of cross-calibrated scintillator detectors. Secondary neutron yield was measured with an 824 detector array of

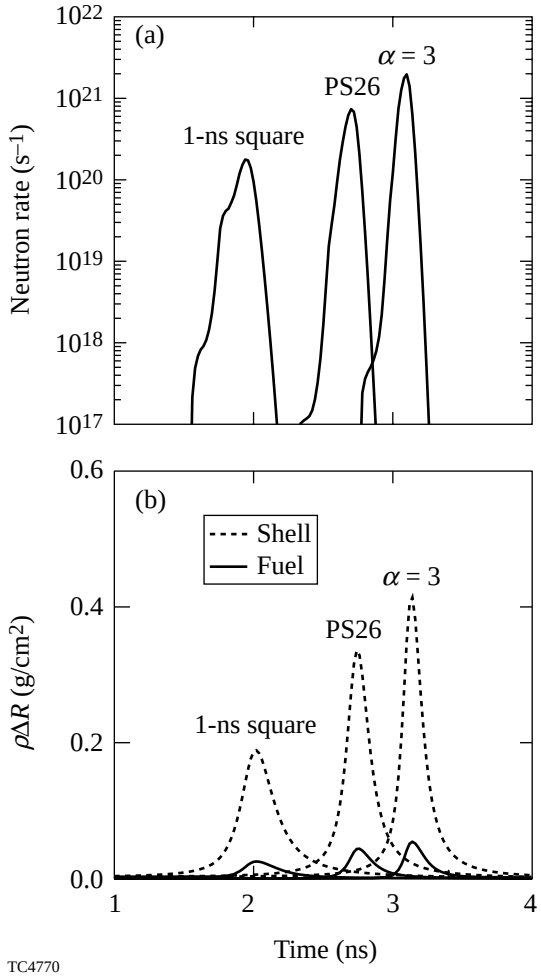

Figure 78.24
Simulations of the (a) D-D neutron-generation rate and (b) the fuel and shell areal densities as functions of time for the three pulse shapes. The targets were all assumed to be 20-μm-thick CH shells, filled with 3 atm of D^3He, imploded by a total energy of 25 kJ.

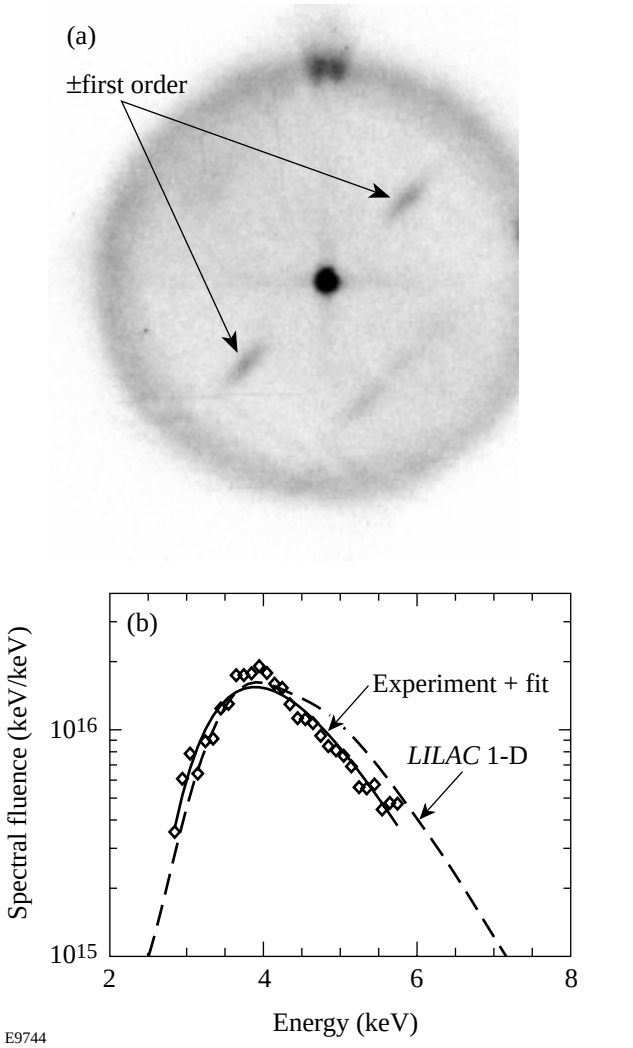

Figure 78.25
Grating-dispersed KB microscope image of OMEGA shot 9130 (see Table 78.IV): (a) the zeroth-order image with ±first-order diffracted images of the core (indicated), and (b) the core spectrum after correction for instrument response, along with 1-D (*LILAC*) simulations of the same.

scintillators, each of which records the neutron arrival time to an accuracy of ~0.5 ns, which translates into an accuracy in energy of ~0.5 MeV. This instrument, called MEDUSA (Multi-Element Detector Using a Scintillator Array),[16] allows for the determination of the much smaller secondary neutron yield (D-T neutrons) due to their earlier arrival time at the detector. Figure 78.26 shows an example spectrum from MEDUSA on a 20-μm-thick CD/CH shell imploded with a 1-ns square pulse and coherent beam illumination. The secondary neutron yield is clearly seen, appearing as the broad peak between 12 and 17 MeV. The integral of this peak is proportional to the secondary yield.

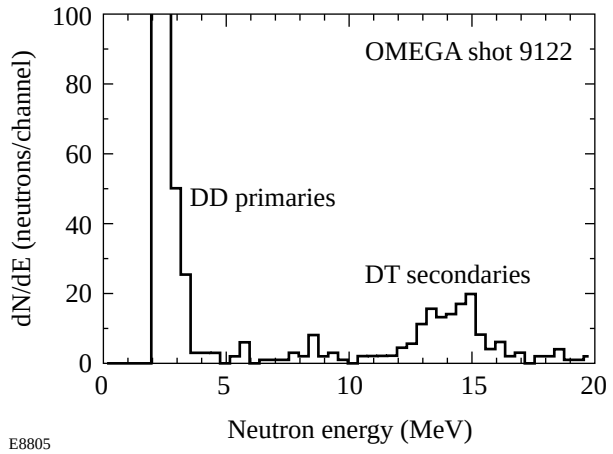

Figure 78.26
Example of the neutron spectrum emitted by a CD target as determined by MEDUSA. The neutrons with energies from 12 to 17 MeV are from DT fusion reactions generated by primary-fusion-product (secondary) tritons fusing with primary deuterons.

Results

Several combinations of shell thicknesses (CD/CH and CH only), fill gases, and pulse shapes were investigated. We present here a representative set from which x-ray and neutron spectral information was obtained. Table 78.IV is a sample of the target shot conditions and experimentally measured values. The conditions for each shot, illumination type, energy, D-D yield, D-T yield (where measured), kT_e, and ρR, along with *LILAC* predictions of these quantities, are grouped by type of pulse shape. The implosions were simulated with the one-dimensional hydrocode *LILAC*, which uses tabulated equation of state (SESAME),[17] flux-limited electron transport, and multi-group radiation transport using local thermodynamic equilibrium (LTE) opacities,[18] and inverse-bremsstrahlung-absorption energy deposition through a ray-tracing algorithm in the underdense plasma. A flux limiter of $f = 0.06$ with a sharp cutoff was used. The primary fusion reaction products were transported using a multi-angle straight-line method, which also includes the production of neutrons from the secondary D-T reactions. The detailed space-resolved x-ray spectra generated for comparison with the observations were calculated with a postprocessor.

As shown in previous works,[14,19] the x-ray spectrum emitted by an undoped polymer shell can, to a good approximation, be represented by

$$I_x = I_{\text{hot}}\, e^{-E/kT_{\text{hot}}}\, e^{-\langle \mu(E)\rho R\rangle_{\text{shell}}}, \tag{1}$$

where I_{hot} is the intensity of the thermal bremsstrahlung emission from the core region, which has a characteristic temperature kT_{hot}. Absorption will occur in the shell as x rays exit the core through the surrounding colder shell whose optical depth $\tau = \langle \mu(E)\rho R\rangle$, where $\mu(E)$ is the energy-dependent mass absorption coefficient and ρR is the areal density (the brackets indicate an average over the shell). To a good approximation μ is given by

$$\mu = 1.9\times 10^3 \frac{1}{E^3} g(\rho, kT) \quad \left(\text{cm}^2/\text{g}\right), \tag{2}$$

where E is in keV and $g \le 1$. Using this approximation, a lower limit on ρR_{shell} can be determined by fitting the observed spectrum to I_X with the optical depth given by

$$\tau = 1.9\times 10^3 \frac{\rho R_{\text{cold}}}{E^3}, \tag{3}$$

where ρR_{cold} is the areal density of the cold shell material and, therefore, a lower limit on the total ρR_{shell}. Both ρR_{cold} and the average electron temperature kT_e are determined by fitting Eq. (1) to the observed spectrum.

The combined measurements of the primary neutron yield from the D-D reaction and the secondary neutron yield from the D-T reaction allow us to estimate the areal density of the deuterium-bearing shell material ρR_{CD} using the following:

$$\rho R_{\text{CD}} \ge \left[\frac{Y_{\text{DT}}}{Y_{\text{DD}}} \Big/ 4.3\times 10^{-2}\right] \left(\text{g}/\text{cm}^2\right), \tag{4}$$

where we have used the results of Azechi, Cable, and Stapf[20] scaled to CD (which has a 6:1 ratio of carbon to deuterium

mass) and we have taken the maximum calculated ratio as a function of temperature as the limit given above. Since the range of the primary 1-MeV tritons may be smaller than the total areal density of the CD layer ρR_{CD} and since ρR_{CD} is less than the total ρR_{shell}, this value again places a lower limit on ρR_{shell}.

Figure 78.27 shows the measurements of kT_e and *LILAC* predictions of these values for the voided targets imploded by 1-ns square pulses. (The values obtained from simulations are averaged over the stagnation, as is the case for all comparisons to measurements that follow. The simulated x-ray measurements are weighted by emitted x-ray intensity, whereas the simulated neutron measurements are values averaged over the time of neutron emission.) The measured values of kT_e show little discernible difference for the three illumination conditions. (Note that slightly less energy was used to implode the targets with DPP+SSD illumination.) The thinnest-shell targets have measured kT_e values that are slightly lower than the predicted values.

Figure 78.28 shows the measured values of ρR_{cold} from the x-ray spectra for 1-ns-square-pulse illumination. Here we have included both the voided CD/CH shells and the 3-atm-filled CH shells. The higher measured values of ρR_{cold} for the thicker-shell targets are evident, following the trend of the simulations, which is expected since the implosion cores of thicker targets reach a lower temperature. (Therefore the shell material is less stripped and can more heavily absorb the continuum emission from the core.) The significantly lower values of ρR_{cold} for the DPP-only cases are also noticeable. This difference is largest for the 3-atm-filled CH targets pointing to the gas–shell interface as a source of disruption to the symmetry of the implosion. The differences between DPP+SSD and DPP-only illumination for gas-filled targets are further apparent when one compares their spectra

Table 78.IV: Measured and simulated values for a representative sample of voided CD/CH target experiments. The numbered columns contain the following: (1) pulse type, (2) beam-smoothing condition, (3) shell thickness, (4) energy on target, (5) the measured D-D neutron yield [Y_n (D-D)], (6) error of measurement of Y_n (D-D), (7) the measured D-T neutron yield [Y_n (D-T)], (8) error of measured Y_n (D-T), (9) the CD layer areal density ρR_{CD} determined from Eq. (4), (10) error of ρR_{CD} value, (11) *LILAC*-predicted value of Y_n (D-D), (12) YOC (D-D), the ratio of the measured-to-predicted values of Y_n (D-D), (13) *LILAC*-predicted value of Y_n (D-T), (14) *LILAC*-predicted value of ρR_{CD}, (15) *LILAC*-predicted

	1	2	3	4	5	6	7	8	9	10	11	12
Shot	Pulse Type	Illumination Condition	CD+CH (μm)	Energy (kJ)	Y_n(D-D)	Y_n(D-D) error	Y_n(D-T)	Y_n(D-T) error	ρR_{MED} (mg/cm^2)	ρR_{MED} error (mg/cm^2)	Y_n(D-D) 1-D	YOC (D-D)
7817	1-ns sq	Coherent	31.8	26.2	2.3(8)	6.7(6)					4.9(8)	0.47
9130	1-ns sq	Coherent	39.4	28.4	7.4(7)	2.5(6)					1.1(8)	0.66
9266	1-ns sq	Coherent	25.6	29.2	5.4(8)	7.0(6)					6.1 (9)	0.09
9267	1-ns sq	Coherent	34.4	30.2	1.6(8)	3.7(6)					5.2(8)	0.31
14010	1-ns sq	DPP's only	21.2	28.0	1.4(9)	3.2(7)	4.1(6)	2.6(5)	69.0	4.8	1.7(10)	0.08
14012	1-ns sq	DPP's only	31.0	27.2	2.5(8)	1.4(7)	5.0(5)	8.6(4)	45.4	8.3	5.9(8)	0.43
11561	1-ns sq	DPP's + SSD	19.9	27.3	2.6(9)	2.0(8)	7.3(6)	3.7(5)	64.9	6.1	1.8(10)	0.15
11562	1-ns sq	DPP's + SSD	30.9	28.3	2.5(8)	6.4(7)	4.6(5)	8.3(4)	42.2	13.2	5.7(8)	0.44
11576	1-ns sq	DPP's + SSD	38.9	27.7	1.4(8)	1.6(6)	1.8(5)	5.1(4)	30.1	8.7	6.7(7)	2.03
12538	1-ns sq	DPP's + SSD	21.1	24.0	1.4(9)	5.5(7)	6.0(6)	3.3(5)	102.3	7.0	5.9(9)	0.23
12548	$\alpha = 3$	DPP's + SSD	21.1	20.6	1.7(8)	2.6(6)	7.2(4)	3.2(4)	9.7	4.4	8.6(9)	0.02
12549	$\alpha = 3$	DPP's + SSD	26.9	21.2	1.1(8)	2.0(6)	5.7(4)	2.9(4)	12.5	6.3	1.3(9)	0.08
12551	$\alpha = 3$	DPP's + SSD	30.8	21.0	4.4(7)	1.3(6)	2.8(4)	2.0(4)	15.0	10.6	3.8(8)	0.12
12562	PS26	DPP's + SSD	21.3	19.6	7.8(7)	1.3(7)	1.1(5)	4.1(4)	34.4	13.5	1.0(10)	0.01
12563	PS26	DPP's + SSD	26.9	19.8	6.5(7)	1.2(7)	1.4(5)	4.5(4)	50.9	18.6	3.0(9)	0.02
12567	PS26	DPP's + SSD	30.7	20.0	7.8(7)	1.3(7)	2.9(5)	6.4(4)	85.6	24.0	1.7(9)	0.05

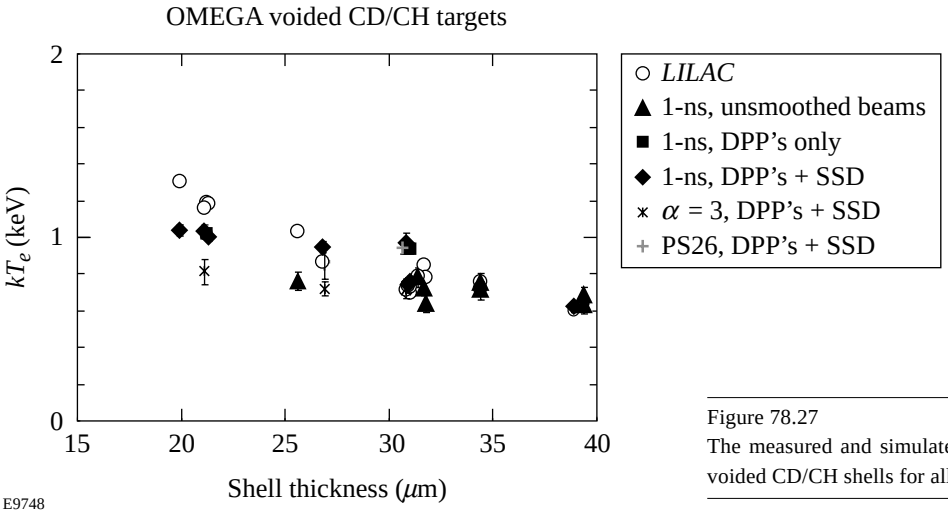

Figure 78.27
The measured and simulated values of kT_e versus shell thickness for the voided CD/CH shells for all pulse shapes.

value of ρR_{shell} averaged over the time of neutron production, (16) *LILAC*-predicted value of the ion temperature (kT_i) averaged over the time of neutron production, (17) the x-ray-spectrum determined electron temperature (kT_e), (18) error of (kT_e), (19) the *LILAC*-predicted value of the kT_e, as would be determined from the x-ray spectrum, (20) the x-ray spectrum determined cold shell density (ρR_{cold}), (21) error of ρR_{cold}, (22) the *LILAC*-predicted value of ρR_{cold}, (23) the inferred shell areal density (ρR_{shell}), and (24) error of experimentally determined value of ρR_{shell}. [*Numbers in ( ) indicate the power of 10; i.e., 2.3(8) = 2.3×10^8].

13	14	15	16	17	18	19	20	21	22	23	24
Y_n(DT) 1-D	ρR_{MED} 1-D (mg/cm^2)	$<\rho R>_n$ 1-D (mg/cm^2)	$<kT_i>_n$ 1-D (keV)	kT_e (KB) (keV)	kT_e error (keV)	kT_e 1-D (keV)	ρR_{cold} (KB) (mg/cm^2)	ρR_{cold} error (mg/cm^2)	ρR_{cold} 1-D (mg/cm^2)	ρR_{shell} (KB) (mg/cm^2)	ρR_{shell} error (mg/cm^2)
1.3(6)		199	0.67	0.64	0.05	0.78	31	6	67	93	18
2.3(5)		170	0.58	0.68	0.05	0.65	61	7	74	140	16
2.6(7)		268	1.03	0.76	0.05	1.03	26	5	76	92	18
1.3(7)		196	0.68	0.71	0.05	0.72	38	6	74	100	16
9.0(7)	127.3	320	1.19	1.02	0.03	1.19	8	1	89	29	4
1.5(6)	58.6	196	0.68	0.94	0.03	0.73	22	1	69	63	3
9.7(7)	128.6	312	1.22	1.04	0.03	1.30	13	1	58	71	5
1.4(6)	59.1	201	0.68	0.74	0.04	0.73	27	3	70	78	9
1.3(5)	43.5	165	0.54	0.62	0.03	0.60	52	7	76	113	15
2.4(7)	96.2	329	1.02	1.03	0.05	1.16	16	3	38	139	22
4.3(7)	117.4	323	1.11	0.81	0.07	1.19	0	3	111	0	
4.0(6)	72.9	254	0.75	0.72	0.04	0.85	16	2	91	45	6
9.3(5)	56.9	224	0.61	0.72	0.05	0.66	22	3	92	54	7
5.4(7)	123.1	346	1.25			1.30			150		
1.2(7)	95.1	338	0.88	0.86	0.09	0.89	29	4	179	54	7
6.6(6)	88.2	368	0.80	0.94	0.03	0.85	42	2	209	74	4

[shown for two different shell thicknesses, 20 and 25 μm, in Figs. 78.29(a) and 78.29(b)]. The low-energy portions of the spectra exhibit a marked difference indicative of lower compression for the DPP-only cases, despite the fact that the high-energy portions of the spectra are nearly identical. This indicates that conditions in the highest-temperature regions of the implosion (i.e., the gas-filled cores and inner edge of the shell) were unaffected by the different conditions obtained in the shell. Additionally, differences between the three pulse shapes are seen in the measured values of ρR_{cold} (Fig. 78.30). The shaped-pulse implosions have lower measured shell areal densities than with a square pulse (see Fig. 78.28), with the highest-contrast-pulse-shape implosions (α = 3) having the lowest values. All DPP-only cases are lower than the comparison DPP+SSD cases.

The measured primary (D-D) neutron yields of the voided CD/CH targets for all pulse shapes are shown in Fig. 78.31(a). The ratios of the measured primary yield to the *LILAC*-calculated yield (normalized yield) are shown in Fig. 78.31(b). The primary yields obtained from implosions with 1-ns-square-pulse illumination follow a fairly well-defined trend with the highest yields obtained for the thinnest shells (highest calculated central temperatures and areal densities). Little difference is seen for the three uniformity conditions, indicative of the insensitivity of the shell/void interface to the illumination conditions employed. Lower absolute yields were obtained for the shaped-pulse implosions [Fig. 78.31(a)]; although, due to current OMEGA laser operation conditions, the maximum on-target energy is less for the shaped pulses (~21 kJ). Nevertheless, lower normalized yields were obtained for the

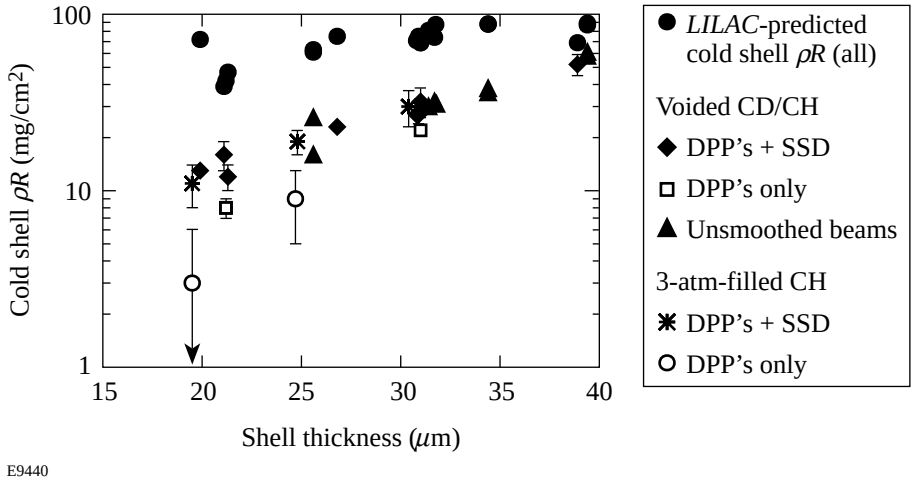

Figure 78.28
The measured values of ρR_{cold} for the voided CD/CH and 3-atm-filled CH targets from shots with 1-ns-square-pulse illumination. Cases of all three laser-beam conditions are shown: unsmoothed beams, DPP only, and DPP+SSD smoothed beams. The values of ρR_{cold} expected from *LILAC* simulations are also shown.

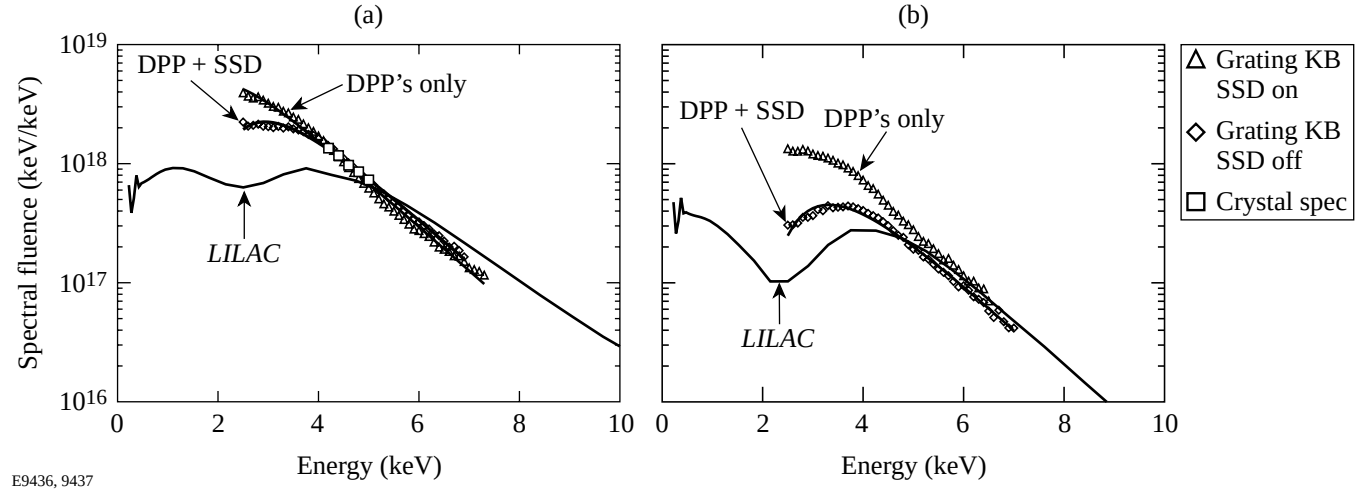

Figure 78.29
The measured and predicted core x-ray spectra from two DPP-only/DPP+SSD pairs of CH targets filled with 3 atm of D^3He and imploded with 1-ns square pulses: (a) a 20-μm-thick pair and (b) a 25-μm-thick pair. Note the agreement between KB-microscope- and crystal-spectrometer-determined spectra in (a).

shaped pulses [Fig. 78.31(b)] with the lowest yield for the PS26 pulse shape.

Figures 78.32(a) and 78.32(b) show the measured primary and secondary neutron yields along with the *LILAC*-simulated yields for the voided CD/CH shells imploded with the 1-ns-pulse shape. Again the trend is to lower yields for thicker shells, with the measured yields for thicker shells closer to the simulated yields, indicating less disruption during implosion for the thicker shells. As discussed previously, a lower limit on ρR_{shell} is determined from the simultaneous measurements of primary (D-D) and secondary (D-T) neutron yield. Figure 78.33 shows the values so obtained for the voided CD/CH shells along with *LILAC* predictions of the measurements. The thinner targets have both higher measured and predicted ρR_{shell} values, opposite to the trend seen in the x-ray measurements, because of the larger range of tritons in the higher-temperature conditions, expected and obtained, for the thinner shells. Quite striking is the trend to lower ρR_{shell} for the thinner shells imploded with shaped pulses, which is lowest for the highest-contrast pulse shape ($\alpha = 3$). This again is indicative of shell disruption for the shaped-pulse implosions (resulting in lower apparent compression at the time of this measurement). The trend is similar to that seen for ρR_{shell} measurements obtained from the x-ray spectra (Fig. 78.29). The observed compression is less for the shaped-pulse implosions from both sets of measurements.

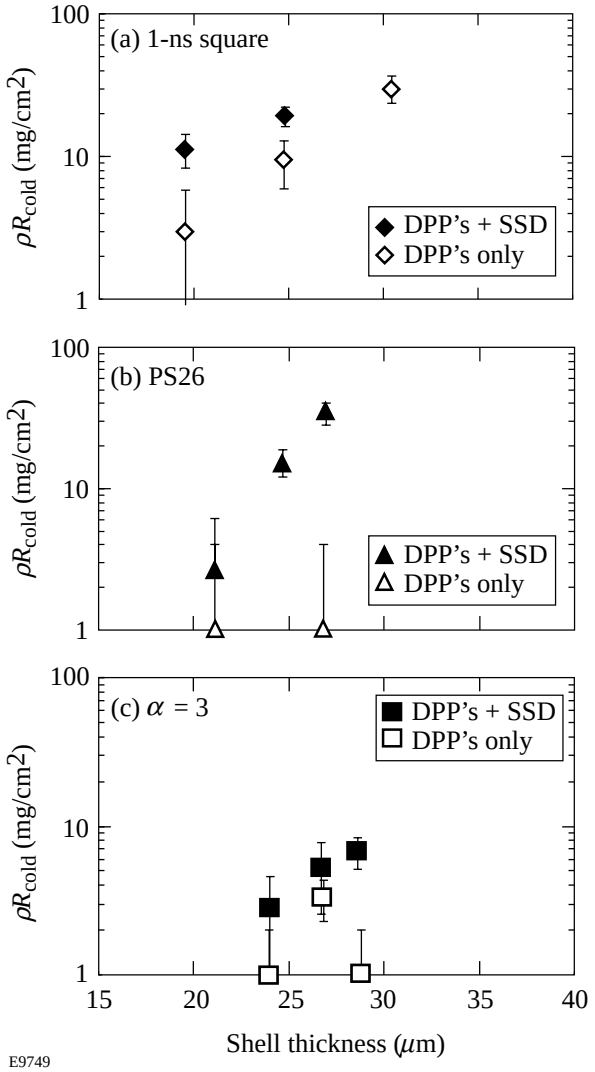

Figure 78.30
The measured values of ρR_{cold} for 3-atm-filled CH targets from shots with (a) 1-ns square, (b) PS26, and (c) $\alpha = 3$ pulse illumination.

The combined measurements of ρR_{shell} from both the x-ray spectra and the primary-to-secondary-yield ratio for the voided targets are shown in Fig. 78.34. The dotted line and arrows indicate the lower limit on ρR_{shell} obtained from the

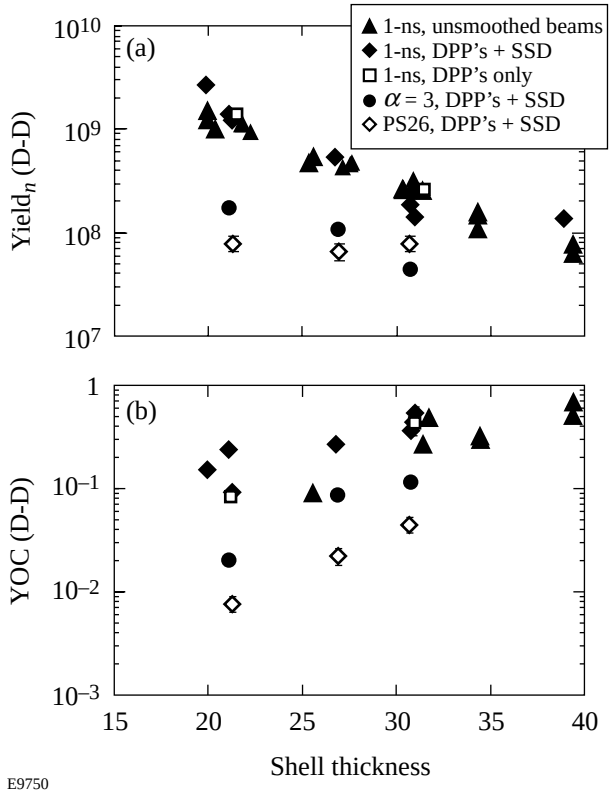

Figure 78.31
Measurements of the primary (D-D) neutron yield from voided CD/CH shells for all three pulse shapes versus shell thickness: (a) the absolute measured yield and (b) the normalized yield (measured/calculated).

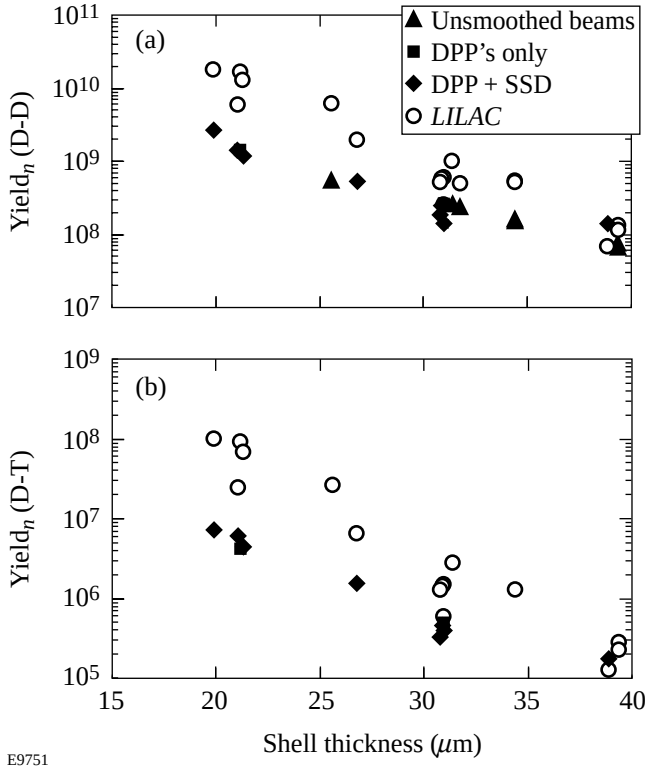

Figure 78.32
Measurements of (a) primary (D-D) and (b) secondary (D-T) neutron yield from voided CD/CH shells imploded with 1-ns square pulses from the three beam-uniformity cases versus shell thickness. *LILAC* predictions of the measurements are also shown.

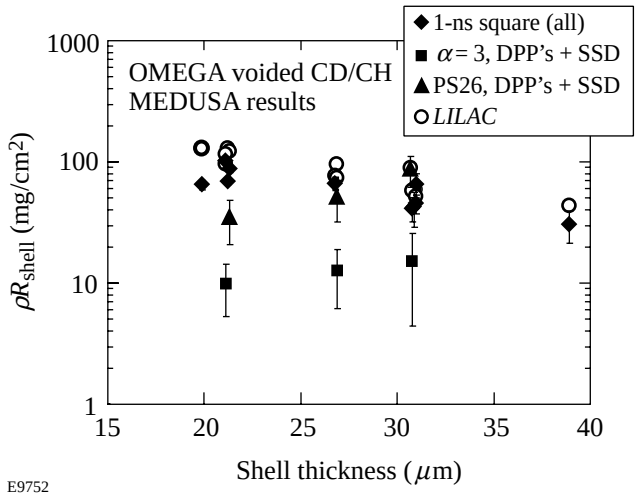

Figure 78.33
The measured lower limits on ρR_{shell} of the voided CD/CH shells from MEDUSA measurements versus shell thickness for the various cases of pulse shape and beam uniformity. The values expected from *LILAC* simulations are shown for comparison.

combined measurements. The estimates of ρR_{shell} obtained from Ti-doped shells as reported by Yaakobi and Marshall[15] are also shown (these values are lower limits as well). Both sets taken together indicate that ρR_{shell} in excess of ~60 mg/cm^2 has been obtained in every case. Assuming that the ionization state of the target is properly predicted by the hydrocode simulations, an estimate of the full ρR_{shell} can be determined by correcting the x-ray measurements of ρR_{cold} by the predicted ionization fraction. Values so determined are shown in Fig. 78.35. The estimated x-ray–averaged ρR_{shell} ranges from ~60 to 130 mg/cm^2.

Conclusions

In conclusion, we have performed experiments on hollow-shell (CD/CH and CH only), evacuated or low-pressure-filled (3-atm) targets with the OMEGA laser system demonstrating compression of the shell material (surrogate-cryogenic fuel) to areal densities of ~60 to 130 mg/cm^2. The survey of various implosion conditions (unsmoothed to smoothed beams; high-intensity, short-pulse shapes to ramped-intensity, longer-pulse shapes) has yielded information about the target performance as a function of illumination (laser drive) relevant to cryogenic-target experiments to follow. Specifically for a 1-ns square pulse and evacuated targets, the primary neutron yield from the core is not greatly affected by the differences in illumination uniformity at current levels; however, both the illumination uniformity and the initial shell thickness affect the final shell areal density. The thicker-shell targets compress to

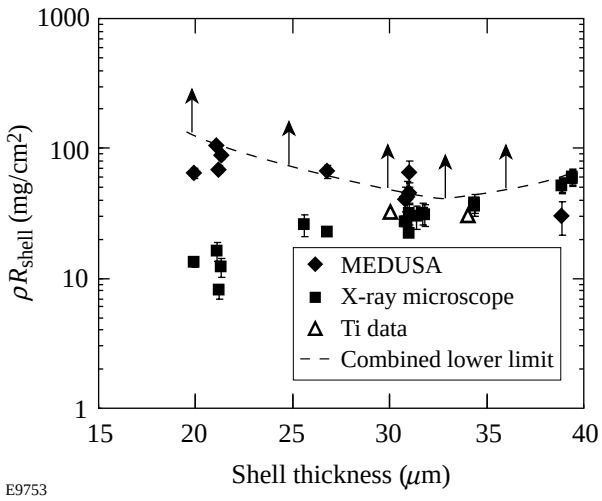

Figure 78.34
Combined upper-limit values on ρR_{shell} of the voided CD/CH shells imploded by 1-ns square pulses determined from both the x-ray and neutron spectra. Additional measurements determined from Ti-doped targets are shown to give consistent lower limits.

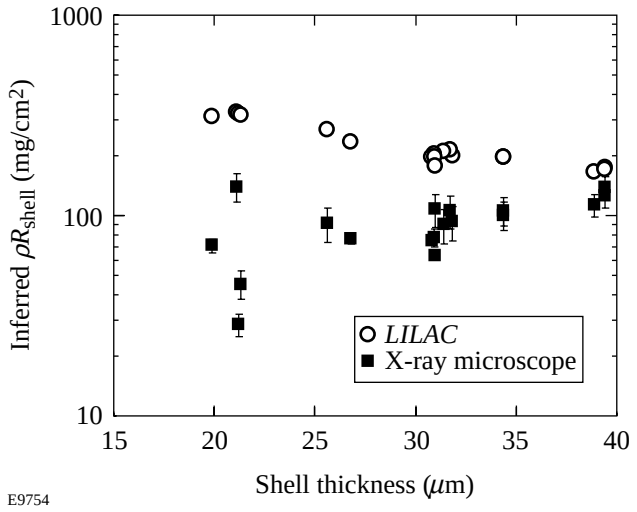

Figure 78.35
Estimates of ρR_{shell} for the voided CD/CH shells imploded by 1-ns square pulses determined from the lower limits (ρR_{cold}) given in Fig. 78.28. The values are determined assuming the ionization fraction predicted by *LILAC*.

areal densities as high as the thinner shells (at least as inferred by currently available techniques) despite the lower specific energy applied to the target, which implies that they are less affected by instabilities. All targets perform more poorly (lower yield, less compression) when imploded by the longer, shaped pulses because they have higher levels of laser imprint and lower ablative stabilization, which leads to large growth rates; thus, shaped-pulse implosions place more stringent requirements on power balance and initial target and illumination uniformity. For all pulse shapes, the gas-filled targets have the most significant increase in measured shell areal density when SSD is turned on (compared to DPP's only). This demonstrates the benefit of SSD in reducing the added instabilities that occur at the gas–shell interface. It is expected that as more-uniform illumination conditions are obtained, the thinner targets will outperform the thicker targets. This would be evidenced in higher neutron yields and higher areal densities as measured by x-ray and neutron spectral diagnostics.

ACKNOWLEDGMENT

The authors acknowledge the support of the staff at the Laboratory for Laser Energetics of the University of Rochester without whose many years of diligent work the OMEGA laser system would not exist. This work was supported by the U.S. Department of Energy Office of Inertial Confinement Fusion under Cooperative Agreement No. DE-FC03-92SF19460, the University of Rochester, and New York State Energy Research and Development Authority. The support of DOE does not constitute an endorsement by DOE of the views expressed in this article.

REFERENCES

1. T. R. Boehly, D. L. Brown, R. S. Craxton, R. L. Keck, J. P. Knauer, J. H. Kelly, T. J. Kessler, S. A. Kumpan, S. J. Loucks, S. A. Letzring, F. J. Marshall, R. L. McCrory, S. F. B. Morse, W. Seka, J. M. Soures, and C. P. Verdon, Opt. Commun. **133**, 495 (1997).

2. T. J. Murphy, J. M. Wallace, N. D. Delamater, C. W. Barnes, P. Gobby, A. A. Hauer, E. Lindman, G. Magelssen, J. B. Moore, J. A. Oertel, R. Watt, O. L. Landen, P. Amendt, M. Cable, C. Decker, B. A. Hammel, J. A. Koch, L. J. Suter, R. E. Turner, R. J. Wallace, F. J. Marshall, D. Bradley, R. S. Craxton, R. Keck, J. P. Knauer, R. Kremens, and J. D. Schnittman, Phys. Rev. Lett. **81**, 108 (1998).

3. J. D. Kilkenny, in *Current Trends in International Fusion Research*, edited by E. Panarella (Plenum Press, New York, 1997), pp. 295–296.

4. M. D. Rosen, Phys. Plasmas **3**, 1803 (1996).

5. J. T. Hunt *et al*., Lawrence Livermore National Laboratory, Livermore, CA, UCRL-JC-117399 (1994).

6. J. Nuckolls *et al*., Nature **239**, 139 (1972).

7. R. E. Kidder, Nucl. Fusion **19**, 223 (1979).

8. J. M. Soures, R. L. McCrory, C. P. Verdon, A. Babushkin, R. E. Bahr, T. R. Boehly, R. Boni, D. K. Bradley, D. L. Brown, R. S. Craxton, J. A. Delettrez, W. R. Donaldson, R. Epstein, P. A. Jaanimagi, S. D. Jacobs, K. Kearney, R. L. Keck, J. H. Kelly, T. J. Kessler, R. L. Kremens, J. P. Knauer, S. A. Kumpan, S. A. Letzring, D. J. Lonobile, S. J. Loucks, L. D. Lund, F. J. Marshall, P. W. McKenty, D. D. Meyerhofer, S. F. B. Morse, A. Okishev, S. Papernov, G. Pien, W. Seka, R. Short, M. J. Shoup III, M. Skeldon, S. Skupsky, A. W. Schmid, D. J. Smith, S. Swales, M. Wittman, and B. Yaakobi, Phys. Plasmas **3**, 2108 (1996).

9. D. K. Bradley, J. A. Delettrez, R. Epstein, R. P. J. Town, C. P. Verdon, B. Yaakobi, S. Regan, F. J. Marshall, T. R. Boehly, J. P. Knauer, D. D. Meyerhofer, V. A. Smalyuk, W. Seka, D. A. Haynes, Jr., M. Gunderson, G. Junkel, C. F. Hooper, Jr., P. M. Bell, T. J. Ognibene, and R. A. Lerche, Phys. Plasmas **5**, 1870 (1998).

10. P. C. Souers, *Hydrogen Properties for Fusion Energy* (University of California Press, Berkeley, 1986).

11. The Department of Energy's designated target supplier for the U.S. ICF Program is General Atomics, Inc., San Diego, CA 92121-1194.

12. T. J. Kessler, Y. Lin, L. S. Iwan, W. P. Castle, C. Kellogg, J. Barone, E. Kowaluk, A. W. Schmid, K. L. Marshall, D. J. Smith, A. L. Rigatti, J. Warner, and A. R. Staley, in *Solid State Lasers for Application to Inertial Confinement Fusion*, edited by M. L. André (SPIE, Bellingham, WA, 1997), Vol. 3047, pp. 272–281.

13. S. Skupsky, R. W. Short, T. Kessler, R. S. Craxton, S. Letzring, and J. M. Soures, J. Appl. Phys. **66**, 3456 (1989).

14. F. J. Marshall, J. A. Delettrez, R. Epstein, and B. Yaakobi, Phys. Rev. E **49**, 4381 (1994).

15. B. Yaakobi, R. Epstein, and F. J. Marshall, Phys. Rev. A **44**, 8429 (1991).

16. J. P. Knauer, R. L. Kremens, M. A. Russotto, and S. Tudman, Rev. Sci. Instrum. **66**, 926 (1995).

17. B. I. Bennett *et al*., Los Alamos National Laboratory Report LA-7130 (1978).

18. W. F. Huebner *et al.*, Los Alamos National Laboratory Report LA-6760-M (1977).

19. B. Yaakobi and F. J. Marshall, J. Quant. Spectrosc. Radiat. Transfer **61**, 465 (1999).

20. H. Azechi, M. D. Cable, and R. O. Stapf, Laser Part. Beams **9**, 119 (1991).

Simultaneous Measurements of Fuel Areal Density, Shell Areal Density, and Fuel Temperature in D^{3}He-Filled Imploding Capsules

Measurements of the charged-particle products of the fusion reactions from an imploding inertial fusion capsule can provide a direct means of characterizing key aspects of the implosion dynamics. Parameters such as the fusion yield, fuel ion temperature, capsule convergence, fuel and shell areal densities, and implosion asymmetry can be inferred by these measurements and can complement and augment similar measurements made using fusion neutrons or x-ray techniques. In addition, such measurements provide unique information on charging up the target and on charged-particle acceleration. In collaboration with MIT and LLNL, LLE has developed two charged-particle magnetic spectrometers that have been implemented on OMEGA.

An initial application of these spectrometers to characterize the compressed capsule parameters involved the compression of capsules containing a mixture of deuterium (D_2) and helium-three (^{3}He). The fusion reactions arising from such a fuel include three primary and four secondary reactions:

Primary:

$$\begin{aligned} \mathrm{D+D} \quad (50\%) &\rightarrow {}^3\mathrm{He}\,(0.82\ \mathrm{MeV}) + n(2.45\ \mathrm{MeV}) \\ (50\%) &\rightarrow \mathrm{T}\,(1.01\ \mathrm{MeV}) + p(3.02\ \mathrm{MeV}) \\ \mathrm{D} + {}^3\mathrm{He} &\rightarrow {}^4\mathrm{He}\,(3.6\ \mathrm{MeV}) + p(14.7\ \mathrm{MeV}) \end{aligned}$$

Secondary:

$$\begin{aligned} \mathrm{D+T} &\rightarrow {}^4\mathrm{He}\,(3.5\ \mathrm{MeV}) + n(14.1\ \mathrm{MeV}) \\ {}^3\mathrm{He} + \mathrm{T}\,(51\%) &\rightarrow {}^4\mathrm{He} + p + n\ 12.1\ \mathrm{MeV} \\ (43\%) &\rightarrow {}^4\mathrm{He}\,(4.8\ \mathrm{MeV}) + \mathrm{D}(9.5\ \mathrm{MeV}) \\ (6\%) &\rightarrow {}^5\mathrm{He}\,(2.4\ \mathrm{MeV}) + p(11.9\ \mathrm{MeV}) \end{aligned}$$

The richness of particles and energies produced by the fusion of D^{3}He provides the opportunity for simultaneous measurement of several key capsule parameters. First, by measuring the ratio of D-D protons (or neutrons) to D^{3}He protons, the temperature of the fuel ions at burn time can be inferred. Figure 78.36(a) plots the ratio of the D-D to D-^{3}He reaction rate as a function of ion temperature. Second, the spectrum of the emergent fusion-produced protons will be affected by energy loss upon escape from the capsule. The 3-MeV D-D protons, for example, have a range of approximately 40 mg/cm^2, whereas the 14.7-MeV D-^{3}He protons have a range greater than 300 mg/cm^2 [see Fig. 78.36(b)]. Measurements of the slowing down of the charged particles therefore indicate the capsule's total areal density at burn time. In addition, the yield of neutron secondaries from the D-D reaction provides an independent measure of the fuel areal density. Thus, it is possible, in principle, to obtain simultaneous characterization of yield, fuel temperature, shell areal density, and fuel areal density by measuring the spectrum of fusion particles emerging from the implosion and burn of a D^{3}He–filled capsule. A series of such measurements carried out on OMEGA with the newly implemented charged-particle spectrometers (CPS) in conjunction with the single-hit neutron detector array (MEDUSA) provided information on the secondary reaction product yield for these experiments.

Spectrometer Description

The charged-particle spectrometer[1] consists of a 7.6-kG permanent magnet with CR-39 track-etch detectors.[2] A schematic of the magnet and sample particle trajectories is shown in Fig. 78.37. Constructed of a neodymium–iron–boron alloy with a steel yoke, this dipole magnet weighs 160 lb and has a long dimension of 28 cm and a 2-cm gap between pole faces. CR-39 pieces are positioned throughout the dispersed beam, normal to the particle directions, using the mounting structure shown in Figs. 78.38(a) and 78.38(b), which allows greater than 80% coverage between the proton-equivalent energies of 0.1 to 57 MeV. Accurate, and calibrated, particle trajectory calculations determine the energy of particles arriving at each position on the detectors. The presence of multiple particle species is conveniently managed since, at any given detector position, the track diameters from each species are clustered into discrete diameter groups—the heavier particles (such as alphas) having larger diameters than the lighter particles (such as protons)—and thus may be easily distinguished. Identifica-

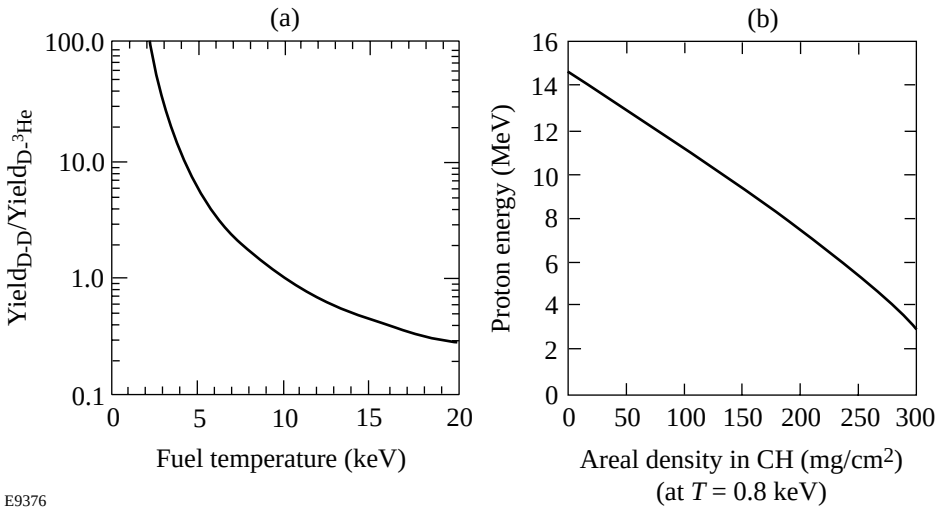

Figure 78.36
(a) Plot of the temperature dependence of the ratio of D-D fusion reactions to D-^{3}He reactions; (b) plot of the energy reduction as a function of areal density of 14.7-MeV protons traversing CH at a temperature of 800 keV.

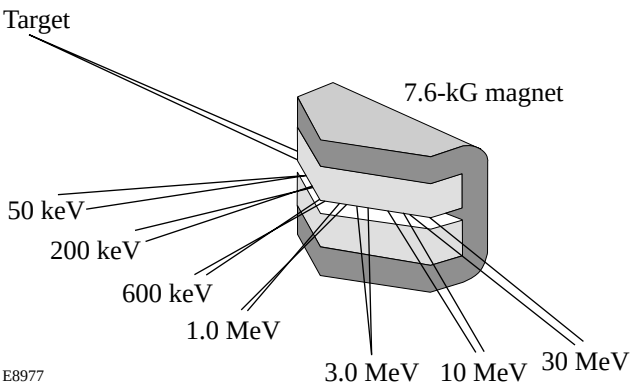

Figure 78.37
Schematic of the spectrometer and sample particle trajectories. A 7.6-kG pentagonal dipole magnet, 28 cm at its longest dimension, disperses protons in the range of 0.1 to 57 MeV. A linear array of CR-39 nuclear track detectors is placed normal to the dispersed beam. The large dynamic range of these detectors allows measurement of particle yields from 10^8 to 10^{17}.

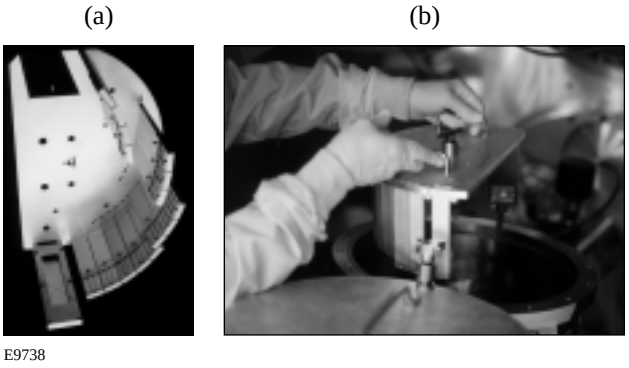

Figure 78.38
The mounting plate assembly that accurately positions pieces of CR-39 in the dispersion arc of the magnet. (a) The mounting plate assembly viewed from the perspective of the magnet. Pieces of CR-39 are positioned in each of the finger structures; these fingers are arranged in arcs that cover the dispersion region of the magnet. The finger at the bottom of the photo is positioned to view the target directly. X-ray film is placed at this position to ascertain the alignment of the spectrometer. The collimator slit is shown at the top of the photo. (b) The loaded mounting plate assembly being lowered onto the magnet (which is obscured) inside the vacuum chamber of CPS-1. After every shot, the mounting plate must be removed, and the CR-39 must be unloaded. A new, freshly loaded plate must then replace it in preparation for the next shot.

tion of each particle species is aided by using a track growth prediction model, calibrated to known particles and energies.

To assess the symmetry of all measurements, two virtually identical spectrometers are operating, one positioned inside the OMEGA chamber, at 100 cm from the target, and the other positioned outside, at 235 cm. The spectrometer inside the chamber is surrounded by a polyethylene-lead shielding structure designed to minimize the neutron noise levels on the CR-39. Incoming particles are collimated by a slit that can be varied from 1 to 10 mm wide, depending on the expected flux levels, giving solid angles between 10^{-6} and 10^{-5}. The measurement range of the instruments covers yields of 10^8 to more than 10^{17}, while the energy resolution is better than 4% over all energies. After every shot, the CR-39 detectors are removed from the spectrometer and replaced by a new set. The exposed detectors are then etched in sodium hydroxide and examined under a microscope. A rapid, automated scanning system has been developed that allows up to 10^6 tracks to be counted per shot.

Demonstration Experiments

Polymer ablator capsules, as illustrated in Fig. 78.39, were used to test the concept of simultaneous density and temperature measurements with D^{3}He–filled capsules. The principal diagnostics used for these experiments were the two charged-particle spectrometers, MEDUSA (to measure the fuel areal density via secondary reaction products[3]), and In activation (to measure the DD neutron yield).

In one series of shots, capsules of CH filled with a mixture of deuterium and ^{3}He were irradiated with up to 28.5 kJ in 1-ns near-square-top pulses with 2-D SSD beam smoothing. The capsule wall thickness ranged from 14.5 to 18.5 μm. Computer simulations of these implosions were performed using the one-dimensional hydrodynamic code *LILAC*,[4] and the spectra were calculated using the particle-tracking code *IRIS*.[5] The assumption of ideal performance (i.e., no mix, one-dimensional performance) in these simulations indicated that fuel ion temperatures in the range of 3.5 to 5.0 keV and capsule convergence ratios (ratio of initial target radius to compressed target radius) up to 28 could be achieved.

Figure 78.40 shows the measured proton spectrum obtained on one of these experiments. Table 78.V is a summary of the predicted and measured target parameters for this shot. The measured spectrum generally shows a greater slowing down for the thicker CH shells compared to thinner CH shells. This increased slowing down is apparent in the simulation results. The simulations, however, predict much larger areal densities, corresponding to an increased slowing down in the target, than are observed experimentally (Table 78.V), indicating departures from one-dimensional, unmixed implosions.

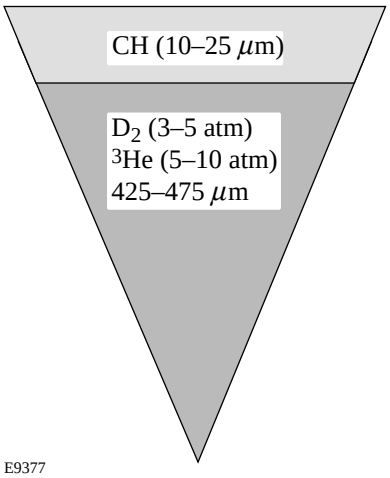

Figure 78.39
Polymer shell capsules filled with D^{3}He were used to test the CPS.

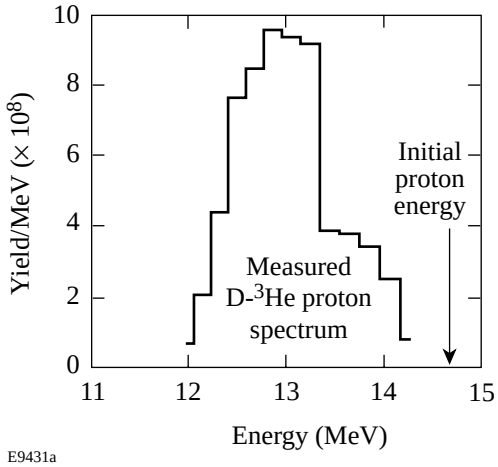

Figure 78.40
D-^{3}He proton spectrum measured on shot 13799. For this shot the laser energy was 28.3 kJ (1-ns square pulse), and the CH ablator was 18.4 μm thick. The capsule was filled with 2.8 atm of D_2 and 4.9 atm of ^{3}He.

Table 78.V: Predicted and Measured Parameters—Shot 13799.

Parameter	Predicted	Measured/Inferred
D-D neutron yield	5.4×10^{10}	2.1×10^{10}
D-^{3}He proton yield	3.1×10^{9}	1.3×10^{9}
Fuel temperature	3.6 KeV	3.9 keV
Proton downshift	4.2 MeV	1.9 MeV
Shell areal density	120 mg/cm^2	60 mg/cm^2
Fuel areal density	32 mg/cm^2	13 to 17 mg/cm^2
Convergence ratio	28	16 to 18

The simulated fuel temperature in Table 78.V is well reproduced by the experiment. This is probably due to the fact that higher temperatures occur earlier in the implosion history of the target when capsule conditions are closer to one-dimensional predictions. The difference between the measured and calculated areal densities is probably due to the fact that the areal density is predicted to increase later in the implosion. In this later phase, the mixing of the fuel and the shell due to hydrodynamic instabilities can cause significant departures from one-dimensional behavior and can reduce the fusion burn significantly. This may be the principal cause of the observed discrepancy between simulation and experiment. More detailed modeling using either mix models or multidimensional hydrodynamic simulations is necessary to correlate the measured spectra with conditions in the target. This analysis is presently being carried on.

In conclusion, simultaneous measurements of the fuel areal density, shell areal density, and fuel temperature have been carried out on OMEGA using D^{3}He–filled imploding capsules and the recently installed charged-particle spectrometers. The initial experiments demonstrated the ability to carry out these measurements at fuel ion temperatures of 3 to 6 keV, fuel areal densities in the range of 10 to 20 mg/cm^2, and shell areal densities in the range of 40 to 60 mg/cm^2. Measurements such as these can be applied to the parameter region characteristic of cryogenic-fuel capsules on OMEGA: total areal density of several hundred mg/cm^2 and fuel temperature of several keV. In future experiments, we will extend such measurements to higher fuel and shell areal densities and attempt to validate these techniques on cryogenic-fuel targets.

ACKNOWLEDGMENT

The authors acknowledge the support of the staff at the Laboratory for Laser Energetics of the University of Rochester without whose many years of diligent work the OMEGA laser system would not exist. This work was supported by the U.S. Department of Energy Office of Inertial Confinement Fusion under Cooperative Agreement No. DE-FC03-92SF19460, the University of Rochester, and New York State Energy Research and Development Authority. The support of DOE does not constitute an endorsement by DOE of the views expressed in this article.

REFERENCES

1. D. G. Hicks, C. K. Li, R. D. Petrasso, F. H. Seguin, B. E. Burke, J. P. Knauer, S. Cremer, R. L. Kremens, M. D. Cable, and T. W. Phillips, Rev. Sci. Instrum. **68**, 589 (1997).

2. T. W. Phillips *et al*., Rev. Sci. Instrum. **68**, 596 (1997).

3. M. D. Cable and S. P. Hatchett, J. Appl. Phys. **62**, 2233 (1987), and references therein.

4. E. Goldman, Laboratory for Laser Energetics Report No. 16, University of Rochester (1973).

5. S. Cremer, *IRIS* – a particle-tracking Monte Carlo code, 1992 (unpublished).

The Design of Optical Pulse Shapes with an Aperture-Coupled-Stripline Pulse-Shaping System

Laser-fusion experiments require precise control of the temporal profile of optical pulses applied to targets. An optical pulse–shaping system has been in operation on OMEGA for several years.[1] During this time the demands on the precision, flexibility, and repeatability of the optical pulse–shaping system have steadily increased. To meet these new demands, a new pulse-shaping system based on an aperture-coupled stripline (ACSL) electrical-waveform generator has been developed and discussed previously.[2] This new system will be implemented on OMEGA in the next few months. In addition to its simplicity, the new system will include significant improvements to the modeling, performance, and diagnostics of the pulse-shaping system to meet the challenging demands required of the system. The shaped optical pulses produced by this system become the seed pulses that are injected into the OMEGA laser system. Details of the on-target pulse shape from the OMEGA laser are critically related to the details of the seed-pulse shape. This article describes the modeling of an ACSL pulse-shaping system that is used to produce an optical seed pulse with a specified temporal shape.

An ACSL generates temporally shaped electrical waveforms that are applied to electro-optic modulators to produce shaped optical pulses. The electro-optic modulators exhibit a finite response time to an applied voltage. This response time has been measured and is included in the calculation of the voltage waveform required from the ACSL to produce a specific optical pulse shape. An ACSL is modeled as two coupled and interacting striplines. Striplines are modeled as transmission lines that obey a set of equations known as the telegraph equations.[3] A new approach to solving the telegraph equations using the method of characteristics is presented here along with a straightforward extension of this approach to ACSL's. The modeling presented here leads to a prescription for determining the necessary ACSL geometry to produce a desired on-target pulse shape on OMEGA.

The Optical Modulator Voltage Waveforms

Given the temporal profile of the optical pulse required on target from the OMEGA laser, the temporal profile of the optical seed pulse that must be produced by the pulse-shaping system is determined from the extensive modeling of the laser system that has evolved over the years. As shown in Fig. 78.41, this low-energy optical seed pulse is shaped by applying shaped voltage waveforms to a dual-channel electro-optic amplitude modulator synchronous with the transit through the modulator of an optical pulse from a single-longitudinal-mode (SLM) laser.[4] If we neglect the finite response time of the modulator, the intensity profile of an optical pulse exiting a modulator is given by

$$I_{\text{out}}(t) = I_{\text{in}}(t)\sin^2\left\{\pi/2\left[V_1(t)/V_\pi + \phi_1\right]\right\}$$

$$\times \sin^2\left\{\pi/2\left[V_2(t)/V_\pi + \phi_2\right]\right\}, \qquad (1)$$

where $I_{\text{in}}(t)$ is the intensity profile of the optical pulse sent into the modulator from the SLM laser; the two sine-squared factors represent the transmission functions of the two modulator channels with $V_1(t)$ the voltage waveform applied to channel 1 of the modulator, $V_2(t)$ the voltage waveform applied to channel 2 of the modulator, V_π the half-wave voltage of the modulator (typically less than 10 V), and ϕ_1 and ϕ_2 the offsets

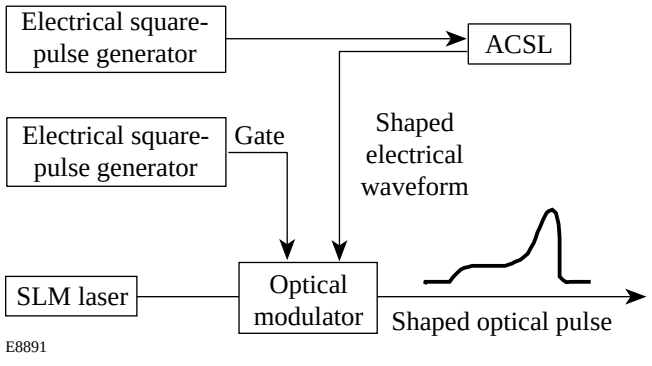

Figure 78.41
The aperture-coupled-stripline (ACSL) optical pulse–shaping system. The output from an electrical square-pulse generator is temporally shaped by an ACSL and used to drive an optical modulator. A separate electrical square-pulse generator is used to gate the second channel of the modulator.

set to zero by the application of a dc bias to each of the modulator channels. The input intensity profile to the modulator is assumed to be unity for our application since the short-duration (<5 ns) voltage waveforms $V_1(t)$ and $V_2(t)$ are applied to the modulators during the peak of the 200-ns Gaussian optical pulse from the SLM laser.

On one channel of the modulator, a shaped electrical waveform from an ACSL is applied. The exact shape of the voltage waveform required from the ACSL is determined by the shape of the optical pulse required from the modulator and by the response of the modulator to an applied voltage. This channel is referred to as the shaping channel of the modulator. On the other channel of the modulator, a square electrical waveform is applied. This channel is intended to produce a square optical waveform that acts as a gate to block unwanted pre- and post-pulses from the modulator and enhances the contrast of the output shaped optical pulse from the modulator. This channel of the modulator is referred to as the gate channel. The optical pulse produced by the gate channel should ideally have a fast rise and fall time with constant amplitude over its duration. The application of a square electrical pulse (with 45-ps rise time) to this channel from a pulse generator (Model 10,050A from Picosecond Pulsed Laboratories, Boulder, CO) produces the optical pulse shape shown in Fig. 78.42. This figure reveals the bandwidth limitations of the modulator for this "ideal" (high-bandwidth) square input electrical pulse. In particular, the optical pulse from this channel does not reach its full amplitude during the first 200 to 300 ps of the pulse, which, if not properly compensated for, can cause pulse distortion on the beginning of a shaped optical pulse and severe pulse distortion for short-pulse generation. This distortion caused by the modulator bandwidth limitation is minimized by including this effect when calculating the voltage waveform applied to the modulator's shaping channel as discussed below.

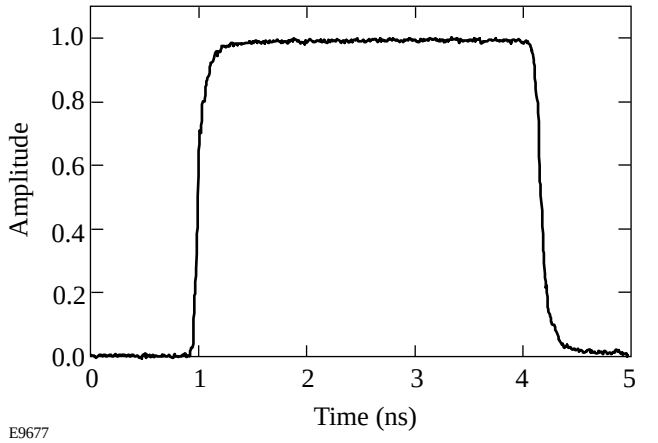

Figure 78.42
The measured optical pulse shape from a single channel of an electro-optic modulator with a square electrical waveform applied to the RF port. The square electrical waveform has a rise time of 45 ps.

Numerical Solution of the Telegraph Equations

Transmission line problems can be classified into two categories. The first category deals with determining the transmission line properties required to produce a specific electrical waveform reflected from the line, given the input electrical waveform to the line. The second category is the reciprocal of the first and deals with determining the electrical waveform reflected from a transmission line, given the input electrical waveform to the line and the properties of the transmission line.

In the present OMEGA pulse-shaping system, shaped electrical waveforms are generated by the reflection from a variable-impedance micro stripline and sent to the shaping channel of the modulator.[2] The micro striplines are designed using a layer-peeling technique that treats the micro stripline as a simple transmission line.[5] This technique allows one to calculate the reflection coefficient along the line (and from that the electrode width) needed to synthesize a given electrical waveform in reflection. The reciprocal of this calculation is to determine the electrical waveform reflected from a transmission line given the reflection coefficient along the line. This latter calculation is discussed here and, in the next section, will be extended to include modeling ACSL's to generate shaped electrical waveforms.

In this section we develop the equations that describe the electrical waveforms propagating along a transmission line starting from the well-known telegraph equations for the line.[3] First we model a stripline or micro stripline as a transmission line that obeys the telegraph equations:

$$\frac{\partial v(x,t)}{\partial x} = -L(x)\frac{\partial i(x,t)}{\partial t}, \tag{2a}$$

$$\frac{\partial i(x,t)}{\partial x} = -C(x)\frac{\partial v(x,t)}{\partial t}, \tag{2b}$$

where v is the voltage along the line, i is the current flowing along the line, L is the inductance per unit length along the line, and C is the capacitance per unit length along the line. In these

equations we introduce the characteristic impedance of the line $Z(x) = \sqrt{L(x)/C(x)}$ and the wave propagation velocity $dx/dt = c = 1/\sqrt{LC}$ along the line. We assume that the propagation velocity c (not to be confused with the speed of light) along the line is constant. With these substitutions Eqs. (2) become

$$\frac{\partial V(x,t)}{\partial x} = -k(x)V(x,t) - c\frac{\partial I(x,t)}{\partial t}, \tag{3a}$$

$$\frac{\partial I(x,t)}{\partial x} = k(x)I(x,t) - c\frac{\partial V(x,t)}{\partial t}, \tag{3b}$$

where the variables are defined as

$$V(x,t) = v(x,t)Z^{-1/2}(x) \tag{4a}$$

and

$$I(x,t) = i(x,t)Z^{1/2}(x) \tag{4b}$$

and where

$$k(x) = \frac{1}{2Z(x)}\frac{dZ(x)}{dx} \tag{5}$$

is the reflection coefficient per unit length along the line.

If we add and subtract Eqs. (3), we get a set of reduced wave equations

$$\frac{\partial WR(x,t)}{\partial x} + \frac{1}{c}\frac{\partial WR(x,t)}{\partial t} = -k(x)WL(x,t) \tag{6a}$$

and

$$\frac{\partial WL(x,t)}{\partial x} + \frac{1}{c}\frac{\partial WL(x,t)}{\partial t} = -k(x)WR(x,t), \tag{6b}$$

where

$$WR(x,t) = \left[V(x,t) + I(x,t)\right]/2$$

$$= \left[v(x,t)Z^{-1/2}(x) + i(x,t)Z^{1/2}(x)\right]/2 \tag{7a}$$

is a wave traveling to the right along the line with velocity c and

$$WL(x,t) = \left[V(x,t) - I(x,t)\right]/2$$

$$= \left[v(x,t)Z^{-1/2}(x) - i(x,t)Z^{1/2}(x)\right]/2 \tag{7b}$$

is a wave traveling to the left along the line with velocity c. In the appendix we show that the form of Eqs. (6) is identical to the form of the equation obtained if one substitutes a plane wave with slowly varying amplitude into the wave equation. Therefore, Eqs. (6) are referred to as the reduced wave equations and are the main results of this section. In the next section we show how to extend these equations to model an ACSL and give a numerical prescription for solving the resulting equations using the method of characteristics.

Extension to an ACSL

The geometry of an ACSL is shown in Fig. 78.43. In principle, an ACSL is a directional coupler consisting of two striplines that are coupled through an aperture in their common ground plane. In operation, a square electrical waveform is launched into port 1 and propagates along electrode 1 to the terminated port 2 of the ACSL. As the square electrical waveform propagates along electrode 1 in the coupling region, a signal is coupled through an aperture to electrode 2 in the backward direction and exits at port 4. The electrical waveform exiting port 4 is sent to the shaping channel of the modulator and must have the proper temporal profile to produce the desired optical pulse shape out of the modulator. By varying the width of the coupling aperture (shown in Fig. 78.43) along the length of the ACSL, a temporally shaped electrical waveform can be generated at port 4. The details of how to calculate the width of this aperture along the line to produce a specific electrical waveform from the ACSL are the main topic of this article.

The ACSL is modeled as two coupled transmission lines. We can extend the formalism in the previous section to an ACSL by writing four reduced wave equations. Two equations describe the waves WR1(x,t) and WR2(x,t) traveling to the right along lines 1 and 2, respectively, and two equations describe the waves WL1(x,t) and WL2(x,t) traveling to the left along lines 1 and 2, respectively. In each reduced wave equation we include the reflection coefficient $k(x)$ along the line as above, and we introduce a coupling term $C(x)$ that allows for coupling waves from one line to the other through the aperture.

The resulting equations are given by

$$\frac{\partial \mathrm{WR1}(x,t)}{\partial x} + \frac{1}{c}\frac{\partial \mathrm{WR1}(x,t)}{\partial t} = -k(x)\,\mathrm{WL1}(x,t) - C(x)\,\mathrm{WL2}(x,t), \tag{8a}$$

$$\frac{\partial \mathrm{WL1}(x,t)}{\partial x} - \frac{1}{c}\frac{\partial \mathrm{WL1}(x,t)}{\partial t} = -k(x)\,\mathrm{WR1}(x,t) - C(x)\,\mathrm{WR2}(x,t), \tag{8b}$$

$$\frac{\partial \mathrm{WR2}(x,t)}{\partial x} + \frac{1}{c}\frac{\partial \mathrm{WR2}(x,t)}{\partial t} = -k(x)\,\mathrm{WL2}(x,t) - C(x)\,\mathrm{WL1}(x,t), \tag{8c}$$

$$\frac{\partial \mathrm{WL2}(x,t)}{\partial x} - \frac{1}{c}\frac{\partial \mathrm{WL2}(x,t)}{\partial t} = -k(x)\,\mathrm{WR2}(x,t) - C(x)\,\mathrm{WR1}(x,t). \tag{8d}$$

The coupling coefficient $C(x)$ is the coupling from one line to the other in the backward direction. In general, another coupling term should be added to the above equations to model coupling from one line to the other in the forward direction. This forward coupling term can be trivially added to this model; however, for directional couplers of this sort, coupling in the forward direction is negligible.

The reduced wave equations (8) for an ACSL [as well as Eqs. (6) for striplines] can be solved by transforming them along the characteristic curves

$$\xi = ct - x \quad \text{and} \quad \eta = ct + x. \tag{9}$$

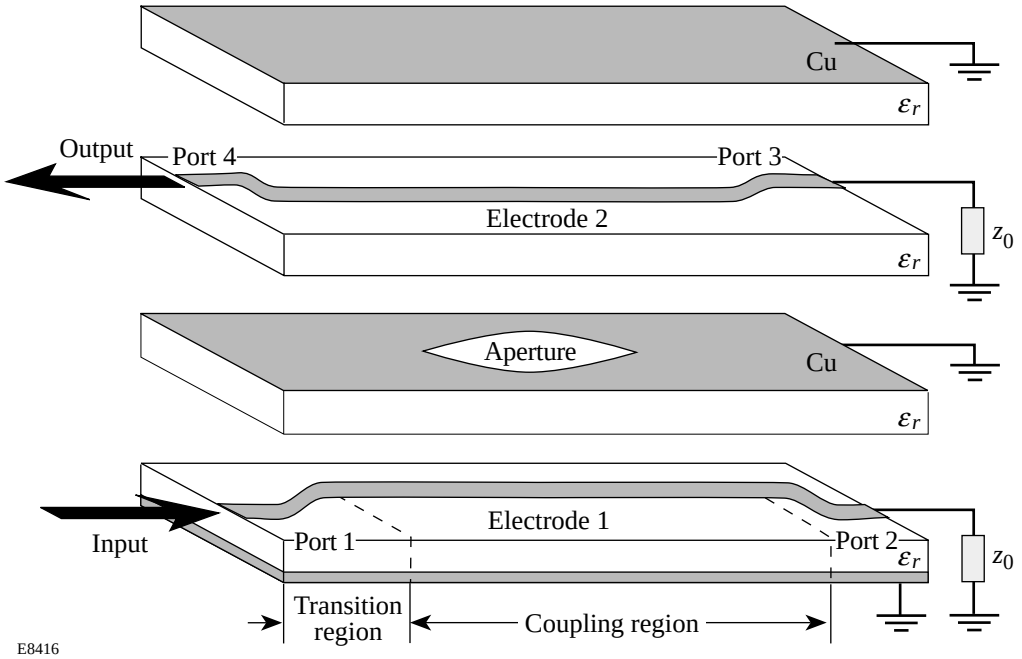

Figure 78.43
Exploded view of a practical four-layer, four-port ACSL. A square electrical waveform is launched into port 1 and propagates along electrode 1 to the terminated port 2. An electrical signal is coupled through an aperture to electrode 2 in the backward direction, and a shaped electrical waveform exits at port 4.

For this transformation we use the chain rules

$$\frac{\partial}{\partial x}=\frac{\partial}{\partial \xi}\frac{\partial \xi}{\partial x}+\frac{\partial}{\partial \eta}\frac{\partial \eta}{\partial x}=\left(-\frac{\partial}{\partial \xi}+\frac{\partial}{\partial \eta}\right) \tag{10a}$$

and

$$\frac{\partial}{\partial t}=\frac{\partial}{\partial \xi}\frac{\partial \xi}{\partial t}+\frac{\partial}{\partial \eta}\frac{\partial \eta}{\partial t}=c\left(\frac{\partial}{\partial \xi}+\frac{\partial}{\partial \eta}\right) \tag{10b}$$

to obtain

$$\frac{\mathrm{dWR1}(\eta)}{\mathrm{d}\eta}=-\left[k(x)\mathrm{WL1}(\xi)+C(x)\,\mathrm{WL2}(\xi)\right]/2, \tag{11a}$$

$$\frac{\mathrm{dWL1}(\xi)}{\mathrm{d}\xi}=\left[k(x)\,\mathrm{WR1}(\eta)+C(x)\,\mathrm{WR2}(\eta)\right]/2, \tag{11b}$$

$$\frac{\mathrm{dWR2}(\eta)}{\mathrm{d}\eta}=-\left[k(x)\mathrm{WL2}(\xi)+C(x)\mathrm{WL1}(\xi)\right]/2, \tag{11c}$$

$$\frac{\mathrm{dWL2}(\xi)}{\mathrm{d}\xi}=\left[k(x)\mathrm{WR2}(\eta)+C(x)\mathrm{WR1}(\eta)\right]/2, \tag{11d}$$

where we have used the fact that WR1,2 are waves propagating in the positive x direction and WL1,2 are waves propagating in the negative x direction and obey wave equations with solutions of the form

$$\mathrm{WR1,2}(x,t)=\mathrm{WR1,2}(ct+x)=\mathrm{WR1,2}(\eta) \tag{12a}$$

and

$$\mathrm{WL1,2}(x,t)=\mathrm{WL1,2}(ct-x)=\mathrm{WL1,2}(\xi). \tag{12b}$$

With this transformation the derivatives in Eqs. (11) become total derivatives.

The coordinate transformation expressed by Eqs. (9) lends itself to a simple geometric interpretation that leads to a numerical solution algorithm for the reduced-wave Eqs. (11). The transformation Eqs. (9) with $\mathrm{d}x = c\mathrm{d}t$ can be seen to be a rotation of the x,ct coordinate system by 45° into the ξ,η coordinate system as shown in Fig. 78.44. In the new ξ,η coordinate system, Eqs. (11) describe how the right-going waves WR1,2 evolve in the η direction and how the left-going waves WL1,2 evolve in the ξ direction. The differential element in this new system is seen to be

$$\mathrm{d}\eta=\frac{\partial \eta}{\partial x}\mathrm{d}x+\frac{\partial \eta}{\partial t}\mathrm{d}t=\mathrm{d}x+c\mathrm{d}t=2\mathrm{d}x, \tag{13}$$

where we have used $\mathrm{d}x = c\mathrm{d}t$. To solve Eqs. (11) numerically, we define a matrix as shown in Fig. 78.44 for each of the four waves and write the finite difference equations

$$\mathrm{WR1}(i,j)=\mathrm{WR1}(i-1,j-1)$$

$$-\left[k(i)\,\mathrm{WL1}(i+1,j-1)+C(i)\,\mathrm{WL2}(i+1,j-1)\right]\mathrm{d}x, \tag{14a}$$

$$\mathrm{WL1}(i,j)=\mathrm{WL1}(i+1,j-1)$$

$$-\left[k(i)\,\mathrm{WR1}(i-1,j-1)+C(i)\,\mathrm{WR2}(i+1,j-1)\right]\mathrm{d}x, \tag{14b}$$

$$\mathrm{WR2}(i,j)=\mathrm{WR2}(i-1,j-1)$$

$$-\left[k(i)\,\mathrm{WL2}(i+1,j-1)+C(i)\,\mathrm{WL1}(i+1,j-1)\right]\mathrm{d}x, \tag{14c}$$

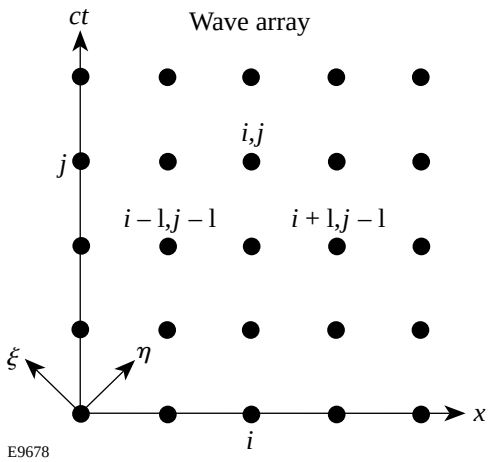

Figure 78.44
An array used by the numerical solution technique to represent a wave propagating along a transmission line. The value at each location in the array gives the amplitude of the wave at some fixed position along the line at some time. Four such arrays are used in the calculation to represent the four waves propagating in an ACSL.

$$\mathrm{WL2}(i,j) = \mathrm{WL2}(i+1, j-1)$$

$$-\left[k(i)\,\mathrm{WR2}(i-1, j-1) + C(i)\,\mathrm{WR1}(i+1, j-1)\right]\mathrm{d}x, \quad (14\mathrm{d})$$

where the index i represents the position x along the line and the index j represents the time t. In these equations, for example, the value of the matrix element at the location i,j in the WR1 array is the amplitude of the wave WR1 at position x along the line at time t. Equations (14) give the values of the four waves at some time, given values of the waves at an earlier time and the reflection and coupling coefficients (k and C) along the line. Therefore, given the coupling coefficients and the initial values of the waves along the line (at $j = 0$ for all i) and the values of the waves at the boundaries for all time (at the first and last i value for all j), Eqs. (14) can be used to find all other values in the arrays. Knowing all values in the four arrays determines the amplitudes of the four waves at all locations along the line for all time. In particular, we specify the right-going wave on line 1 (the pulse from the pulse generator applied to port 1), and we calculate the left-going wave on line 2 (the pulse at port 4 that is applied to the modulator shaping channel). In the next section we show how to apply this technique to the design of optical pulse shapes from the ACSL pulse-shaping system.

Optical Pulse Shape Design/Performance

It is important to use actual measured waveforms or accurately modeled waveforms as input to the pulse-shaping model whenever possible to compensate for imperfections introduced by these waveforms that cannot be corrected by other means. The temporally shaped voltage waveform [V_2 in Eq. (1)] that must be produced by the ACSL and applied to the pulse-shaping channel of the modulator is calculated from Eq. (1). In Eq. (1), I_{out} is the desired temporally shaped optical pulse from the modulator, and the gate channel transmission function is modeled after data similar to that shown in Fig. 78.42. With these substitutions in Eq. (1), the required voltage waveform V_2 is determined, and an ACSL can be designed and fabricated to produce this voltage waveform.

The numerical solution described in the previous section allows one to calculate the electrical waveforms from all four ports of an ACSL given the reflection coefficient $k(x)$ and coupling coefficient $C(x)$ along the line. Experiments show that for any aperture width along the line, these coefficients are equal at each point along the line. To obtain a first approximation to these coefficients a modified version of the layer-peeling technique[5] is used. In the modified layer-peeling technique, the effective reflection coefficient at each point along the line is calculated given the desired output electrical waveform from port 4 and given an ideal input square electrical pulse (i.e., square pulse with an infinite bandwidth) applied to port 1 of the ACSL. (The layer-peeling technique, unfortunately, has difficulties when using an actual measured electrical waveform as input to the line.) Using this first approximation for the reflection and coupling coefficients and using the measured electrical square pulse from the square-pulse generator (Model 4500E from Picosecond Pulsed Laboratories) as input to port 1 of the ACSL, the shaped voltage waveform exiting port 4 of the ACSL is calculated as described in the previous section. This calculated electrical waveform from port 4 of the ACSL is then compared to the required electrical waveform V_2 from this port; this comparison is then used to derive a second approximation to the coupling coefficients. This iteration process can be continued until the calculated output waveform from port 4 of the ACSL is identical to the required output waveform to any degree of accuracy (in practice, one iteration gives sufficient accuracy). Once the coupling coefficient C is determined in this way, the aperture width along the line is obtained from the relationship of the aperture width to the coupling coefficient shown in Fig. 78.45.[2]

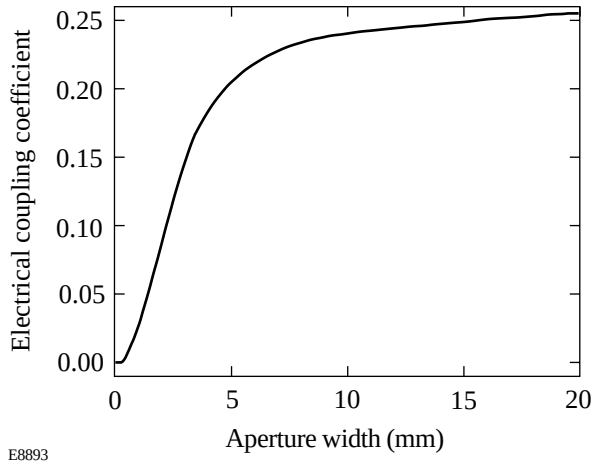

Figure 78.45
The electrical coupling coefficient, defined as the ratio of the output voltage at port 4 to the input voltage applied to port 1 shown in Fig. 78.43, plotted as a function of aperture width for an ACSL with the geometry discussed in the text.

Figure 78.46 shows the design of a specific pulse shape for the OMEGA laser. In Fig. 78.46(a), the design voltage waveform V_2 is compared to the measured voltage waveform from port 4 of the fabricated ACSL. In Fig. 78.46(b), the design optical waveform required from the modulator is compared

to the measured optical waveform from the modulator. Figure 78.46(c) shows the predicted on-target OMEGA UV pulse shape calculated from the measured optical pulse shape from the modulator [Fig. 78.46(b)] and compared to the desired on-target OMEGA UV pulse shape.

Summary

In conclusion, an ACSL pulse-shaping system will be implemented on OMEGA. A model has been developed that allows one to produce accurately shaped optical pulses suitable for injection into the OMEGA laser system. The ACSL electrical-waveform generator is modeled with a numerical solution of the telegraph equations using the method of characteristics. The model uses as input the measured electrical square pulse from the pulse generator used in the pulse-shaping system. The model also compensates for the pulse-shape distortion due to bandwidth limitations of the modulator introduced primarily by the gate pulse. The ACSL pulse-shaping system is a significant improvement over the existing pulse-shaping system currently on OMEGA because of its simplicity, enhanced performance and diagnostics, and improved modeling capabilities.

ACKNOWLEDGMENT

The authors acknowledge the support of the staff at the Laboratory for Laser Energetics of the University of Rochester without whose many years of diligent work the OMEGA laser system would not exist. This work was supported by the U.S. Department of Energy Office of Inertial Confinement Fusion under Cooperative Agreement No. DE-FC03-92SF19460, the University of Rochester, and New York State Energy Research and Development Authority. The support of DOE does not constitute an endorsement by DOE of the views expressed in this article.

Appendix A: Derivation of the Reduced Wave Equation

In this appendix we derive the reduced wave equation that results by substituting a plane wave with slowly varying amplitude into the wave equation. For simplicity, we assume that the

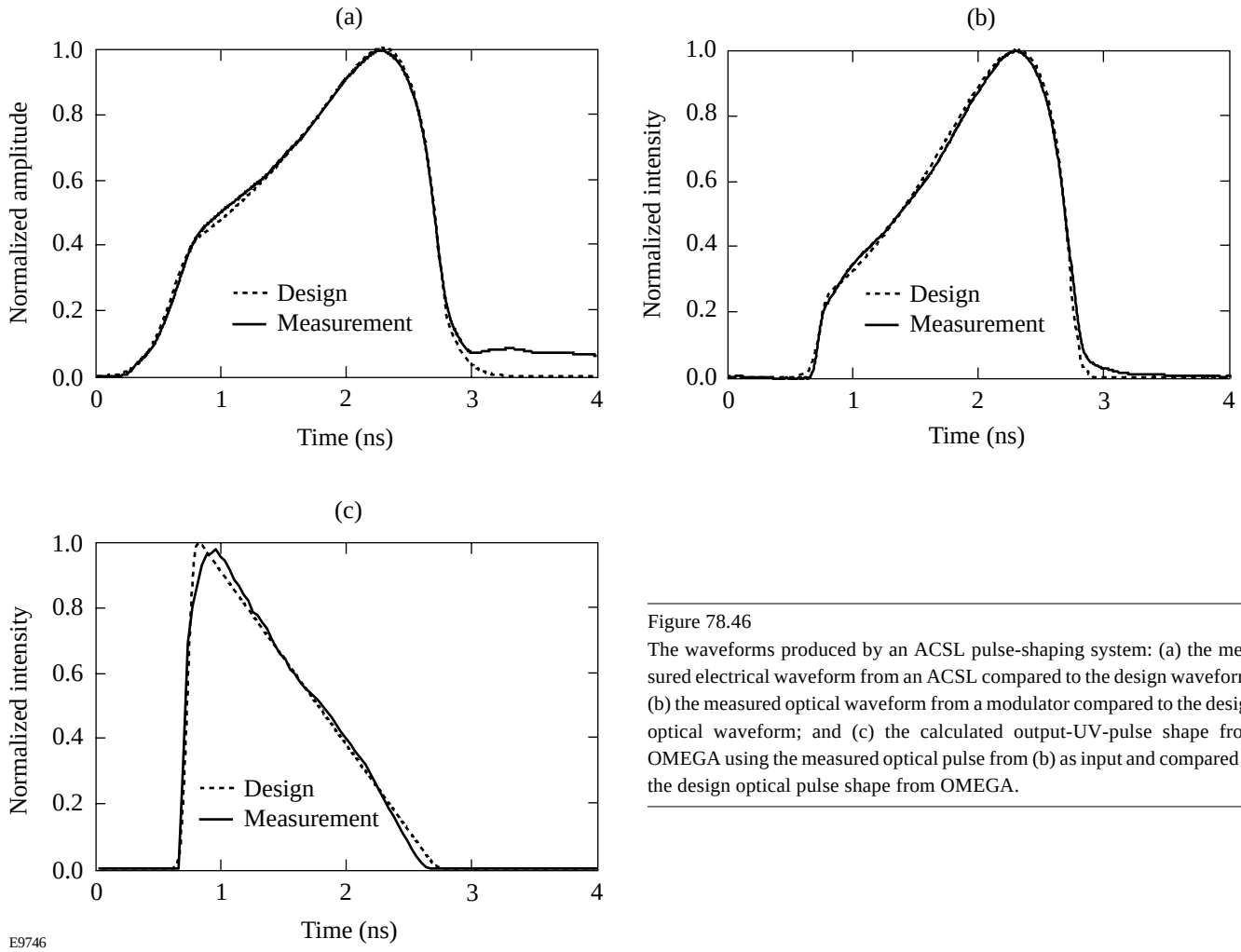

Figure 78.46
The waveforms produced by an ACSL pulse-shaping system: (a) the measured electrical waveform from an ACSL compared to the design waveform; (b) the measured optical waveform from a modulator compared to the design optical waveform; and (c) the calculated output-UV-pulse shape from OMEGA using the measured optical pulse from (b) as input and compared to the design optical pulse shape from OMEGA.

wave is linearly polarized and propagating in the x direction in a nondispersive medium. The plane wave can be represented by

$$E_{\pm}(x,t) = A_{\pm}(x,t)\exp\left[i(\omega t \mp kx)\right] + \text{cc}, \qquad \text{(A1)}$$

where $A_{\pm}$ is the complex amplitude of the wave, the upper sign representing a wave propagating to the right and the lower sign representing a wave propagating to the left; $\omega = 2\pi\nu$ is the angular frequency of the wave with frequency ν; $k = 2\pi/\lambda$ is the propagation constant of the wave with wavelength λ; and cc implies complex conjugate. The purpose of representing the waves in this form is to factor out the slow variations (the temporal profile of the electrical waveform) from the rapid oscillations (referenced to some microwave carrier frequency $\omega/2\pi$). The one-dimensional wave equation is given by

$$\frac{\partial^2 E_{\pm}(x,t)}{\partial x^2} - \frac{1}{c^2}\frac{\partial^2 E_{\pm}(x,t)}{\partial t^2} = 0, \qquad \text{(A2)}$$

where $c = \omega/k$ is the velocity of the wave. If we substitute A1 into A2, after some manipulation we get

$$\frac{\partial^2 A_{\pm}}{\partial x^2} \mp 2ik\frac{\partial A_{\pm}}{\partial x} - \frac{1}{c^2}\frac{\partial^2 A_{\pm}}{\partial t^2} + 2i\frac{\omega}{c^2}\frac{\partial A_{\pm}}{\partial t} = 0, \qquad \text{(A3)}$$

where we have used $c = \omega/k$ to eliminate terms. We now use the fact that the amplitude is slowly varying, that is

$$\frac{\partial A_{\pm}}{\partial x} << \left| kA_{\pm} \right| \qquad \text{(A4a)}$$

and

$$\frac{\partial A_{\pm}}{\partial t} << \left| \omega A_{\pm} \right|. \qquad \text{(A4b)}$$

Equation (A4a) implies that the amplitude of the wave does not change significantly over a distance of one wavelength λ, and Eq. (A4b) implies that the amplitude of the wave does not change significantly over a time duration of $1/\nu$. With these slowly varying amplitude approximations, Eq. (A3) reduces to

$$\frac{\partial A_{\pm}(x,t)}{\partial x} \mp \frac{1}{c}\frac{\partial A_{\pm}(x,t)}{\partial t} = 0. \qquad \text{(A5)}$$

This equation is the reduced wave equation referred to in the text.

REFERENCES

1. A. V. Okishev, W. Seka, J. H. Kelly, S. F. B. Morse, J. M. Soures, M. D. Skeldon, A. Babushkin, R. L. Keck, and R. G. Roides, in *Conference on Lasers and Electro-Optics*, *Vol. 11*, 1997 OSA Technical Digest Series (Optical Society of America, Washington, DC, 1997), p. 389.

2. Laboratory for Laser Energetics LLE Review **73**, 1, NTIS document No. DOE/SF/19460-212 (1997). Copies may be obtained from the National Technical Information Service, Springfield, VA 22161.

3. W. C. Johnson, *Transmission Lines and Networks*, 1st ed., McGraw-Hill Electrical and Electronic Engineering Series (McGraw-Hill, New York, 1950).

4. A. V. Okishev and W. Seka, IEEE J. Sel. Top. Quantum Electron. **3**, 59 (1997).

5. S. C. Burkhart and R. B. Wilcox, IEEE Trans. Microw. Theory Tech. **38**, 1514 (1990).

Measurement Technique for Characterization of Rapidly Time- and Frequency-Varying Electronic Devices

The conventional method for measuring the transfer function of an electronic device uses Fourier transform theory and convolutions and is, therefore, limited to either time-invariant or frequency-invariant devices. The measurement technique presented here enables the complete characterization of electronic devices having any dynamic temporal and spectral frequency response. A technique presented earlier[1] applied the windowing of signals in the time and frequency domains (called time-frequency distributions) to characterize photoconductive switches that vary in time *and* frequency; however, windowing requires a slowly varying envelope approximation, which limits the allowed rate of temporal and spectral variations. The more general technique allows us to measure the frequency response of the optoelectronic (photoconductive) microwave switches on OMEGA's pulse-shaping system. Unlike microwave diode switches, photoconductive switches do not have a constant conductive on-state, but rather decay monotonically to the off-state after the illumination ceases. A complete linear model for such a device must incorporate both filtering and modulation into a general time-varying filter (or equivalently, band-limited modulator). Any microwave or millimeter-wave device whose properties vary rapidly requires the application of this technique for complete characterization, including elements that depend on charge-carrier dynamics such as photoconductive attenuators, phase shifters, and directional couplers.

The general concept of a linear, time-varying filter is well established in the signal-processing,[2,3] communication,[4] and automatic control[5] fields. In the microwave-device field, however, the linear variations of filter properties are typically due to slowly varying mechanisms (e.g., mechanical) or are generated by rapid transitions between steady-state regimes (e.g., microwave diode switches); therefore, a form of windowing is usually adequate for characterization. The analysis presented here introduces a characterization technique analogous to (and a superset of) a form of input–output relationships called the scattering or *S* parameters, which can be applied to devices that can be considered linear filters with rapid modulation of amplitude and/or phase (e.g., photoconductive switches). In the next section we briefly discuss the complementary relationship between linear filters and linear modulators. From this conceptual viewpoint, we derive an extension of the filter and modulator characterization functions $S(\omega)$ and $k(t)$ to a general linear device characterization or system function $\tilde{S}(\omega, t)$. Based on the limitations of conventional *S*-parameter analysis in the **Mathematical Formulation** section, we present some important properties of the $\tilde{S}$ parameter and explain conditions under which this form of analysis can be implemented. In the **Analytical Example** section we apply our $\tilde{S}$-parameter concept to device analysis by considering a simplified lumped-element example, deriving the $\tilde{S}$ parameters from the theory and directly from the differential equations, and demonstrate the limitations of windowing. Photoconductive switches used on OMEGA pulse shaping have been optimized through the application of the $\tilde{S}$-parameter technique; these results will be presented in a separate article.

Background

Conventional microwave device characterization depends on shift-invariant device models for characterization, taking advantage of the property that a convolution in one domain Fourier transforms to multiplication in the other. In Table 78.VI the canonical input–output relationships of the two ideal shift-invariant microwave devices are presented to emphasize their complementary nature. All dependent variables are complex, $a(\omega)$ and $b(\omega)$ are the Fourier transforms of the respective input and output temporal power waves $A(t)$ and $B(t)$, $S(\omega)$ and $h(t)$ are the scattering parameter and its Fourier transform (the impulse response), k and K are the modulation parameter and its Fourier transform, and the subscripts refer to the microwave input–output ports of the device. The linear-frequency-invariant (LFI) model of a modulator is valid when narrow-band input signals (relative to the modulator bandwidth) are applied, and the linear-time-invariant (LTI) filter model is valid when the device's temporal variations are longer than the signal duration. Note that here and throughout this article, for the convenience of using notation familiar in measurement practice, we use ω for $j\omega$ and draw no distinction between real and analytic time-series signals.

Table 78.VI: A comparison of the transfer functions of shift-invariant devices: an ideal, linear-time-invariant (LTI) filter and frequency-invariant (LFI) modulator.

	Time Domain	Frequency Domain
Time-invariant filter	$B_i(t) = \int_{-\infty}^{\infty} h_{ij}(t-\tau)\, A_j(\tau)\, d\tau$	$b_i(\omega) = S_{ij}(\omega) \cdot a_j(\omega)$
Frequency-invariant modulator	$B_i(t) = k_{ij}(t) \cdot A_j(t)$	$b_i(\omega) = \int_{-\infty}^{\infty} K_{ij}(\omega - \xi) \cdot a_j(\xi)\, d\xi$

The analysis based on the equations in Table 78.VI cannot be applied to a device that is neither time invariant nor frequency invariant. As Fig. 78.47 indicates, a time-varying filter will have different impulse responses at different times [(b) and (c)], or equivalently a modulator with finite frequency response will modulate different frequencies differently [(d) and (e)]; so neither model in Table 78.VI is adequate for complete characterization. If the device can be held constant in one domain independently of the other, or if the variations are slow relative to the signal applied, conventional analysis can be applied by using some form of windowing; inaccuracies will depend on how strongly the LTI or LFI assumptions are violated. If the filtering and modulating aspects of this general linear device cannot be controlled independently (i.e., cannot be made separable) and the variations in time and frequency are rapid, characterization of the device under test (DUT) using either $k(t)$ modulator functions or $S(\omega)$ filter parameters cannot account for complete device behavior. Since conventional methods of linear microwave circuit characterization (e.g., spectrum and network analyzers) are based on the application of Fourier transforms and the convolution integral, their use can lead to incorrect or even misleading characterization results.

Motivated by these limitations, we combine the separate (but complementary) one-dimensional (1-D) LTI and LFI transfer functions to a single two-dimensional (2-D) transfer (or system) function, calling it $\tilde{S}(\omega, t)$ to emphasize its similarity to conventional $S(\omega)$ parameters. For illustration, a conceptual example of the amplitude of an exponentially decaying, low-pass filter is shown in Fig. 78.47(f). This 2-D parameter can be more difficult to measure than a conventional device's $S(\omega)$ parameters; however, the measurement process can be simplified by taking advantage of the 2-D nature of $\tilde{S}$ and using methods that are not applicable 1-D functions. For example, the theory of generalized projections as used in 2-D phase retrieval allows us to reconstruct the full, vector (complex) 2-D transfer function $\tilde{S}$ by measuring only the magnitude $|\tilde{S}|$. Although generalized projections are restricted to functions that are zero outside some finite temporal and spectral window (i.e., that have known, compact support along both axes[6]), in practice the transfer functions of microwave devices satisfy this criteria.

$\tilde{S}(\omega, t)$ can be applied to device characterization in the *frequency domain* or the *time domain*. Conceptually, in the frequency-domain approach a single-frequency wave can be applied to the DUT for the time duration of interest, and then the temporal evolution of the resulting output signal's amplitude and phase can be recorded. Next, to separate the device's effect on signal amplitude and phase, the same input wave is applied, phase shifted by $\pi/4$, over the same time duration relative to the trigger, and again the temporal evolution of amplitude and phase is recorded (i.e., this is equivalent to measuring the analytic signal). Finally, by reapplying signals at different frequencies, a map of $\tilde{S}(\omega, t)$ can be generated for the DUT by constructing successive time slices at each frequency. Alternatively, in the time-domain approach a series of impulse functions can be applied at appropriate time intervals over the period of interest, and the impulse response corresponding to each input can be recorded. Although these descriptions are intuitively appealing, it may not be readily apparent how to extract an input–output relationship such as $\tilde{S}(\omega, t)$ from the measured signals, apply it to the calculation of output signals given an arbitrary input signal properly, and avoid the effects of windowing. The following analysis will clarify the technique and the method of calculation.

Mathematical Formulation

To derive a combined system function $\tilde{S}(\omega, t)$ that is capable of characterizing the input–output relationships of devices that are neither exclusively modulators nor filters and is easily determined by measuring the incident and emerging signals, we must revisit some of the assumptions used in microwave circuit/network analysis and synthesis. To emphasize the utility of our more generalized transfer function, we will frame our discussion in terms of filters and *S*-parameter characterization; however, the system function $\tilde{S}(\omega, t)$ sub-

sumes both LFI and LTI devices as special cases, so it is equally applicable to modulators. The route taken is motivated by the observation that, in the equations for filters and modulators presented in the previous section, the roles of time and frequency are complementary, i.e., the 1-D characterization functions are along orthogonal axes in the complex plane. From this comes the realization that a more general, 2-D characterization is possible by considering and measuring the device's response on the entire plane.

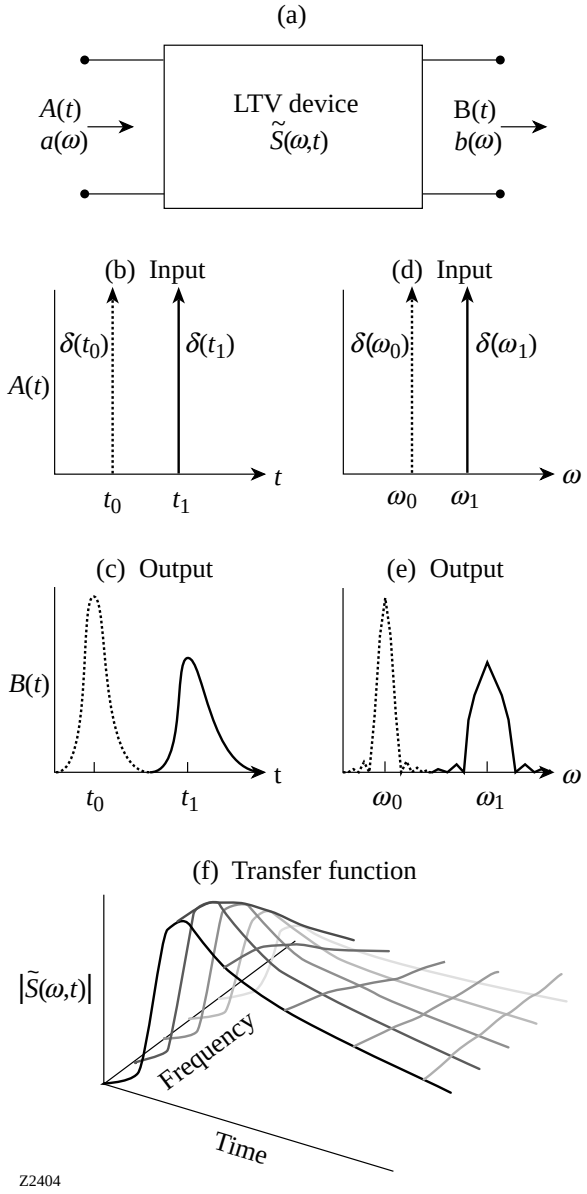

Figure 78.47
(a) Signal flow for a general linear-time- and frequency-varying device. Time variation is shown schematically by (b) identical impulses applied at different times, which result in (c) different impulse responses. Frequency variation is shown by (d) two different input sine waves and (e) differences in their modulated output spectral functions. (f) A representative sketch of the magnitude of the resulting transfer function $\tilde{S}(\omega,t)$ shows exponential time decay and low-pass filtering, such as might occur with OMEGA's photoconductive switches.

A convenient place to begin the derivation is with the time-domain differential equation describing a linear lumped-element device with time-variable coefficients:

$$\alpha_0(t)\frac{\mathrm{d}^n}{\mathrm{d}t^n}B(t)+\alpha_1(t)\frac{\mathrm{d}^{n-1}}{\mathrm{d}t^{n-1}}B(t)+\cdots+\alpha_n(t)B(t)$$

$$=\mathscr{L}(p,t)B(t)=A(t), \tag{1}$$

where the coefficients α are determined by the (time-varying) dependencies between the ports (e.g., the lumped-element models of resistance, capacitance, and inductance). The signals $A(t)$ and $B(t)$ are defined as in Table 78.VI, and we've used the operator notation

$$\mathscr{L}(p)=\alpha_0(t)p^n+\alpha_1(t)p^{n-1}+\cdots+\alpha_n(t),$$

where p is the differential operator d/dt.[7] Note that although the following derivation is for a device with a finite number of (time-varying) poles and zeros, $\tilde{S}(\omega,t)$, like $S(\omega)$, is equally applicable to distributed-element devices.

For the ideal filter model there is no time variation in the coefficients and Eq. (1) simplifies to

$$\mathscr{L}_{ij}(p)B_1(t)=A_j(t). \tag{2}$$

Assuming complex exponentials for the basis functions (so that the differential operator becomes ω) and converting to S-parameter notation $S_{ij}^{-1}(\omega)=\mathscr{L}_{ji}(p)$, we derive the frequency-domain filter transfer function of Table 78.VI, and the process is analogous for the ideal modulator model. The use of complex exponential basis functions as solutions in the transform integral leads to the formalism of Fourier transforms. Fourier transforms are useful for microwave-device characterization because they transform between a system of differential equations and a system of algebraic equations; that is to say they are *compatible* integral transform operators.[8] Non-compatible transforms do not result in simple convolution or multiplicative relationships between input and output ports.

In contrast to ideal modulators and filters, for a general device a compatible integral transform operator depends on the functional form of the variable coefficients in Eq. (1). This means that the basis functions are not, in general, $e^{\pm j\omega t}$ but rather are dependent on the particular form of modulation and frequency response. To keep the analysis independent of the details of the modulation and frequency response, we will choose a noncompatible transform such that we are able to continue to use $e^{\pm j\omega t}$ basis functions; this is the key point of this characterization technique. Some important implications of this choice will be mentioned as we derive properties of the system function resulting from this choice of integral transform.

A definition of the general linear device system function is

$$\tilde{S}_{ij}(\omega,t)=\left.\frac{B_i(t)}{A_j(t)}\right|_{A_j(t)=e^{j\omega t}}, \tag{3}$$

which differs from the traditional *S*-parameter definition in that it is now a function of time as well as frequency. In addition $\tilde{S}_{ij}^{-1}(\omega,t)=\mathcal{L}_{ji}(p,t)$, where the differential operator p transforms to ω by differentiation of $e^{j\omega t}$; therefore, $B_i(t)=\tilde{S}_{ij}(\omega,t)e^{j\omega t}$ is the output of the device for an input $A_j(t)=e^{j\omega t}$, given that the device is in a known state at every time $t \geq t_0$ (i.e., the variable coefficients evolve deterministically from time $t = t_0$). Due to the linearity of the device, by superposition the output $B_i(t)$ is defined in terms of $A_j(\tau)$ according to

$$B_i(t)=\int_0^t \tilde{h}_{ij}(\tau,t)A_j(\tau)\,d\tau. \tag{4}$$

Equation (4), where the impulse response function $\tilde{h}_{ij}(\tau,t)$ is now the more general Green's function, is a generalization of the time-invariant convolution in Table 78.VI in that the impulse response no longer depends only on the *age* from impulse time τ to observation *t*. Substituting Eq. (4) into Eq. (3) results in a transform relationship between the system function $\tilde{S}(\omega,t)$ and the new generalized impulse response $\tilde{h}_{ij}(\tau,t)$:

$$\tilde{S}_{ij}(\omega,t)=\int_{-\infty}^{\infty}\tilde{h}_{ij}(\tau,t)e^{-j\omega(t-\tau)}d\tau. \tag{5}$$

Notice that (a) $\tilde{S}(\omega,t)$ and $\tilde{h}_{ij}(\tau,t)$ are related by a Fourier transform of the first axis and (b) two other system function definitions result from transforming each of these in the second variable. We can visualize the fundamental difference between (a) these 2-D system functions that are characterizations of time- and frequency-varying devices and (b) system functions that are determined from windowed signals: the feature size of a 2-D system function (the mountains and valleys of the surface plot) along one axis is independent of the other axis, whereas (due to the uncertainty principle) the features of a system function along each axis generated by windowing are related to each other by the Fourier transform. In other words, a narrow windowing of a signal in time (necessary to prevent averaging of the system's time fluctuations) implies a widening of the spectral window (which forces averaging over spectral fluctuations), and vice versa. In the next section we show this difference in more detail by applying ambiguity functions and time-frequency distributions.[9–12]

From Eq. (4) we get a relationship between input and output by replacing $A_j(t)$ with its transform $\int a_j(\omega)e^{j\omega t}d\omega$, inverting the order of integration, and substituting from Eq. (5):

$$B_i(t)=\mathcal{F}^{-1}\left\{\tilde{S}_{ij}(\omega,t)\,a_j(\omega)\right\}, \tag{6}$$

where the differential transform operator $\mathcal{F}^{-1}\{\ \}$ is essentially the inverse Fourier transform but with the variable *t* held as a constant parameter. Equation (6) is similar to the frequency-domain filter relation in Table 78.VI in that the signal $B(t)$ is the transform of the product of the *S* (or in this case $\tilde{S}$) parameter and the input spectral function. Unlike conventional Fourier transforms, however, Eq. (4) is not a convolution, and the argument inside the brackets of Eq. (6) is not the product of two 1-D functions; therefore, it is not possible to relate the output signal algebraically to the input signal:

$$b_i(\omega)\neq\tilde{S}_{ij}(\omega,t)\,a_j(\omega). \tag{7}$$

Importantly, the complete function $\tilde{S}(\omega,t)$ cannot be found by taking a quotient $b(\omega)/a(\omega)$ as it can be when finding $S(\omega)$ for LTI devices. For network synthesis, where a model (or equivalently a differential equation) must be synthesized from a given (measured) $\tilde{S}(\omega,t)$ or $G(\tau,t)$, this consequence of noncompatible transforms has no major implications and in fact choosing the noncompatible Fourier transform allows one to use standard transform tables, making the synthesis easier. For network analysis, however, where the output $B(t)$ is found in terms of $A(\tau)$, the significance of Eq. (7) is that only simple linear time- and frequency-varying device models (having first- or second-order differential equations) can be used since

signal flow graphs and the combination of series and parallel devices are no longer algebraic or even analytic, as explained in the next paragraph.

For network analysis using $\tilde{S}(\omega,t)$ of microwave systems with time- and frequency-varying elements, the network must be broken down into block diagrams where the linear time- and frequency-varying element is isolated from the rest of the (conventionally analyzed) LFI or LTI components. The block diagram approach then requires operational methods that combine the general linear element with other components, both in cascade and parallel, to determine the overall system function. For two linear devices in parallel this is trivial; they can be combined by adding their impulse response functions, or equivalently adding their transfer functions.[13] For two devices in series, however, the combination depends on shift invariance: the overall transfer function of two LTI devices in series is accomplished by multiplying the individual transfer functions together, or equivalently convolving their impulse responses. For two LFI devices in series the transfer (modulation) functions are multiplied, while the spectral transform of the modulation is convolved.

To derive the transfer function of two general linear devices in series, we begin with the repeated operation of the transfer function (in operational form):

$$\tilde{S}(p,t)\big[a(\omega)\big] = \tilde{S}_b(p,t)\Big\{\tilde{S}_a(p,t)\big[a(\omega)\big]\Big\}, \tag{8}$$

where $\tilde{S}_a(p,t)$ and $\tilde{S}_b(p,t)$ are the transfer functions for the first and second device, respectively, and $a(\omega) = e^{j\omega t}$ is assumed. Since $\tilde{S}_b(p,t)$ will operate on both $\tilde{S}_a(p,t)$ [now $\tilde{S}_a(\omega,t)$ due to the form of its operand] and $A(t)$, we get

$$\begin{aligned}\tilde{S}e^{j\omega t} &= \tilde{S}_b\left(e^{j\omega t}\frac{\partial}{\partial t}\tilde{S}_a + \tilde{S}_a\frac{\partial}{\partial t}e^{j\omega t}\right)\\ &= \tilde{S}_b\frac{\partial}{\partial t}\tilde{S}_a e^{j\omega t} + \tilde{S}_b\omega\tilde{S}_a e^{j\omega t}\end{aligned} \tag{9}$$

and therefore

$$\tilde{S}(p,t)\,a(\omega) = \tilde{S}_b(p+\omega,t)\big[\tilde{S}_a(p,t)\,a(\omega)\big]. \tag{10}$$

Analytical Example

To demonstrate the application of $\tilde{S}$ to microwave-device characterization, a representative lumped-element device will be solved analytically. The device shown in Fig. 78.48 is a single-pole, low-pass RC filter with a sinusoidally varying capacitive element $C(t) = C_0 + C_m\sin(\omega_m t)$, where suitable values of the variables are chosen for convenience: $C_0 = 1$ pF is the steady-state capacitance, $C_m/C_0 = 0.2$ is the modulation depth, and $\omega_m = 2.3$ Grad/s is the modulation rate.

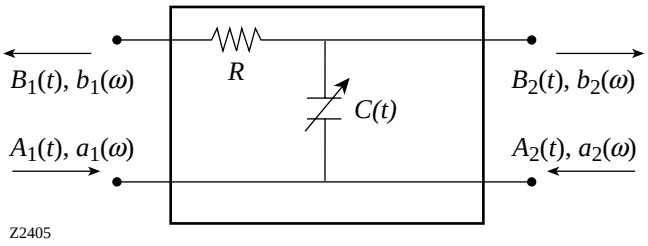

Figure 78.48
An example linear device with a time-varying capacitance and therefore time-varying pole location (bandwidth). This device is linear but cannot be modeled as only a filter or a modulator.

The differential equation for this device, written in the form of Eq. (1), is

$$\left[\frac{1}{2}C(t)\left(R+Z_0\right)\right]\frac{\mathrm{d}}{\mathrm{d}t}B(t)$$

$$+\left[1+\frac{1}{2}R\Big/Z_0+\frac{1}{2}\left(R+Z_0\right)\frac{\mathrm{d}}{\mathrm{d}t}C(t)\right]B(t) = A(t). \tag{11}$$

From *S*-parameter analysis the S_{21} for a conventional LTI filter like Fig. 78.48 is

$$S_{21}(\omega) = \frac{2\,Z_0}{2Z_0 + R + j\omega\,C\,Z_0\left(R+Z_0\right)}. \tag{12}$$

Applying Eq. (10) to the cascade elements of the resistor and shunt capacitor, we get

$$\tilde{S}_{21}(\omega,t) = \frac{2Z_0}{2Z_0 + R + (p+j\omega)CZ_0\cdot\left(R+Z_0\right)}, \tag{13}$$

which could also be found by directly solving the differential equation in Eq. (11). The $\left|S_{21}(\omega)\right|$ plot for the LTI version of this device (where the time invariant $C = C_0$) is shown in Fig. 78.49, and $\left|\tilde{S}_{21}(\omega,t)\right|$ is shown in the elevation plot of

Fig. 78.50 for one cycle of modulation. Observe in both figures the low-pass attenuation along the frequency axis and for Fig. 78.50 the sinusoidal modulation of the frequency response along the temporal axis.

To further illustrate the properties of the time-varying system function we show a surface-density plot of $|\tilde{S}(\omega,t)|$ (Fig. 78.51) over several cycles of modulation and from dc to 50 GHz. Figure 78.51 will also be used in conjunction with the windowed signal to show the limitations of windowing. An aspect of this $\tilde{S}$ shown clearly here is the skew in the peak of the temporal modulation near the 3-dB point of 6.1 GHz, due to the phase shift in the transmission function that occurs at this frequency.

Figure 78.52 is a cross section of the transfer function along the time axis, showing the modulating aspect of the device, which is seen to be frequency dependent.The cross sections of $|\tilde{S}|$ along the frequency axis (Fig. 78.53) show the low-pass filter effect of the device and indicate that the shape of the frequency response depends on time. Although stability considerations are outside the scope of this article, both Figs. 78.52 and 78.53 indicate that the instantaneous magnitude can rise momentarily above unity, resulting in a gain in the system over a short time span and finite spectral band. Modulating the capacitance causes a transfer of energy in and out of the system, and with proper terminations it is possible to create an oscillator.

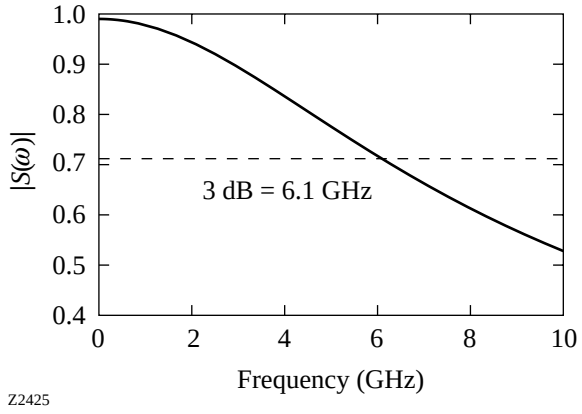

Figure 78.49
Magnitude of the transfer function $|S_{21}(\omega)|$ of a low-pass, single-pole filter that is equivalent to the circuit in Fig. 78.48 but with no time-variation in the capacitance.

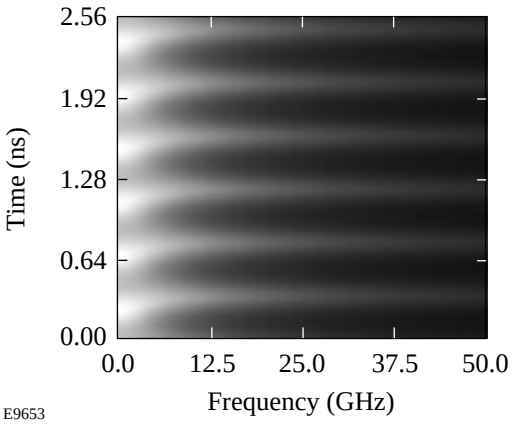

Figure 78.51
Surface-density plot of $|\tilde{S}(\omega,t)|$ for six cycles of modulation along the time axis and demonstrating low-pass filtering along the frequency axis.

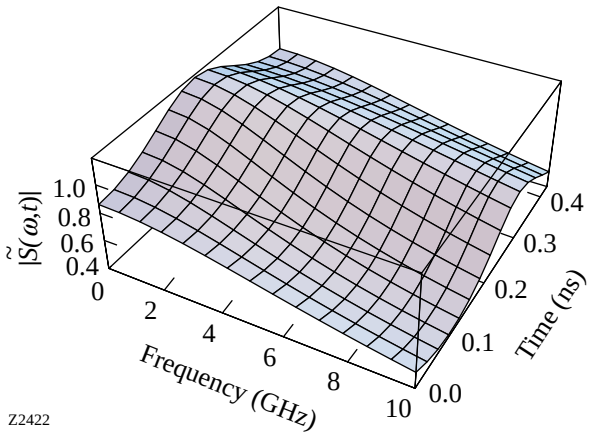

Figure 78.50
Magnitude of the transfer function $|\tilde{S}_{21}(\omega,t)|$ of a low-pass, single-pole filter with sinusoidally varying capacitance, plotted over one cycle of modulation in time and over 150% of the bandwidth in frequency.

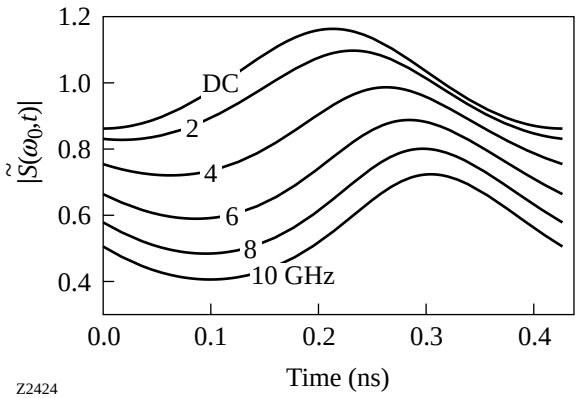

Figure 78.52
A series of cross sections through $|\tilde{S}(\omega,t)|$ along the time axis, showing the change in the magnitude and phase of the modulation for different frequencies.

Using Eqs. (6) and (13) we simulated the propagation of the sum of 5.9- and 19.5-GHz sine waves through the device. The attenuation and dispersion of each spectral component are demonstrated in Fig. 78.54, where the low-pass features are readily apparent in the output signal (solid line) as compared with the input signal (dashed line). The influence of the modulation can best be compared in Fig. 78.55, where the sinusoidal modulation puts discrete sidebands on each spectral component; however, since only magnitude is plotted, the phase shift of the modulation between different frequencies cannot be observed. Since this device not only modulates each frequency differently but also filters the signals, application of network or spectrum analysis would not adequately characterize the device.

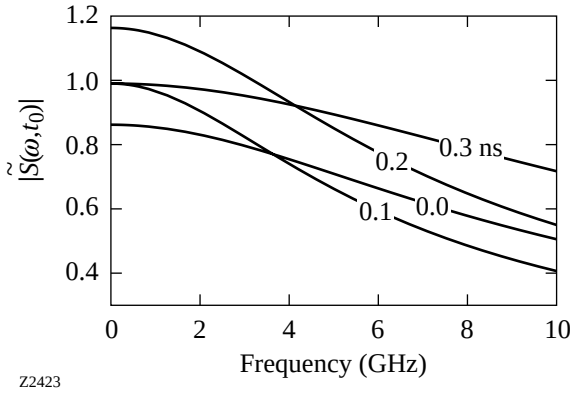

Figure 78.53
A series of cross sections through $\left|\tilde{S}(\omega,t)\right|$ along the frequency axis, showing the change in instantaneous bandwidth at different times.

In the remainder of this section we use windowed signals in an attempt to adequately characterize our time-varying filter with conventional *S*-parameter analysis, and we compare the results to our previous approach. For the windowing we use time–frequency distributions because of their appealing representation, and because they more intuitively demonstrate the fundamental constraint; due to the uncertainty principle, a narrow windowing in time necessarily leads to a broad frequency window. This is seen on a time–frequency representation by the phenomenon of *minimum area*: a surface-density plot of the time–frequency distribution of a signal consists of areas (or regions) where the signal exists at a localized time and frequency, which cannot be smaller than a constant determined by the uncertainty principle. The uncertainty is inherent to windowing in general and not time–frequency distributions in specific, so therefore the choice of specific time–frequency distributions to demonstrate the uncertainty limitations of windowing doesn't detract from the generality of the result.

To demonstrate the limitations of windowing, the particular choice of algorithm to generate a time–frequency representation is a matter of convenience: for this example we will use

$$A(\omega;t) = \int_{-\infty}^{\infty} A(t)\,\omega\, e^{-j\omega^2(t-\tau)^2}\,\mathrm{d}t, \qquad (14)$$

where $A(\omega;t)$ is the time–frequency distribution of $A(t)$ and a semicolon is used between the joint time–frequency variables to stress the dependence of the axes. This definition has the virtues of showing all the essential features of time–frequency

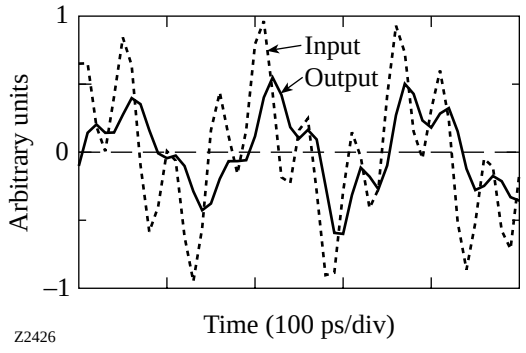

Figure 78.54
Plot of input and output signals showing the DUT's low-pass filtering effect. Dashed line is the input signal; solid line is the output signal.

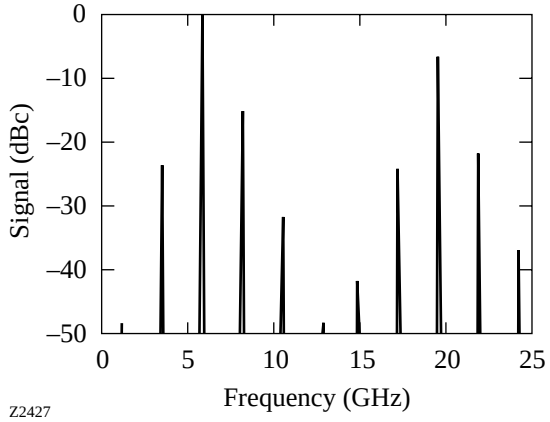

Figure 78.55
Spectral plot of output signal, showing the change in modulation characteristics for different frequencies.

distributions and (due to the use of a Gaussian window) being easily transformable back into the Fourier transform of the signal $a(\omega)$ by integration:

$$a(\omega) = \int_{-\infty}^{\infty} A(\omega; t)\,\mathrm{d}t. \tag{15}$$

Figure 78.56 shows an example windowed signal to be propagated through our system: a 2-GHz sine wave that abruptly transitions after 1.28 ns (with broadband noise) to a 20-GHz sine wave. The smearing of the signal in time (for the low-frequency signal) and frequency (for the high-frequency signals) due to windowing trade-offs (which are ultimately due to the uncertainty relationship) can be easily seen. The use of the FFT to generate the time–frequency distribution (which assumes a continuous, periodic signal) caused leakage to occur across the time boundary (top and bottom) of each spectral component of the signal; for the low-frequency signal, the leakage is significant enough to bridge the span over which it is ostensibly "off."

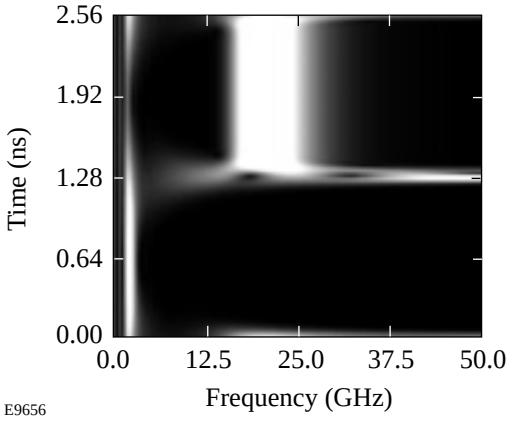

Figure 78.56
Time–frequency representation (ambiguity function) of a 2-GHz sine wave that transitions abruptly to a 20-GHz sine wave with broadband noise at the transition.

By multiplying the input signal $A_1(\omega;t)$ of Fig. 78.56 with the system function $\tilde{S}_{21}(\omega,t)$ of Fig. 78.51 we get the time–frequency distribution of the output signal $B_2(\omega;t)$ (shown in Fig. 78.57). Important features of the resulting output signal, as evidenced in the time–frequency distribution, are the significantly different modulation of each spectral component and the low-pass filtering, which attenuates the high-frequency component. Converting back to the time domain using Eq. (15) and then inverse Fourier transforming, we can compare the resulting output signal with our technique. The windowing technique gives the solid line in Fig. 78.58, while our result is the dashed line. It is evident that although windowing produced acceptable results for the second half of the signal when the modulation was much slower than the signal (i.e., the slowly varying envelope approximation), for the first half of the signal, the modulation was comparable to the signal frequency so the window effectively smeared the modulation

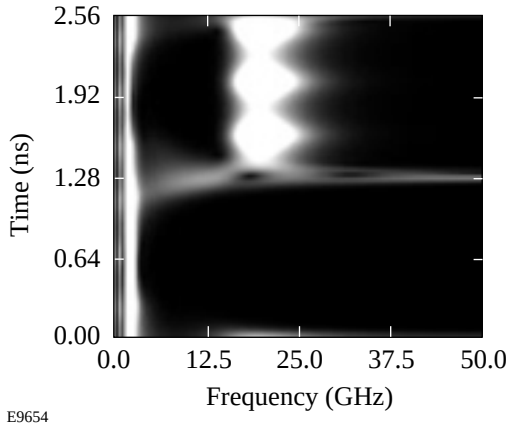

Figure 78.57
Time–frequency representation of the output signal, after multiplication of the input time–frequency distribution with the system function $\tilde{S}(\omega,t)$. The effect of the system function is shown by the attenuation of the broadband noise and the ripple in the two spectral components of the signal.

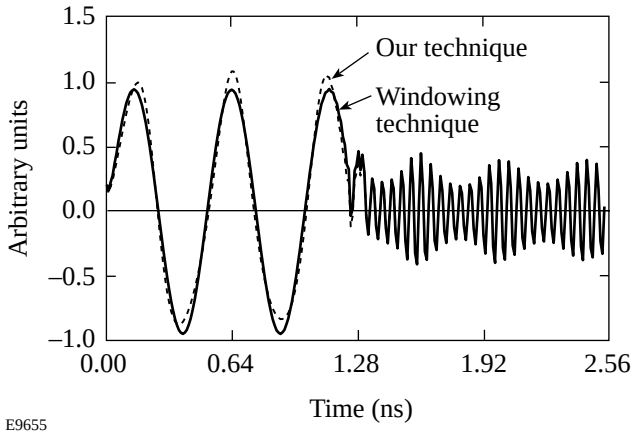

Figure 78.58
Time-domain comparison of output signals using the technique described in this article (dashed) and the windowing method (solid). The windowing appears acceptable for high-frequency signal component where the modulation is gradual, but it washes out the temporal modulation for the low-frequency component.

in time. Choosing a narrower window would not solve the fundamental problem since doing so would necessarily broaden the spectral window, causing increased smearing of the spectral response.

Conclusions

The goal of this work is to completely characterize photoconductive microwave switches regardless of the temporal and spectral variations in their frequency response (transfer function). The unique photoconductive properties of these devices that enable their use in OMEGA's pulse-shaping system also require a characterization technique that accounts for the switch's frequency and time variations simultaneously. The analysis presented in this article provides such a characterization technique and is currently being applied to the switches to optimize their pulse-shaping performance. To characterize such devices, we take advantage of the complementary aspects of LTI and LFI 1-D transfer functions and combine them into a single linear device system function $\tilde{S}(\omega, t)$. This 2-D transfer function allows us to synthesize network models based on measurements of device responses that vary rapidly in frequency as well as time. We discussed several important properties of this new $\tilde{S}$ parameter, showing similarities to conventional *S*-parameter analysis that preserve most features of the familiar Fourier transform tables. The transfer function of an analytical linear time-varying device was calculated and compared to that of an LTI filter, and the utility of the $\tilde{S}(\omega, t)$ function concept was demonstrated while also showing the limitations of windowing.

ACKNOWLEDGMENT

This work was supported by the U.S. Department of Energy Office of Inertial Confinement Fusion under Cooperative Agreement No. DE-FC03-92SF19460 and the University of Rochester. The support of DOE does not constitute an endorsement by DOE of the views expressed in this article. Kenton Green also acknowledges the support of the Frank Horton Graduate Fellowship Program.

REFERENCES

1. Laboratory for Laser Energetics LLE Review **76**, 225, NTIS document No. DOE/SF/19460-264 (1998). Copies may be obtained from the National Technical Information Service, Springfield, VA 22161.
2. G. W. Wornell, Proc. IEEE **84**, 586 (1996).
3. C. Bor-Sen, C. Yue-Chiech, and H. Der-Feng, IEEE Trans. Signal Process. **46**, 3220 (1998).
4. L. Heung-No and G. J. Pottie, IEEE Trans. Commun. **46**, 1146 (1998).
5. L. M. Silverman, IEEE Trans. Autom. Control **AC-16**, 554 (1971).
6. H. Stark, ed. *Image Recovery: Theory and Application* (Academic Press, Orlando, 1987).
7. G. H. Owyang, *Foundations for Microwave Circuits* (Springer-Verlag, New York, 1989), Chap. 10, pp. 541–606.
8. H. D'Angelo, *Linear Time-Varying Systems: Analysis and Synthesis*, The Allyn and Bacon Series in Electrical Engineering (Allyn and Bacon, Boston, 1970).
9. B. Boashash, Proc. IEEE **80**, 520 (1992).
10. H. N. Kritikos and J. G. Teti, Jr., IEEE Trans. Microw. Theory Tech. **46**, 257 (1998).
11. S. R. Kunasani and C. Nguyenj, IEEE Microw. Guid. Wave Lett. **6**, 1 (1996).
12. H. Ling *et al*., IEEE Trans. Antennas Propag. **41**, 1147 (1993).
13. W. Kaplan, Operational Methods for Linear Systems, Addison-Wesley Series in Mathematics (Addison-Wesley, Reading, MA, 1962), Chap. 2, pp. 64–103.

Damage to Fused-Silica, Spatial-Filter Lenses on the OMEGA Laser System

Vacuum surface damage to fused-silica, spatial-filter lenses is the most prevalent laser-damage problem occurring on the OMEGA laser system. Approximately one-half of the stage-C-input and output, D-input, E-input, and F-input spatial-filter lenses are currently damaged with millimeter-scale fracture sites. With the establishment of safe operational damage criteria, laser operation has not been impeded. These sol-gel-coated lenses see an average fluence of 2 to 4 J/cm^2 (peak fluence of 4 to 7 J/cm^2) at 1053 nm/1 ns. Sol-gel coatings on fused-silica glass have small-spot damage thresholds at least a factor of 2 higher than this peak operational fluence. It is now known that the vacuum surfaces of OMEGA's spatial-filter lenses are contaminated with vacuum pump oils and machine oils used in the manufacture of the spatial-filter tubes; however, development-phase damage tests were conducted on uncontaminated witness samples. Possible explanations for the damage include absorbing defects originating from ablated pinhole material, contamination nucleated at surface defects on the coating, or subsurface defects from the polishing process. The damage does not correlate with hot spots in the beam, and the possibility of damage from ghost reflections has been eliminated. Experiments have been initiated to investigate the long-term benefits of ion etching to remove subsurface damage and to replace sol-gel layers by dielectric oxide coatings, which do not degrade with oil contamination.

In this article, we discuss the implications of spatial-filter lens damage on OMEGA, damage morphologies, possible causes, and ongoing long-term experiments. The staging diagram depicted in Fig. 78.59 plots the peak design fluence (average fluence times 1.8 intensity modulation factor) at each stage of a single beamline on OMEGA; the bold lines indicate regions where spatial-filter lens damage is occurring.[1] These lenses are all fused-silica optics with a sol-gel-dipped, antireflection coating at 1053 nm. Several issues have been identified regarding these lenses. The first concern is the mechanical fracture of the lenses. As the damage continues to grow, a flaw-size criteria must be determined to prevent catastrophic lens failure (fracture into two pieces) and ensure safe laser operation. The damage morphology is important to understanding

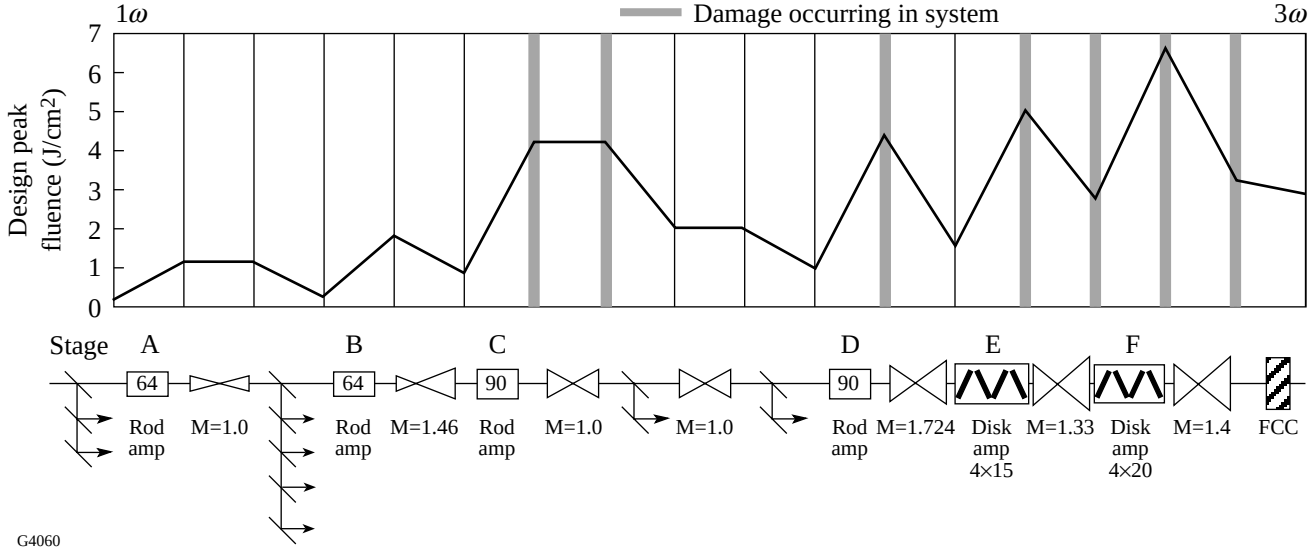

Figure 78.59
Peak design fluence plotted at each stage of the OMEGA laser. Operational laser damage is occurring at the high-fluence positions.

the initiator for large-scale fracture sites observed in Fig. 78.60 and discussed later in this article. A secondary and possibly related problem is the change in the sol-gel coating's reflectivity after exposure to the spatial-filter tube's vacuum environment. A few early experiments to investigate the damage cause are reviewed later.

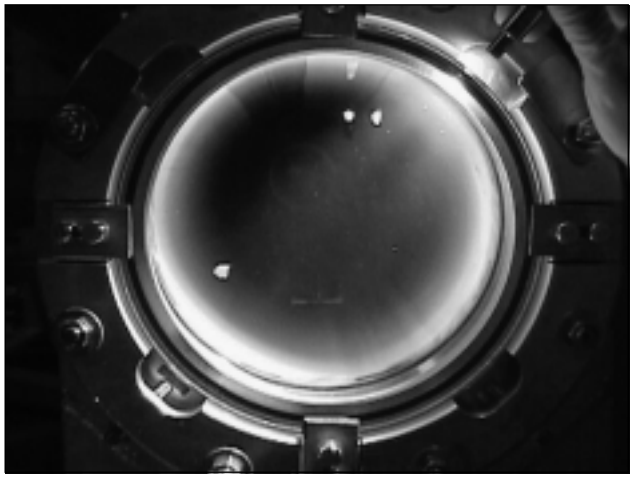

G4745

Figure 78.60
An OMEGA stage-E-input, spatial-filter lens with multiple fracture sites. The largest site is approximately 10 mm.

Mechanical Fracture

The vacuum surface of an OMEGA spatial-filter lens is under tensile stress, and any damage to this vacuum surface can lead to catastrophic crack growth if a flaw reaches a size above the critical value a_c. The critical flaw depth a_c depends on the shape of the flaw with respect to the applied stresses and can be calculated with the following equation:[2]

$$a_c = \frac{(K_c)^2}{p(Ys)^2},$$

where K_c = fracture toughness of the glass, Y = geometrical factor of the flaw, and s = bending stress induced by atmospheric pressure p.

Actual defects on OMEGA spatial-filter lenses are shallow and elliptical in cross section, and these defects can be simulated with a half-penny–shaped defect ($Y = 1$), which has a surface diameter of twice the defect depth. This model assumes the defect to be located at the vacuum-side center of the lens where the tensile stresses are greatest; therefore, the critical-flaw-size calculations are a worst-case scenario. For an OMEGA stage-F-input lens, 25 mm thick, 283 mm in diameter, and subjected to a tensile stress of 615 psi, calculation for a half-penny defect on the vacuum side of a lens yields a critical flaw depth of 10 mm. A defect of this size will be easily detected before catastrophic failure occurs.

Lens fracture on Nova and Beamlet was modeled at Lawrence Livermore National Laboratory (LLNL), arriving at a "fail-safe" lens-design criterion with two key parameters: (1) a peak tensile stress of less than 500 psi and (2) the ratio of thickness to critical flaw size of less than six.[3] The definition of a fail-safe lens requires catastrophic fracture to proceed without implosion. An implosion refers to the action of a spatial-filter lens fracturing into many pieces and then being accelerated into the evacuated volume inside the spatial-filter housing due to atmospheric pressure.[4] Given these conditions, a properly mounted window under full vacuum load will break into two pieces only, provided the air leak through the fracture is rapid enough to reduce the load on the window before secondary crack growth ensues. The list of LLE spatial-filter lens specifications in Table 78.VII indicates that all OMEGA spatial-filter lenses meet the criteria for a fail-safe optic. Data for LLNL optics are provided in Table 78.VIII. Based on radial-fracture observations in these optics, one may expect no more than a single radial fracture in an OMEGA spatial-filter lens.

If the model is correct, fully vacuum-loaded OMEGA lenses should not implode into multiple fragments when defects reach their critical flaw size but should crack into two pieces and lock together as long as the mount restrains the radial motion of the fragments. While there have been several hundred observations of damage on the vacuum side of OMEGA spatial-filter lenses, there have been no incidents of an OMEGA spatial-filter lens fracturing into two or more pieces. For safety reasons, OMEGA optics are removed when defects reach one-half their critical flaw size.

Damage Morphology

Operational damage to 1ω, fused-silica, spatial-filter lenses occurs exclusively on the vacuum side of the lens, regardless of the beam propagation direction, and is dominated by two damage morphologies originating at or near the surface. The first morphology is that of a massive fracture greater than 100 μm on the surface, while the second is a surface crack linked to a planar, clam-shell flaw in the bulk. The photograph in Fig. 78.61 shows an example of the former. After initiation of this type, fractures grow in lateral size on subsequent laser shots until the defect reaches one-half the critical flaw size. At this time, the lens is replaced. Current OMEGA lenses have

defects ranging in size from less than 0.5-mm to 10-mm diameter, and multiple damage sites on a len's vacuum surface are common. The damage depth tends to be less than one-third its surface diameter, and defects occur at apparently random radial locations. A clam-shell defect is depicted in a side view in Fig. 78.62 and in a head-on view in Fig. 78.63. The flaw's discoloration may signal that it is being filled by an absorbing material. On repeated irradiation, the clam-shell morphology is eventually obliterated and a crater develops, as in Fig. 78.61. While this clam-shell morphology is one initiator of millimeter-sized fractures, it remains inconclusive whether it is the only one. To further evaluate clam-shell damage, a sample was cleaved, as depicted in Fig. 78.64, and the exposed clam-shell cross section was analyzed by scanning electron microscopy (SEM). SEM/EDAX (energy dispersive x-ray analysis) element identification revealed the presence of carbon within the fracture while reporting its absence outside the fractured area. It is surmised that once a crack appears on the vacuum-side

Table 78.VII: Summary of peak tensile stresses and critical flaw size for OMEGA vacuum spatial-filter lenses.

Lens	Diameter (mm)	Peak stress (psi)	Peak stress (MPa)	Center thickness t (mm)	Flaw size a_c (mm)	t/a_c
C-in	149.4	656	4.52	12.5	8.8	1.4
D-in	149.4	683	4.71	12.5	8.1	1.5
E-in	213.5	538	3.71	20.0	13.0	1.5
F-in	283.4	615	4.24	25.0	10.0	2.5

Table 78.VIII: Summary of peak tensile stresses and critical flaw size for various vacuum optics in a LLNL study.[3]

Lens/Window	Peak stress (psi)	Peak stress (MPa)	Thickness t (mm)	Flaw size a_c (mm)	t/a_c	Number of radial fractures
Beamlet L3	1490	10.10	35.0	2.1	16.7	9–11
Nova SF-7	810	5.51	37.0	5.5	6.7	2–3
Nova 3ω focus	515	3.50	83.0	15.0	5.5	<1
15-cm SiO_2 plate	830	5.65	9.5	5.4	1.8	≤1

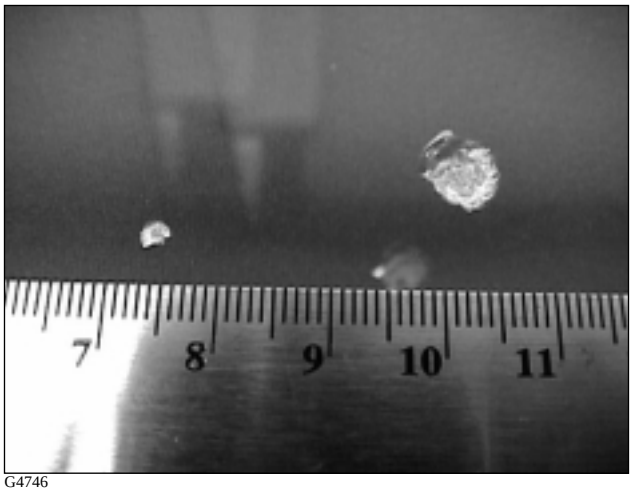

G4746

Figure 78.61
Fractures on the vacuum side of an OMEGA lens. Scale units in centimeter.


E4747

Figure 78.62
Clam-shell defect originating at the vacuum side (bulk view).

surface, oils from the machined surfaces of the spatial-filter tubes or oils from the mechanical pumping system seep into the crack over time. The combination of absorption by the trapped fluid and physical–chemical assistance in crack-front propagation during subsequent exposure is surmised to form the ring structure observed within the clam shell.

The cause of damage initiation to 1ω, fused-silica, spatial-filter lenses remains undetermined. Possible causes include (1) absorbing defects ablated from the tube wall or pinhole material, (2) oils or contamination nucleated at specific defects on the lens or coating, (3) oils absorbed into subsurface fractures expanded by tensile surface forces, and (4) isolated contamination remaining from coating application. Related work for the National Ignition Facility (NIF[5]) laser found (1) that the cause of 3ω damage was polishing-process defects within 500 μm of the surface and (2) that removal of these defects by etching improved the surface damage thresholds.[6] LLE-based ion-etching experiments to improve surface damage threshold are discussed later.

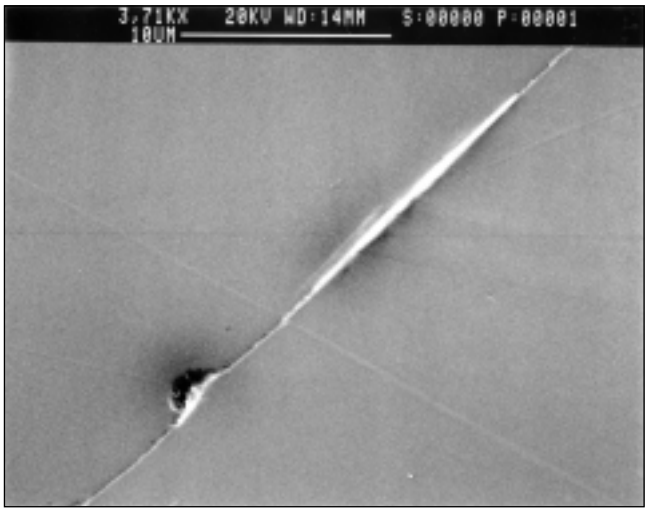

G4748

Figure 78.63
SEM vacuum surface view of a clam-shell defect on an OMEGA lens (top view).

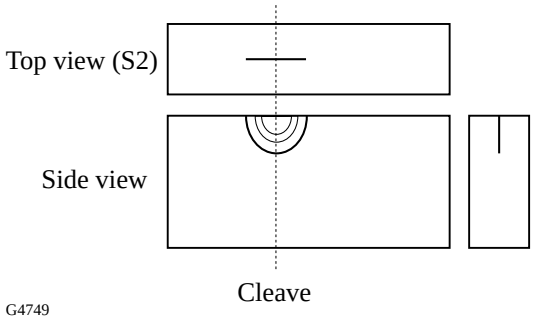

G4749

Figure 78.64
Illustration of cleave sample orientation.

Sol-Gel Coating Degradation

OMEGA sol-gel coatings show a significant change in reflectivity when exposed to a vacuum contaminated with oil from mechanical pumps. A fiber-optic spectrometer is used to measure the lens reflectivity *in situ*. While the instrument provides only relative photometric measurements, the spectral-curve shapes provide essential information on coating performance. Spectra in Fig. 78.65 show an example for how spectral response among the two sol-gel-coated surfaces of a single lens is affected by exposure to oil. While the S1, nonvacuum-side reflectivity curve is expected for a 1ω antireflection coating, the spectral characteristics of the S2, vacuum-side data show an increase in reflectivity at 1ω from 0.1% to 3.4%, owing to refractive-index changes resulting from adsorbed organic material. Evaluation of the S2 sol-gel coating by gas chromatography/mass spectrometry detected the presence of vacuum-pump oil and other organic contamination. The effect of oil contamination on the film index on a fixed-thickness sol-gel coating is modeled in Fig. 78.66. As the film index varies from 1.23 to 1.44 (film thickness is constant), reflectivity minima disappear into a flat line similar to the experimental observation in Fig. 78.65. This coating problem is seen on all OMEGA sol-gel-coated spatial-filter lenses that are collectively pumped by a single mechanically pumped vacuum system. Coatings are found to fail at different rates, however, as a result of differing cleanliness conditions or

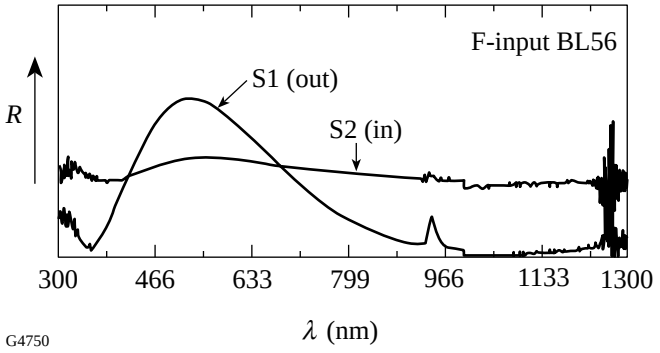

G4750

Figure 78.65
Reflectance data measured on a sol-gel-coated spatial-filter lens. The S2 (in) surface is the vacuum interface; the S1 (out) surface resides in air.

vacuum pressure levels within the spatial-filter tubes. Loss of reflectivity on a mechanically pumped tube is suffered in about six weeks or more. Hard-oxide dielectric coatings pumped under similar vacuum conditions show no change in reflectivity after exposure for similar periods.

The prototype beamline laser (PBL) assembled years earlier was disassembled about the same time as this study. The sol-gel-coated lenses in those tubes showed no coating degradation due to contamination. The tubes were first pumped mechanically and were then switched to a titanium sublimation pump, which maintained a pressure of 1×10^{-5} mbar. No record exists to indicate what method was used to clean the tubes in this PBL. To gauge the effect of different pumping methods on OMEGA, a freshly sol-gel-coated lens was placed in a spatial-filter tube that was isolated from the OMEGA mechanical pumping system. The tube was then connected to a cleaner turbo-pumping system although the tube itself could not be decontaminated *in situ*. A properly run turbo pump will exhibit very little back streaming of high-molecular-weight oils such as those used by a mechanical pump. Surprisingly, the coating was contaminated after less than four days' exposure to this environment. It was surmised that the greater mean free path in the lower pressure allowed faster transport of the oil from the contaminated walls to the sol-gel coating. This rules out the relatively simple solution of redesigning the pumping system. Improvement of the oil-contaminated system could be effected only by removing the tubes, then cleaning and baking them, possibly in a vacuum along with all the associated plumbing. This would produce an unacceptable lapse in the OMEGA firing schedule.

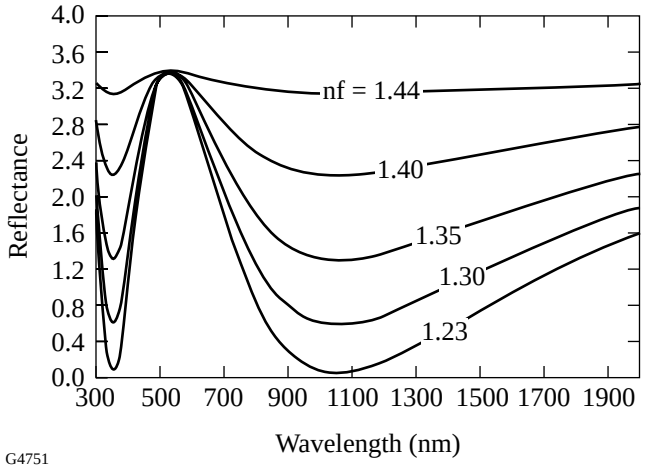

Figure 78.66
A model of reflectance change as the film index is varied for a constant film thickness. Film indices used are 1.44, 1.40, 1.35, 1.30, 1.23.

A causal link between sol-gel contamination and lens damage is suspected but has yet to be fully proven. Experiments to investigate this link and solve this damage problem are ongoing, and some results are reported in the next section. In addition, several solutions to this sol-gel-coating degradation problem are being examined to recover the light loss imposed by each "bad" surface: (1) replace sol-gel coatings with hard-oxide dielectric coatings (damage threshold is a key factor); (2) improve the spatial-filter pumping system and clean the spatial-filter tubes; and (3) add a "getter" material to adsorb the contamination before it reaches the coating.

Experiments

Several experiments were started to investigate the cause of damage to the vacuum surfaces of OMEGA spatial-filter lenses. One experiment resulted from a LLNL report that the damage threshold of fused silica at 3ω can be improved with etching. Etching appeared to remove polishing-process defects within a few hundred microns of the surface. Another experiment was proposed to examine the cleanliness conditions of the spatial-filter tubes and explore the probability that ablated pinhole debris produce damage-initiation sites.

1. Ion-Etching Tests

Since LLE developed an ion-etch capability for manufacturing distributed phase plates, it was logical to set up a process to ion etch the vacuum surface of spatial-filter lenses.[7] An experiment was designed to remove 3 μm of material from side 2 (vacuum side) of OMEGA stage-F-input, fused-silica, spatial-filter lenses, and then coat and install the optics on OMEGA to observe damage and coating failure. The following matrix was established with five lenses to be processed for each type:

(a) ion etch and sol-gel coat,
(b) ion etch and hard-oxide coat,
(c) ion etch and no coating, and
(d) no etch and no coating.

The hard-oxide coating is a hafnia/silica, e-beam-evaporated, antireflection coating.[8]

Once the optics are installed on OMEGA, observation over a long period of time (possibly one year) is required as damage onset times remain uncertain. The statistics of damage occurrence on these lenses in comparison to the damage statistics on OMEGA over the last three years will be reviewed. The experi-

ment will evaluate the effect of subsurface defects on the laser-induced damage threshold (LIDT) and also the effect of ion etching in modifying subsurface topography. These tests may also provide a correlation between damage and type of coating.

Progress on this test has been hampered by the paucity of spare optics to complete the matrix. In August 1998, type-(a) optics were installed; as of March 1999, no damage has been observed on these surfaces, and only one of the five sol-gel coatings has enhanced vacuum-side (S2) reflectivity. Transmittance loss was incurred within six weeks of installation. Three of five type-(b) optics were installed—one in October 1998 and two in November 1998; to date no damage or coating degradation has been observed. The remaining tests will be completed in June 1999 and results reported in the future.

2. Spatial-Filter Witness Tests

To investigate the cleanliness conditions of spatial-filter tubes, ten 2-in.-diam, sol-gel-coated, fused-silica samples were installed in OMEGA's stage-E spatial-filter tubes for approximately two months. All samples were damage tested at 1053 nm with a 1-ns pulse before and after exposure to the spatial-filter tube environment. Three beamlines had one sample installed at the input lens location and one sample at the output lens location, and a fourth beamline had two samples installed at each location. The sample orientation within the spatial-filter tube is illustrated in Fig. 78.67. By mounting the samples in this manner, the top surface collects pinhole condensate, while the bottom surface remains shielded.

The results revealed that the spatial-filter tube's cleanliness condition inflicts a stiff penalty, regardless of pinhole debris. As seen in Table 78.IX, all samples showed a significant drop in damage threshold after a two-months' exposure to the spatial-filter tube environment, and the top and bottom surface threshold data are virtually indistinguishable. The reported thresholds are 1-on-1 damage tests with a 1-mm^2 beam size; approximately 12 sites per sample were tested. Further SEM analysis revealed no high-Z element presence on the post-exposure surfaces, indicative of an absence of spatial-filter pinhole emanations on the top witness surface. It is difficult to predict the trajectory of ablated material, and further tests with samples located at various orientations are required to identify the path of ablated pinhole material that may contribute to lens damage. There is evidence on some pinholes that the edges are melted and craters have formed. While further experiments are needed to confirm pinhole ablation as an initiator for vacuum surface damage sites, the data confirm that oil contamination does decrease the sol-gel-coating damage threshold.

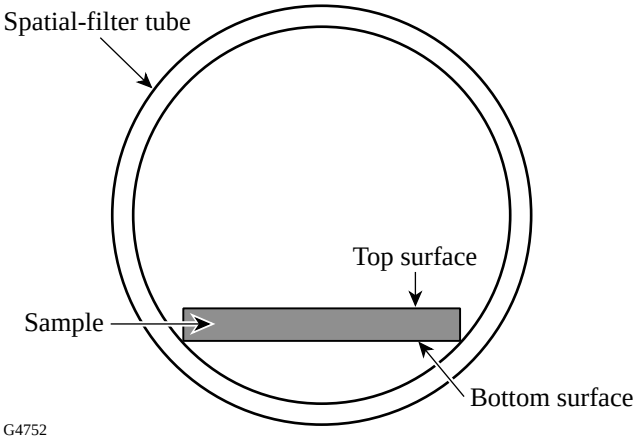

Figure 78.67
Witness sample orientation within a spatial-filter tube.

Table 78.IX: Witness sample damage threshold results before and after exposure to a spatial-filter tube environment.

Sample Orientation		Before-Exposure Damage Threshold* (J/cm^2)	After-Exposure Damage Threshold* (J/cm^2)
Top surface	average	20.7	11.9
	standard deviation	4.9	2.5
Bottom surface	average	22.1	11.3
	standard deviation	3.9	3.1

*1-on-1 damage tests at 1054 nm with a 1-ns pulse and 1-mm^2 beam size.

Conclusion

Approximately 50% of OMEGA's stage-C-input, C-output, D-input, E-input, and F-input fused-silica, spatial-filter lenses are damaged. LLE has implemented a plan to maintain the quality of OMEGA optics that includes frequent inspections and *in-situ* cleaning of optics by a skilled support group. Since damaged optics are closely monitored and the one-half critical flaw size is of the order of 10 mm in diameter, OMEGA lenses are not likely to catastrophically fail before replacement occurs. This allows for safe operation of the laser while the damage problem is being brought under control. Owing to the effectiveness of spatial filters in removing critical intensity modulations, propagating bulk or surface damage to components downstream of these damaged lenses has not been observed. Damage always occurs on the lens's vacuum surface regardless of the beam propagation direction, and an unusual clam-shell damage morphology has been observed. It is also known that the sol-gel coating on the vacuum surface fails due to organic contaminants, and this degradation is linked to a drop in the tested laser-damage threshold. A link between sol-gel contamination and lens damage is suspected but yet unproven. Experiments will continue to explore the role of subsurface fractures in the generation of the clam-shell morphology and to identify other absorbing defects on the vacuum surface, possibly originating from pinhole closures, which may be causing the damage.

ACKNOWLEDGMENT

This work was supported by the U.S. Department of Energy Office of Inertial Confinement Fusion under Cooperative Agreement No. DE-FC03-92SF19460, the University of Rochester, and the New York State Energy Research and Development Authority. The support of DOE does not constitute an endorsement by DOE of the views expressed in this article.

REFERENCES

1. *OMEGA System Operations Manual Volume I – System Description (S-AA-M-12)*, Laboratory for Laser Energetics, University of Rochester (1995), p. 43.

2. J. C. Lambropoulos, "Critical Flaw Size for Catastrophic Failure of Fused-Silica Spatial Filter Lens," 1995 (unpublished).

3. J. H. Campbell *et al*., in *Laser-Induced Damage in Optical Materials: 1996*, edited by H. E. Bennett et al. (SPIE, Bellingham, WA, 1997), Vol. 2966, pp. 106–125.

4. "Incident Analysis Report: Failure of a Spatial Filter Lens on the Beamlet Laser at Lawrence Livermore National Laboratory on April 3, 1995," Investigation Report May 11, 1995; U.S. Department of Energy, Oakland Operations Office.

5. J. Murray, *ICF Quarterly Report* **7**, 95, Lawrence Livermore National Laboratory, Livermore, CA, UCRL-LR-105821-97-3 (1997).

6. J. Yoshiyama *et al*., in *Laser-Induced Damage in Optical Materials: 1997*, edited by G. J. Exarhos et al. (SPIE, Bellingham, WA, 1998), Vol. 3244, pp. 331–340.

7. Laboratory for Laser Energetics LLE Review **74,** 71, NTIS document No. DOE/SF/19460-241 (1998). Copies may be obtained from the National Technical Information Service, Springfield, VA 22161.

8. D. J. Smith, J. F. Anzellotti, S. Papernov, and Z. R. Chrzan, in *Laser-Induced Damage in Optical Materials: 199*6, edited by H. E. Bennett *et al*. (SPIE, Bellingham, WA, 1997), Vol. 2966, p. 250.

Publications and Conference Presentations

Publications

E. L. Alfonso, F.-Y. Tsai, S.-H. Chen, R. Q. Gram, and D. R. Harding, "Fabrication of Polyimide Shells by Vapor Phase Deposition for Use as ICF Targets," Fusion Technol. **35**, 131 (1999).

T. R. Boehly, R. L. McCrory, C. P. Verdon, W. Seka, S. J. Loucks, A. Babushkin, R. E. Bahr, R. Boni, D. K. Bradley, R. S. Craxton, J. A. Delettrez, W. R. Donaldson, R. Epstein, D. Harding, P. A. Jaanimagi, S. D. Jacobs, K. Kearney, R. L. Keck, J. H. Kelly, T. J. Kessler, R. L. Kremens, J. P. Knauer, D. J. Lonobile, L. D. Lund, F. J. Marshall, P. W. McKenty, D. D. Meyerhofer, S. F. B. Morse, A. Okishev, S. Papernov, G. Pien, T. Safford, J. D. Schnittman, R. Short, M. J. Shoup III, M. Skeldon, S. Skupsky, A. W. Schmid, V. A. Smalyuk, D. J. Smith, J. M. Soures, M. D. Wittman, and B. Yaakobi, "Inertial Confinement Fusion Experiments with OMEGA—A 30-kJ, 60-Beam UV Laser," Fusion Eng. Des. **44**, 35 (1999).

S.-H. Chen, D. Katsis, A. W. Schmid, J. C. Mastrangelo, T. Tsutsui, and T. N. Blanton, "Circularly Polarized Light Generated by Photoexcitation of Luminophores in Glassy Liquid-Crystal Films," Nature **397**, 506.

T. J. B. Collins, A. Frank, J. E. Bjorkman, and M. Livio, "Supernova 1987A: Rotation and a Binary Companion," Astrophys. J. **512**, 322 (1999).

F. Dahmani, J. C. Lambropoulos, A. W. Schmid, S. J. Burns, and C. Pratt, "Nanoindentation Technique for Measuring Residual Stress Field Around a Laser-Induced Crack in Fused Silica," J. Mater. Sci. **33**, 4677 (1998).

F. Dahmani, J. C. Lambropoulos, A. W. Schmid, S. Papernov, and S. J. Burns, "Fracture of Fused Silica with 351-nm-Laser-Generated Surface Cracks," J. Mater. Res. **14**, 597 (1999).

V. N. Goncharov, "Theory of the Ablative Richtmyer–Meshkov Instability," Phys. Rev. Lett. **82**, 2091 (1999).

D. Katsis, A. W. Schmid, and S.-H. Chen, "Mechanistic Insight into Circularly Polarized Photoluminescence from a Chiral-Nematic Film," Liq. Cryst. **26**, 181 (1999).

E. M. Korenic, S. D. Jacobs, S. M. Faris, and L. Li, "Cholesteric Liquid Crystal Flakes—A New Form of Domain," Mol. Cryst. Liq. Cryst. **317**, 197 (1998).

E. M. Korenic, S. D. Jacobs, S. M. Faris, and L. Li, "Cholesteric Liquid Crystal Transmission Profile Asymmetry," Mol. Cryst. Liq. Cryst. **317**, 221 (1998).

M. Lindgren, M. Currie, C. Williams, T. Y. Hsiang, P. M. Fauchet, R. Sobolewski, S. H. Moffat, R. A. Hughes, J. S. Preston, and F. A. Hegmann, "Intrinsic Picosecond Response Times of Y-Ba-Cu-O Superconducting Photodetectors," Appl. Phys. Lett. **74**, 853 (1999).

F. J. Marshall and G. R. Bennett, "A High-Energy X-Ray Microscope for Inertial Confinement Fusion," Rev. Sci. Instrum. **70**, 617 (1999).

K. L. Marshall, J. Haddock, N. Bickel, D. Singel, and S. D. Jacobs, "Angular-Scattering Characteristics of Ferroelectric Liquid-Crystal Electro-Optical Devices Operating in the Transient-Scattering and the Extended-Scattering Modes," Appl. Opt. **38**, 1287 (1999).

C. J. McKinstrie, R. E. Giacone, and E. A. Startsev, "Accurate Formulas for the Landau Damping Rates of Electrostatic Waves," Phys. Plasmas **6**, 463 (1999).

A. V. Okishev, M. D. Skeldon, R. L. Keck, R. Roides, K. Green, and W. Seka, "A High-Bandwidth Optical-Pulse-Shaping/ Fiber-Optic Distribution System for the High-Energy OMEGA Laser-Fusion Facility," in the *Optical Fiber Communication Conference and the International Conference on Integrated Optics and Optical Fiber Communication 1999 Technical Digest* (Optical Society of America, Washington, DC, 1999), pp. 286–288.

A. V. Okishev, M. D. Skeldon, and W. Seka, "A Highly Stable, Diode-Pumped Master Oscillator for the OMEGA Laser Facility," in *Advanced Solid-State Lasers 1999 Technical Digest* (Optical Society of America, Washington, DC, 1999), pp. 124–126.

A. L. Rigatti, D. J. Smith, A. W. Schmid, S. Papernov, and J. H. Kelly, "Damage in Fused-Silica Spatial-Filter Lenses on the OMEGA Laser System," in *Laser-Induced Damage in Optical Materials: 1998*, edited by G. J. Exarhos, A. H. Guenther, M. R. Kozlowski, K. L. Lewis, and M. J. Soileau (SPIE, Bellingham, WA, 1999), Vol. 3578, pp. 472–479.

M. D. Skeldon, R. B. Saager, and W. Seka, "Quantitative Pump-Induced Wavefront Distortions in Laser-Diode- and Flashlamp-Pumped Nd:YLF Laser Rods," IEEE J. Quantum Electron. **35**, 381 (1999).

V. A. Smalyuk, T. R. Boehly, D. K. Bradley, J. P. Knauer, and D. D. Meyerhofer, "Characterization of an X-ray Radiographic System Used for Laser-Driven Planar Target Experiments," Rev. Sci. Instrum. **70**, 647 (1999).

D. J. Smith, J. A. Warner, N. E. LeBarron, and S. LaDelia, "Production of Distributed Phase Plates Using an Energetic Ion Process," in *Laser-Induced Damage in Optical Materials: 1998*, edited by G. J. Exarhos, A. H. Guenther, M. R. Kozlowski, K. L. Lewis, and M. J. Soileau (SPIE, Bellingham, WA, 1999), Vol. 3578, pp. 702–717.

B. Yaakobi and F. J. Marshall, "Imaging the Cold, Compressed Shell in Laser Implosions Using the Kα Fluorescence of a Titanium Dopant," J. Quant. Spectrosc. Radiat. Transfer **61**, 465 (1999).

Forthcoming Publications

A. Babushkin, W. A. Bittle, S. A. Letzring, M. D. Skeldon, and W. Seka, "Regenerative Amplifier for the OMEGA Laser System," to be published in SPIE's Proceedings of Solid State Lasers for Application (SSLA) to Inertial Confinement Fusion, 3rd Annual International Conference, Monterey, CA, 7–12 June 1998.

A. Babushkin, R. S. Craxton, S. Oskoui, M. J. Guardelben, R. L. Keck, and W. Seka, "Demonstration of Dual-Tripler Broadband Third-Harmonic Generation and Implications for OMEGA and the NIF," to be published in SPIE's Proceedings of Solid State Lasers for Application (SSLA) to Inertial Confinement Fusion, 3rd Annual International Conference, Monterey, CA, 7–12 June 1998.

A. Babushkin, J. H. Kelly, C. T. Cotton, M. Labuzeta, M. Miller, T. A. Safford, R. G. Roides, W. Seka, I. Will, M. D. Tracy, and D. L. Brown, "Compact Nd^{3+}-Based Laser System with Gain $G_{ss} \leq 10^{13}$ and 20-J Output Energy," to be published in SPIE's Proceedings of Solid State Lasers for Application (SSLA) to Inertial Confinement Fusion, 3rd Annual International Conference, Monterey, CA, 7–12 June 1998.

T. R. Boehly, A. Babushkin, D. K. Bradley, R. S. Craxton, J. A. Delettrez, R. Epstein, T. J. Kessler, J. P. Knauer, R. L. McCrory, P. W. McKenty, D. D. Meyerhofer, S. P. Regan, W. Seka, S. Skupsky, V. A. Smalyuk, R. P. J. Town, and B. Yaakobi, "Laser-Uniformity and Hydrodynamic-Stability Experiments at the OMEGA Laser Facility," to be published in Laser and Particle Beams.

T. R. Boehly, V. A. Smalyuk, D. D. Meyerhofer, J. P. Knauer, D. K. Bradley, R. S. Craxton, M. J. Guardalben, S. Skupsky, and T. J. Kessler, "The Reduction of Laser Imprinting Using Polarization Smoothing on a Solid-State Fusion Laser," to be published in the Journal of Applied Physics.

S.-H. Chen, J. C. Mastrangelo, B. M. Conger, and D. Katsis, "Design, Synthesis, and Potential Application of Glass-Forming Functional Organic Materials," to be published in the Proceedings of the 6th International Polymer Conference, Kusatsu, Japan, 20–24 October 1997 (invited).

T. J. B. Collins, H. L. Helfer, and H. M. Van Horn, "Oscillations of Accretion Disks and Boundary Layers in Cataclysmic

Variables: I. Unperturbed, Steady-Flow Models," to be published in Astrophysical Journal.

T. J. B. Collins, H. L. Helfer, and H. M. Van Horn, "Oscillations of Accretion Disks and Boundary Layers in Cataclysmic Variables: II. A Local, Linear Stability Analysis of Accretion Disk Boundary Layers," to be published in Astrophysical Journal.

M. Currie, C.-C. Wang, R. Sobolewski, and T. Y. Hsiang, "Picosecond Nodal Testing of Centimeter-Size Superconducting Nb Microstrip Interconnects," to be published in Applied Superconductivity.

F. Dahmani, S. Burns, and J. C. Lambropoulous, "Arresting UV-Laser Damage in Fused Silica," to be published in Optics Letters.

F. Dahmani, J. C. Lambropoulos, S. Burns, S. Papernov, and A. W. Schmid, "How Small Stresses Affect 351-nm Damage Onset in Fused Silica," to be published in SPIE's Proceedings of the XXX Annual Symposium on Optical Materials for High Power Lasers, Boulder, CO, 28 September–1 October 1998.

F. Dahmani, J. C. Lambropoulos, A. W. Schmid, S. Papernov, and S. J. Burns, "Crack Arrest and Stress Dependence of Laser-Induced Surface Damage in Fused Silica and Borosilicate Glass," to be published in the Journal of Applied Physics.

F. Dahmani, A. W. Schmid, J. C. Lambropoulos, and S. J. Burns, "Lifetime Prediction of Laser-Precracked Fused Silica Subjected to Subsequent Cyclic Laser Pulses," to be published in the Journal of Materials Science.

O. M. Efimov, L. B. Glebov, S. Papernov, A. W. Schmid, and E. Van Stryland, "Laser-Induced Damage of Photo-Thermo-Refractive Glasses for Optical Holographic Elements Writing," to be published in SPIE's Proceedings of the XXX Annual Symposium on Optical Materials for High Power Lasers, Boulder, CO, 28 September–1 October 1998.

R. E. Giacone, C. J. McKinstrie, and T. Kolber, "Angular Dependence of Stimulated Brillouin Scattering in a Homogeneous Two-Dimensional Plasma," to be published in Physics of Plasmas.

K. Green, W. Seka, M. D. Skeldon, R. L. Keck, A. V. Okishev, and R. Sobolewski, "Transient Bandwidth Analysis of Photoconductive Microwave Switches Implemented in the OMEGA Pulse-Shaping System," to be published in SPIE's Proceedings of Solid State Lasers for Application (SSLA) to Inertial Confinement Fusion, 3rd Annual International Conference, Monterey, CA, 7–12 June 1998.

J. P. Knauer, R. Betti, D. K. Bradley, T. R. Boehly, T. J. B. Collins, V. N. Goncharov, P. W. McKenty, D. D. Meyerhofer, V. A. Smalyuk, C. P. Verdon, S. G. Glendinning, D. H. Kalantar, and R. G. Watt, "Single-Mode Rayleigh–Taylor Growth-Rate Measurements with the OMEGA Laser System," to be published in Physics of Plasmas.

M. Lindgren, W.-S. Zeng, M. Currie, R. Sobolewski, S. Cherednichenko, B. Voronov, and G. N. Gol'tsman, "Picosecond Response of a Superconducting Hot-Electron NbN Photodetector," to be published in Applied Superconductivity.

J. A. Marozas, "The Cross-Phase Modulation Between Two Intense Orthogonally Polarized Laser Beams Co-Propagating Through a Kerr-like Medium," to be published in SPIE's Proceedings of Solid State Lasers for Application (SSLA) to Inertial Confinement Fusion, 3rd Annual International Conference, Monterey, CA, 7–12 June 1998.

R. L. McCrory and J. M. Soures, "Status of Direct-Drive Inertial Confinement Fusion Research at the Laboratory for Laser Energetics," to be published in the Proceedings of the 2nd Symposium on Current Trends in International Fusion Research Review and Assessment, Washington, DC, 10–14 March 1997 (invited).

P. W. McKenty, "Direct-Drive Capsule Requirements for the National Ignition Facility and OMEGA Laser Systems," to be published in Fusion Technology.

P. W. McKenty and M. D. Wittman, "Characterization of Thick Cryogenic Layers Using an Interferometric Imaging System," to be published in Fusion Technology.

A. V. Okishev, M. D. Skeldon, and W. Seka, "Multipurpose, Diode-Pumped Nd:YLF Laser for OMEGA Pulse Shaping and Diagnostics Applications," to be published in SPIE's Proceedings of Solid State Lasers for Application (SSLA) to Inertial Confinement Fusion, Monterey, CA, 7–12 June 1998.

S. P. Regan, D. K. Bradley, J. J. Carroll III, A. V. Chirokikh, R. S. Craxton, R. P. Drake, D. D. Meyerhofer, W. Seka, R. W. Short, A. Simon, R. P. J. Town, and B. Yaakobi, "Laser–Plasma

Interactions in Long-Scale-Length Plasmas Under Direct-Drive National Ignition Facility Conditions," to be published in Physics of Plasmas.

M. D. Skeldon, A. V. Okishev, R. L. Keck, W. Seka, and S. A. Letzring, "An Optical Pulse-Shaping System Based on Aperture-Coupled Stripline for OMEGA Pulse-Shaping Applications," to be published in SPIE's Proceedings of Solid State Lasers for Application (SSLA) to Inertial Confinement Fusion, 3rd Annual International Conference, Monterey, CA, 7–12 June 1998.

S. Skupsky and R. S. Craxton, "Irradiation Uniformity for High-Compression Laser Fusion Experiments," to be published in Physics of Plasmas.

V. A. Smalyuk, T. R. Boehly, D. K. Bradley, V. N. Goncharov, J. A. Delettrez, J. P. Knauer, D. D. Meyerhofer, D. Oron, D. Shvarts, and Y. Srebro, "Nonlinear Evolution of Broad-Bandwidth, Laser-Imposed Nonuniformities in Planar Targets Accelerated by 351-nm Laser Light," to be published in Physics of Plasmas.

D. J. Smith, J. A. Warner, N. E. LeBarron, T. J. Kessler, S. LaDelia, J. P. Knauer, D. D. Meyerhofer, D. Oron, and D. Shvarts, "The Development of Ion-Etched Phase Plates," to be published in Applied Optics.

R. Sobolewski, "Ultrafast Dynamics of Nonequilibrium Quasiparticles in High-Temperature Superconductors," to be published in Superconducting and Related Oxides: Physics and Nanoengineering III.

J. M. Soures, R. L. McCrory, P. B. Radha, R. Betti, W. A. Bittle, T. R. Boehly, R. Boni, D. K. Bradley, T. J. B. Collins, R. S. Craxton, J. A. Delettrez, W. R. Donaldson, R. Epstein, V. Yu. Glebov, V. N. Goncharov, D. R. Harding, P. A. Jaanimagi, R. L. Keck, J. H. Kelly, T. J. Kessler, J. P. Knauer, C. K. Li, S. J. Loucks, F. J. Marshall, P. W. McKenty, D. D. Meyerhofer, S. F. B. Morse, S. Padalino, R. D. Petrasso, S. P. Regan, W. Seka, R. W. Short, A. Simon, S. Skupsky, D. J. Smith, R. P. J. Town, B. Yaakobi, and J. D. Zuegel, "Recent Advances in Direct-Drive ICF Target Physics at the Laboratory for Laser Energetics," to be published in the Proceedings of the 1998 IAEA Conference, Yokohama, Japan, 19–24 October 1998.

M. D. Wittman and R. S. Craxton, "Self-Interference Patterns and Their Application to Inertial-Fusion Target Characterization," to be published in Applied Optics.

L. Zheng and D. D. Meyerhofer, "Self- and Cross-Plate Modulation Coefficients in a KDP Crystal Measured by a Z-Scan Technique," to be published in the Journal of the Optical Society of America B.

J. D. Zuegel and W. Seka, "Upconversion and Reduced $^4F_{3/2}$ Upper-State Lifetime in Intensely Pumped Nd:YLF," to be published in Applied Optics.

Conference Presentations

V. N. Goncharov, "Theory of the Ablative Richtmyer–Meshkov Instability," Conference on Hydrodynamic and Magnetohydrodynamic Interface Instabilities: Unsteady or Discontinuous Flows, Paris, France, 11–12 January 1999.

W. R. Donaldson, R. Boni, R. L. Keck, and P. A. Jaanimagi, "UV-Power Balance on the OMEGA Laser," LASE '99, San Jose, CA, 22–29 January 1999.

A. V. Okishev, M. D. Skeldon, and W. Seka, "A Highly Stable, Diode-Pumped Master Oscillator for the OMEGA Laser Facility," 1999 Advanced Solid-State Lasers Fourteenth Topical Meeting, Boston, MA, 31 January–3 February 1999.

The following presentations were made at the Banff Workshop on Laser Plasma Interaction Physics, Banff, Canada, 17–20 February 1999:

W. Seka, S. P. Regan, D. D. Meyerhofer, B. Yaakobi, R. S. Craxton, A. Simon, and R. W. Short, "Recent SBS and SRS Results Under Direct-Drive NIF Conditions."

R. W. Short, "Effects of SSD on Forward SBS and Filamentation."

A. V. Okishev, M. D. Skeldon, R. L. Keck, R. G. Roides, K. Green, and W. Seka, "A High-Bandwidth Optical Pulse-Shaping/Fiber-Optic Distribution System for the High-Energy OMEGA Laser Fusion Facility," OFC/IOOC '99, San Diego, CA, 21–26 February 1999.

S. Il'in, G. N. Gol'tsman, B. M. Voronov, and R. Sobolewski, "Characterization of the Electron Energy Relaxation Process in NbN Hot-Electron Devices," 10th International Symposium on Space Terahertz Technology, Charlottesville, VA, 16–18 March 1999.

J. M. Larkin, W. R. Donaldson, T. H. Foster, and R. S. Knox, "Reverse Intersystem Crossing From a Triplet State of Rose Bengal Populated by Sequential 532- and 1064-nm Laser Excitation," APS 1999 Centennial Meeting, Atlanta, GA, 20–26 March 1999.

UNIVERSITY OF
ROCHESTER